The Dissertation Committee for Yu-Heng Cheng Certifies that this is the approved version of the following Dissertation:

Membrane Fouling Study – from Fundamental Theory to Industrial Fouling Mitigation

Committee:
Benny D. Freeman, Supervisor

Donald R. Paul

Robert W. Field

Mukul M. Sharma

Nathaniel A. Lynd

Membrane Fouling Study – from Fundamental Theory to Industrial Fouling Mitigation

by

Yu-Heng Cheng

Dissertation

Presented to the Faculty of the Graduate School of

The University of Texas at Austin

in Partial Fulfillment

of the Requirements

for the Degree of

Doctor of Philosophy

The University of Texas at Austin

May 2021

Dedication

To Tiffany Wang, who always has my back on my PhD journey

To my family, who always support me from the other side of the Pacific Ocean

Acknowledgements

First of all, I want to thank Tiffany Wang, my significant one. Thank you for all your support and encouragement when I'm down. I love you, you're the best part of my Ph.D. journey and my life in the US.

Next, thanks to all my family members in Taiwan, who made my childhood full of joys and happiness. Thank you for supporting my decision to leave for graduate school, for sending me Taiwanese goods and desserts to ease my nostalgia, for cheering me up from the other side of the Earth.

I also want to thank all my great friends. My new friends in the US and the best volleyball teammates: Jonathan, Jhen, Tina, JiaLin, KueiFu, and Matt. Thank you for training me from an absolute volleyball beginner to an "OK" player, and inviting me to all the amazing parties. You make my life in the US colorful. Thank you to all my good old friends in Taiwan who are still willing to keep in touch even though I can only meet you in person once in several years. There are too many to list, but I love you all and hope to hang out with you guys more often after moving back to Taiwan.

I'm grateful to all the Freeman group members, past and present, It is my honor to work with Lisa, Peach, Mostafa, William, and all other Freeman group members. Special thanks to Alon Kirschner, who taught me all the basics of fouling theory and experiments. I would never have been able to finish this Ph.D. without you. You are the best senpai.

Thank you to my advisors, Dr. Freeman, for giving invaluable advice when I met difficulties in research. Thank you to my dissertation committee, Dr. Sharma, Dr. Field, Dr. Paul and Dr. Lynd. You always had an open door when I needed advice, I truly learned and gained valuable wisdom from each of you.

I’d like to acknowledge the U.S. Department of Energy for the different grants my work was funded through, and the University of Texas at Austin Graduate School for their supplemental fellowships. Thank you to the United States of America, and especially the great state of Texas, for the opportunity to live and learn here. God bless America.

Abstract

Membrane Fouling Study – from Fundamental Theory to Industrial Fouling Mitigation

Yu-Heng Cheng, Ph.D.

The University of Texas at Austin, 2021

Supervisors: Benny D. Freeman

Membrane filtration is widely applied to the treatment of sewage, wastewater from the biomedical industry, and flowback water from hydraulic fracturing, but fouling remains a key challenge in these applications. Membrane fouling increases mass transfer resistance and energy consumption. Severely fouled membranes require expensive cleaning or replacement, which increases operating costs and reduces filtration efficiency. Modelling membrane fouling can advance our understanding of filtration processes and improve our ability to predict the onset and severity of fouling. This study focuses on developing fouling models in constant flux crossflow operations, commonly used in industry, and on developing fouling-resistant coatings to mitigate membrane fouling in industrial filtration applications.

Two fouling mechanisms from the accepted Hermia's model, intermediate pore blocking and cake filtration, were modified and combined together to describe fouling in constant flux crossflow ultrafiltration (UF). The model gave a qualitatively good fit to experimental fouling results using rigid latex bead particles and deformable oil droplets. Observations of the model's accuracy at different fluxes shed light on the physical meaning

of the threshold flux: the flux below which cake buildup is negligible and above which cake filtration becomes the dominant fouling mechanism.

Although the model that combines intermediate pore blocking (IPB) and cake filtration can qualitatively described fouling by latex beads and emulsified oil, the IPB model fails at high foulant concentrations or high permeate flux. To resolve this issue, the IPB model has been replaced with a complete coverage model (CCM). CCM was combined with the cake filtration model, and then compared to the previous combined IPB/cake filtration model. Constant flux crossflow fouling experiments were conducted using dilute latex bead suspensions and commercial poly(ether sulfone) flat sheet ultrafiltration membranes to investigate the influence of operating conditions (foulant concentration, permeate flux, etc.) on the evolution of transmembrane pressure profile. The CCM/cake filtration combined model provides better agreement with experimental data than does the IPB/cake filtration combined model.

To mitigate fouling in oil-water separations, a new approach to preparing hydrophilic membrane coatings based on 1,4-benzoquinone and various commercially available polyetheramines was developed. These coatings, prepared specifically from 1,4-benzoquinone and Jeffamine® EDR 148, poly(benzoquinone-Jeffamine® EDR 148) (p(BQ-EDR 148)), were used to modify polysulfone (PS) ultrafiltration membranes. In fouling experiments using an oil/water emulsion, membranes exhibited comparable fouling resistance to that of a polydopamine (pDA) modified membrane, a commonly used surface-modified membrane. Based on contact angle measurements, p(BQ-EDR 148) and pDA modified membranes have similar levels of hydrophilicity, and both exhibited higher threshold flux values than did their unmodified analogs. Based on their similar threshold flux values, p(BQ-EDR 148) (76 LMH) and pDA modified membranes (74 LMH) should have similar fouling resistance. Moreover, the mean pore size of p(BQ-EDR 148) modified

membranes can be tuned, while keeping the pure water permeance constant, by changing the deposition time and molar ratio of benzoquinone to EDR 148 in the modification solution.

Table of Contents

List of Tables

List of Figures

Chapter 1: Introduction

1.1 Goals of the Dissertation

Water and energy are critical, mutually dependent resources. The production of energy requires large volumes of water, from oil and gas extraction to cooling of thermoelectric power plants. Meanwhile, energy is used to extract, treat, and deliver water. This interconnection of water and energy is known as the water-energy nexus.[1-3] A good example is shale oil production in the US. Shale gas and shale oil have recently emerged as new important sources to meet future energy demands.[4] Hydraulic fracturing, a technology used for shale hydrocarbon extraction, is associated with substantial amounts of water withdrawal and consumption.[5] This water-intensive process requires 3-5 million gallons of water to drill a single well.[6] A large amount of water is injected into a bedrock formation under high pressure, and 30% of the injected water returns to the surface as flowback water that is highly contaminated with salts, oil, heavy metal, and surfactant.[7] Deep well injection is currently the most common method for flowback water disposal,[6] but this disposal procedure causes several environmental problems. The contaminants in flowback water may pollute the surrounding areas of injection sites.[8] Also, some evidence shows that large volumes of wastewater in deep injection wells may be associated with an increase in earthquakes.[8-9] These issues lead to strict regulation on deep well injection.[10] In 2016, the Oklahoma state government ordered the shutdown of 37 of its injection wells after a record-high magnitude 5.6 earthquakes.[11] Consequently, researchers and oil companies have been working on alternative methods for flowback water treatment.

One potential substitute for deep well injection is membrane filtration, which is widely used in many fields (*e.g.*, food and beverage, petrochemical, pharmaceutical, etc.).[12-14] Membrane separation processes are environmentally friendly, cost effective, and

easy to use.[12, 15] These systems are modular and can be loaded on trailers and transported to drilling sites, making them prime candidates for flowback water treatment. However, membrane fouling remains the main challenge for water purification.[16-17] Fouling occurs when rejected solutes accumulate on the membrane surface as external fouling or clog membrane pores as internal fouling.[16] Both increase mass transfer resistance and the required energy to maintain constant throughput. Physical/chemical cleaning or even membrane replacements are required when severe fouling occurs.[18] Consequently, operating costs are high, making membrane filtration economically undesirable.

The subject of this dissertation is an investigation of fundamental fouling mechanisms and fouling mitigation in porous water treatment membranes. The goals were to:

(1) Understand the mechanisms of fouling progression in constant flux crossflow filtration, and develop models to describe and predict the rise of transmembrane pressure in porous water treatment operations.

(2) Investigate how operational conditions (foulant concentration, permeate flux, feed crossflow velocity, etc.) affect transmembrane pressure in constant flux crossflow filtration, and derive models to explain them.

(3) Improve current fouling-resistant coating technology by exploring substitutes for conventional polydopamine coatings.

1.2 FOULING MODELING

Modeling membrane fouling has played an integral part in advancing our understanding of membrane separation processes. Most early fouling studies focused on constant transmembrane pressure (ΔP, TMP) dead-end filtration (DEF). Hermia described membrane fouling under this mode as encompassing four distinct mechanisms: complete

pore blocking, intermediate pore blocking, standard pore blocking, and cake filtration.[19] Field *et al.* introduced a foulant removal term to Hermia's four mechanisms for constant ΔP, crossflow filtration.[20-22] Most industrial filtrations are based on constant flux operation, but constant ΔP DEF filtration models are not directly applicable.[23] Although there are a few models for fouling under constant flux mode—Ho and Zydney, for example, developed a constant flux DEF model for BSA protein fouling—modeling of fouling mechanisms in constant flux crossflow filtration is scarce.[24-25]

The threshold flux (TF) was defined by Field and Pearce as "useful to distinguish between regions of low fouling and high fouling both in direct-flow and crossflow systems".[21] Thus far, the TF has been useful as a qualitative tool to compare the fouling resistance performance of different membranes, but it has not been defined in terms of fouling mechanisms.[26-27]

Chapter 4 presents a redevelopment of Hermia's equations to describe fouling under constant flux crossflow filtration. Experimental results for constant flux crossflow ultrafiltration (UF) were fitted with the models, and applicability of the models is discussed. Latex bead suspensions and soybean oil-in-water emulsion were used to represent non-deformable and deformable foulants, respectively. A model combining intermediate pore blocking and cake filtration was used to model the progression of fouling in these experiments. Based on the proposed models, a physical interpretation of the TF is suggested, which clarifies the transition between different fouling mechanisms occurring at the tipping point between slow and rapid fouling.

The impacts of operational conditions, such as foulant concentration, permeate flux and crossflow velocity, are investigated in chapter 5. We found that the intermediate pore blocking model redeveloped in chapter 4 fails at high foulant concentration or permeate flux. To resolve this issue, a complete coverage model is proposed. In addition, the effects

that change the local permeate flux during fouling progression are also evaluated and incorporated into the complete coverage model, which is then combined with cake filtration from chapter 4. The new combined model better describes how operational conditions affect transmembrane pressure in constant flux crossflow filtration than does the model discussed in chapter 4.

1.3 MEMBRANE MODIFICATION

Because most polymeric membranes are made of hydrophobic material, hydrophobic solutes or suspensions attach to such membranes easily through strong hydrophobic interactions.[15] Membrane surface modification to impart hydrophilic character to the surface can lead to formation of a strongly-bound layer of water molecules that reduces hydrophobic foulant adhesion.[28] Many kinds of modification materials, such as poly(ethylene glycol) (PEG)-based coatings,[29-31] grafted polymers,[32-33] metal oxide or zwitterionic polymers have been considered as surface modification agents.[34-37] Polydopamine (pDA) has been widely studied as a membrane modification material and can be deposited onto almost any membrane by immersing it in a slightly alkaline aqueous solution of dopamine.[38-39] The influence of pDA modification on membrane properties, such as hydrophilicity, surface charge, and surface roughness, have been reported previously.[40-43] Messersmith *et al.* suggested that the catechol and amine groups of dopamine play critical roles in the oxidative polymerization and adhesion processes of pDA.[38] Therefore, materials with both amine and phenol groups may possess similar adhesion and hydrophilic properties. For example, Wang *et al.* found that polymerization between catechol and polyamine can yield a hydrophilic polymer.[44] Xu *et al.* co-deposited catechol and polyethylenimine (PEI) to modify polyacrylonitrile (PAN) nanofiltration

(NF) membranes.[45] These modified membranes showed excellent performance in separating a cationic dye and common inorganic salts from water.

Prior to the recent increase in surface modification research, Erhan *et al.* reported an anti-corrosive coating based on commercially available Jeffamine® and *p*-benzoquinone (BQ).[46-48] We found that these coatings are usually hydrophilic and could serve as substitutes for pDA coating. In chapter 6, commercially available flat-sheet polysulfone (PS) UF membranes were modified with BQ and several Jeffamines® and subjected to oily water fouling experiments. Among all tested samples, membranes modified with BQ and Jeffamines® EDR 148 (p(BQ-EDR 148) modified membrane) showed the best hydrophilicity as judged by contact angle experiments. The effect of these surface modifications on membrane pore size and distribution was investigated by molecular weight cut off (MWCO) experiments. MWCO results were used to calculate mean pore size and pore size distribution using the hindered transport model.[43] Based on these modeling results, the mean pore size can be varied without changing pure water permeance.

1.4 REFERENCES

1. Siddiqi, A.; Anadon, L. D., The Water–Energy Nexus in Middle East and North Africa. *Energy Policy* **2011,** *39* (8), 4529-4540.

2. Scott, C. A.; Pierce, S. A.; Pasqualetti, M. J.; Jones, A. L.; Montz, B. E.; Hoover, J. H., Policy and Institutional Dimensions of the Water–Energy Nexus. *Energy Policy* **2011,** *39* (10), 6622-6630.

3. Hamiche, A. M.; Stambouli, A. B.; Flazi, S., A Review of the Water-Energy Nexus. *Renewable and Sustainable Energy Reviews* **2016,** *65*, 319-331.

4. Council, W. E., World Energy Resources-Unconventional Gas, a Global Phenomenon. **2016**.

5. Nicot, J. P.; Scanlon, B. R., Water Use for Shale-Gas Production in Texas, U.S. *Environ Sci Technol* **2012,** *46* (6), 3580-6.

6. Nicot, J. P.; Scanlon, B. R.; Reedy, R. C.; Costley, R. A., Source and Fate of Hydraulic Fracturing Water in the Barnett Shale: A Historical Perspective. *Environmental Science & Technology* **2014,** *48* (4), 2464-2471.

7. Rassenfoss, S., From Flowback to Fracturing: Water Recycling Grows in the Marcellus Shale. *Journal of Petroleum Technology* **2011,** *63* (07), 48-51.

8. Bailey, R. S., Ground Water Contamination – Fracking Controversy Continues. *The Los Angles Post* 2011.

9. Hand, E., Injection Wells Blamed in Oklahoma Earthquakes. *Science* **2014,** *345* (6192), 13-14.

10. Finkel, M.; Hays, J.; Law, A., The Shale Gas Boom and the Need for Rational Policy. *Am J Public Health* **2013,** *103* (7), 1161-1163.

11. Oklahoma Orders Wastewater Disposal Wells Shut Down after Earthquake. https://www.theguardian.com/us-news/2016/sep/04/oklahoma-wastewater-wells-earthquake#:~:text=Oklahoma%20orders%20wastewater%20disposal%20wells%20shut%20down%20after%20earthquake,-This%20article%20is&text=Five%20months%20ago%2C%20US%20officials,suffer%20tremors%20as%20northern%20California.

12. Baker, R. W., *Membrane Technology and Applications. 2nd Ed.* Wiley: 2004.

13. Pearce, G. K., UF/MF Pre-Treatment to RO in Seawater and Wastewater Reuse Applications: A Comparison of Energy Costs. *Desalination* **2008,** *222* (1), 66-73.

14. Kochkodan, V.; Hilal, N., A Comprehensive Review on Surface Modified Polymer Membranes for Biofouling Mitigation. *Desalination* **2015,** *356*, 187-207.

15. Mueller, J.; Cen, Y.; Davis, R. H., Crossflow Microfiltration of Oily Water. *Journal of Membrane Science* **1997,** *129* (2), 221-235.

16. Guo, W.; Ngo, H. H.; Li, J., A Mini-Review on Membrane Fouling. *Bioresource Technology* **2012,** *122*, 27-34.

17. Miller, D. J.; Dreyer, D. R.; Bielawski, C. W.; Paul, D. R.; Freeman, B. D., Surface Modification of Water Purification Membranes. *Angewandte Chemie International Edition* **2017,** *56* (17), 4662-4711.

18. Lee, H.; Amy, G.; Cho, J.; Yoon, Y.; Moon, S.-H.; Kim, I. S., Cleaning Strategies for Flux Recovery of an Ultrafiltration Membrane Fouled by Natural Organic Matter. *Water Research* **2001,** *35* (14), 3301-3308.

19. Hermia, J., Constant Pressure Blocking Filtration Laws: Application to Power-Law Non-Newtonian Fluids. **1982**.

20. Field, R. W.; Wu, D.; Howell, J. A.; Gupta, B. B., Critical Flux Concept for Microfiltration Fouling. *Journal of Membrane Science* **1995,** *100* (3), 259-272.

21. Field, R. W.; Pearce, G. K., Critical, Sustainable and Threshold Fluxes for Membrane Filtration with Water Industry Applications. *Advances in Colloid and Interface Science* **2011,** *164* (1), 38-44.

22. Field, R. W.; Wu, J. J., Modelling of Permeability Loss in Membrane Filtration: Re-Examination of Fundamental Fouling Equations and Their Link to Critical Flux. *Desalination* **2011,** *283*, 68-74.

23. The AWWA Subcommittee On Periodical Publications Of The Membrane Process, Microfiltration and Ultrafiltration Membranes for Drinking Water. *Journal (American Water Works Association)* **2008,** *100* (12), 84-97.

24. Ho, C. C.; Zydney, A. L., A Combined Pore Blockage and Cake Filtration Model for Protein Fouling During Microfiltration. *Journal of Colloid and Interface Science* **2000,** *232* (2), 389-399.

25. Ho, C. C.; Zydney, A. L., Transmembrane Pressure Profiles During Constant Flux Microfiltration of Bovine Serum Albumin. *Journal of Membrane Science* **2002,** *209* (2), 363-377.

26. Miller, D. J.; Huang, X.; Li, H.; Kasemset, S.; Lee, A.; Agnihotri, D.; Hayes, T.; Paul, D. R.; Freeman, B. D., Fouling-Resistant Membranes for the Treatment of Flowback Water from Hydraulic Shale Fracturing: A Pilot Study. *Journal of Membrane Science* **2013,** *437* (Supplement C), 265-275.

27. Kasemset, S.; Wang, L.; He, Z.; Miller, D. J.; Kirschner, A.; Freeman, B. D.; Sharma, M. M., Influence of Polydopamine Deposition Conditions on Hydraulic Permeability, Sieving Coefficients, Pore Size and Pore Size Distribution for a Polysulfone Ultrafiltration Membrane. *Journal of Membrane Science* **2017,** *522*, 100-115.

28. Elimelech, M.; Phillip, W. A., The Future of Seawater Desalination: Energy, Technology, and the Environment. *Science* **2011,** *333* (6043), 712-717.

29. Ju, H.; McCloskey, B. D.; Sagle, A. C.; Wu, Y.-H.; Kusuma, V. A.; Freeman, B. D., Crosslinked Poly(Ethylene Oxide) Fouling Resistant Coating Materials for Oil/Water Separation. *Journal of Membrane Science* **2008,** *307* (2), 260-267.

30. Sagle, A. C.; Ju, H.; Freeman, B. D.; Sharma, M. M., PEG-Based Hydrogel Membrane Coatings. *Polymer* **2009,** *50* (3), 756-766.

31. Sagle, A. C.; Van Wagner, E. M.; Ju, H.; McCloskey, B. D.; Freeman, B. D.; Sharma, M. M., PEG-Coated Reverse Osmosis Membranes: Desalination Properties and Fouling Resistance. *Journal of Membrane Science* **2009,** *340* (1–2), 92-108.

32. Ulbricht, M.; Matuschewski, H.; Oechel, A.; Hicke, H.-G., Photo-Induced Graft Polymerization Surface Modifications for the Preparation of Hydrophilic and Low-Proten-Adsorbing Ultrafiltration Membranes. *Journal of Membrane Science* **1996,** *115* (1), 31-47.

33. Roosjen, A.; Kaper, H. J.; Van er Mei, H. C.; Norde, W.; Busscher, H. J., Inhibition of Adhesion of Yeasts and Bacteria by Poly(Ethylene Oxide)-Brushes on Glass in a Parallel Plate Flow Chamber. *Microbiology* **2003,** *149* (11), 3239-3246.

34. Yang, X.; Sun, P.; Zhang, H.; Xia, Z.; Waldman, R. Z.; Mane, A. U.; Elam, J. W.; Shao, L.; Darling, S. B., Polyphenol-Sensitized Atomic Layer Deposition for Membrane Interface Hydrophilization. *Advanced Functional Materials* **2020,** *30* (15), 1910062.

35. Jiang, S.; Cao, Z., Ultralow-Fouling, Functionalizable, and Hydrolyzable Zwitterionic Materials and Their Derivatives for Biological Applications. *Advanced Materials* **2010,** *22* (9), 920-932.

36. Zhao, Y.-H.; Wee, K.-H.; Bai, R., Highly Hydrophilic and Low-Protein-Fouling Polypropylene Membrane Prepared by Surface Modification with Sulfobetaine-Based Zwitterionic Polymer through a Combined Surface Polymerization Method. *Journal of Membrane Science* **2010,** *362* (1–2), 326-333.

37. Cai, T.; Li, X.; Wan, C.; Chung, T.-S., Zwitterionic Polymers Grafted Poly(Ether Sulfone) Hollow Fiber Membranes and Their Antifouling Nehaviors for Osmotic Power Generation. *Journal of Membrane Science* **2016,** *497*, 142-152.

38. Lee, H.; Dellatore, S. M.; Miller, W. M.; Messersmith, P. B., Mussel-Inspired Surface Chemistry for Multifunctional Coatings. *Science* **2007,** *318* (5849), 426-430.

39. Lee, H.; Lee, Y.; Statz, A. R.; Rho, J.; Park, T. G.; Messersmith, P. B., Substrate-Independent Layer-by-Layer Assembly by Using Mussel-Adhesive-Inspired Polymers. *Advanced Materials* **2008,** *20* (9), 1619-1623.

40. McCloskey, B. D.; Park, H. B.; Ju, H.; Rowe, B. W.; Miller, D. J.; Chun, B. J.; Kin, K.; Freeman, B. D., Influence of Polydopamine Deposition Conditions on Pure Water Flux and Foulant Adhesion Resistance of Reverse Osmosis, Ultrafiltration, and Microfiltration Membranes. *Polymer* **2010,** *51* (15), 3472-3485.

41. McCloskey, B. D.; Park, H. B.; Ju, H.; Rowe, B. W.; Miller, D. J.; Freeman, B. D., A Bioinspired Fouling-Resistant Surface Modification for Water Purification Membranes. *Journal of Membrane Science* **2012,** *413–414*, 82-90.

42. Kasemset, S.; Lee, A.; Miller, D. J.; Freeman, B. D.; Sharma, M. M., Effect of Polydopamine Deposition Conditions on Fouling Resistance, Physical Properties, and Permeation Properties of Reverse Osmosis Membranes in Oil/Water Separation. *Journal of Membrane Science* **2013,** *425–426*, 208-216.

43. Kasemset, S.; He, Z.; Miller, D. J.; Freeman, B. D.; Sharma, M. M., Effect of Polydopamine Deposition Conditions on Polysulfone Ultrafiltration Membrane Properties and Threshold Flux During Oil/Water Emulsion Filtration. *Polymer* **2016,** *97*, 247-257.

44. Wang, H.; Wu, J.; Cai, C.; Guo, J.; Fan, H.; Zhu, C.; Dong, H.; Zhao, N.; Xu, J., Mussel Inspired Modification of Polypropylene Separators by Catechol/Polyamine for Li-Ion Batteries. *ACS Applied Materials & Interfaces* **2014,** *6* (8), 5602-5608.

45. Xu, Y. C.; Wang, Z. X.; Cheng, X. Q.; Xiao, Y. C.; Shao, L., Positively Charged Nanofiltration Membranes via Economically Mussel-Substance-Simulated Co-Deposition for Textile Wastewater Treatment. *Chemical Engineering Journal* **2016,** *303*, 555-564.

46. Kaleem, K.; Chertok, F.; Erhan, S., A Novel Coating Based on Poly(Etheramine-Quinone) Polymers. *Progress in Organic Coatings* **1987,** *15* (1), 63-71.

47. Kaleem, K.; Chertok, F.; Erhan, S., Quinone–Amine Polymers. II. 1,3-Bis(3-Aminophenoxy) Benzene-P-Benzoquinone Oligomers. *Journal of Polymer Science Part A: Polymer Chemistry* **1989,** *27* (3), 865-872.

48. Reddy, T. A.; Macaione, D.; Erhan, S., Quinone-Amine Polymers. XV. Syntheses and Characterization of High-Temperature Resistant Poly(Arylamino-Quinone)S. *Journal of Polymer Science Part A: Polymer Chemistry* **1994,** *32* (10), 1977-1982.

Chapter 2: Background

2.1 Membrane Applications in Water Treatment

Membranes were first applied to water treatment processes in the 1960s, but over the next decades, they became increasingly used for desalination.[1] Membrane filtrations have several advantages: small, modular, easy to use, and with low chemical requirements, making them useful for a variety of processes. Membranes are used in the food and beverage industry for making beer, milk, juice, and cheese.[2] Biochemical processes, petroleum refining, paint manufacturing, and adhesive production also employ membrane filtration.[2] Even hospitals utilize membranes for sensitive procedures requiring ultrapure water.[2]

2.2 Membrane Classification

The large variety of applications described above requires different types of membranes to achieve higher efficiencies. Fig. 2.1 shows how membranes are classified based on the size of solutes they can reject.

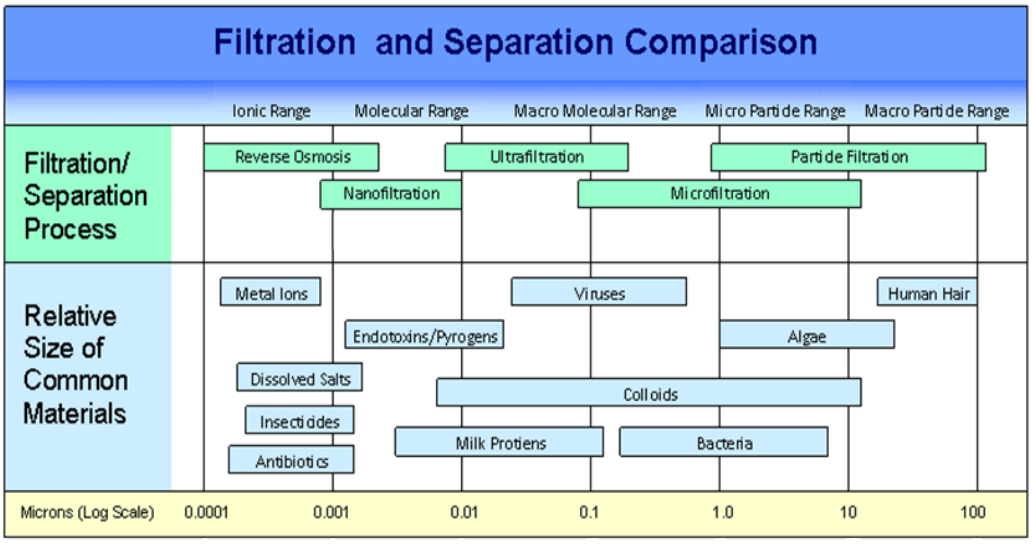

Fig. 2.1: Classification of membranes based on size of rejected materials.[3]

Generally, water treatment membranes achieve separation through pore flow or solution-diffusion mechanisms. The differences between them are shown in Fig. 2.2. Pore flow membranes have a porous substructure. The membrane rejects particles in the feed that have a larger diameter than the membrane's nominal pore diameter, while smaller particles can pass through.[4] Solution-diffusion is a process that occurs in dense, non-porous films. These membranes are capable of separating out very small solutes, including monovalent salt ions. Solute penetration is a two-step process. First, ions dissolve into the polymer matrix, and then they diffuse through polymer chains to the other side of the membrane. Separation occurs when solutes have different solution and diffusion rates.[5]

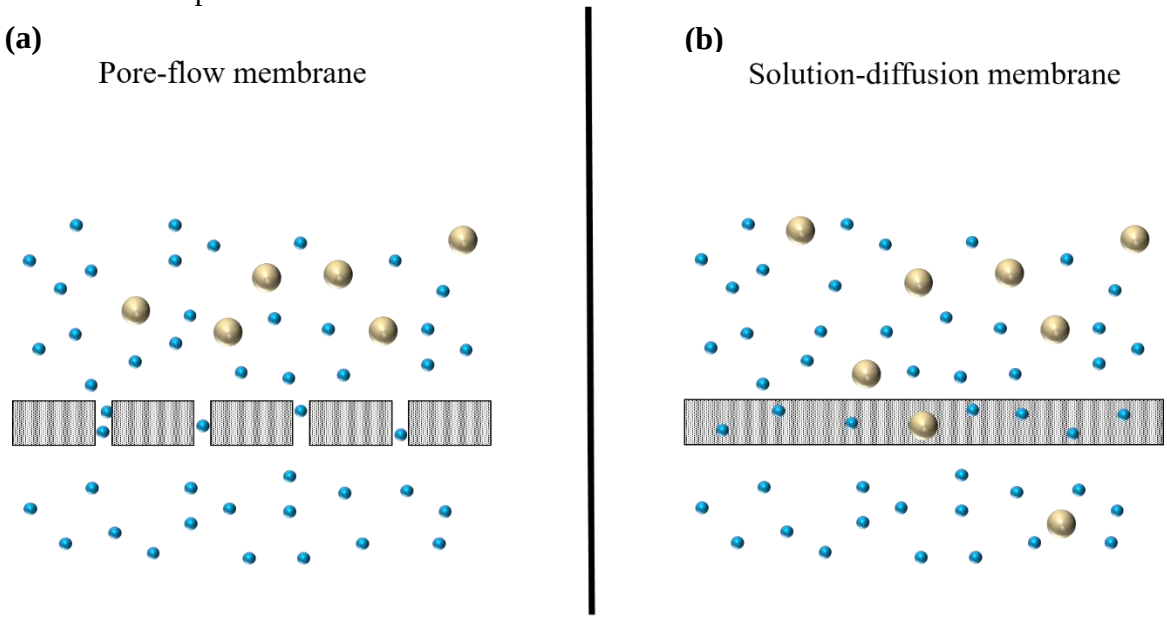

Fig. 2.2: Schematic of pore-flow vs. solution-diffusion membrane. Large (light yellow) spheres are rejected particles, small (blue) spheres represent non-rejected particles or molecules.

Typically, pore-flow membranes are used in microfiltration (MF) or ultrafiltration (UF) processes. These are low-pressure processes that effectively remove microorganisms, suspended solids, and colloids.[6] Dense (solution-diffusion) membranes are applied to the

reverse osmosis that can, for example, remove ions from water.[5] This work focuses on the fouling of porous ultrafiltration membranes.

2.3 MEMBRANE OPERATING MODES

The feed flow of ultrafiltration is usually categorized as either dead-end filtration (DEF) or crossflow.[4] A simple illustration is shown in Fig. 2.3. In DEF, the feed flows perpendicularly to the membrane surface. Rejected solutes or particles have no way to exit the system, so all of them accumulate on the membrane surface. In crossflow filtration, the feed flows tangentially to the membrane, which generates a shear force near the membrane surface. This shear force can carry a portion of the rejected solutes or particles out of the system. Besides the difference in feed flow direction, ultrafiltration can operate under constant transmembrane pressure (ΔP) or constant flux. Due to differences in feed flow and operation modes, most ultrafiltration processes fall into one of the four following categories: 1. Constant ΔP DEF, 2. Constant ΔP crossflow filtration, 3. Constant flux DEF, and 4. Constant flux crossflow filtration.[7] In this dissertation, we will focus on fouling under constant flux crossflow filtration, which is the most commonly used operation mode in industry.

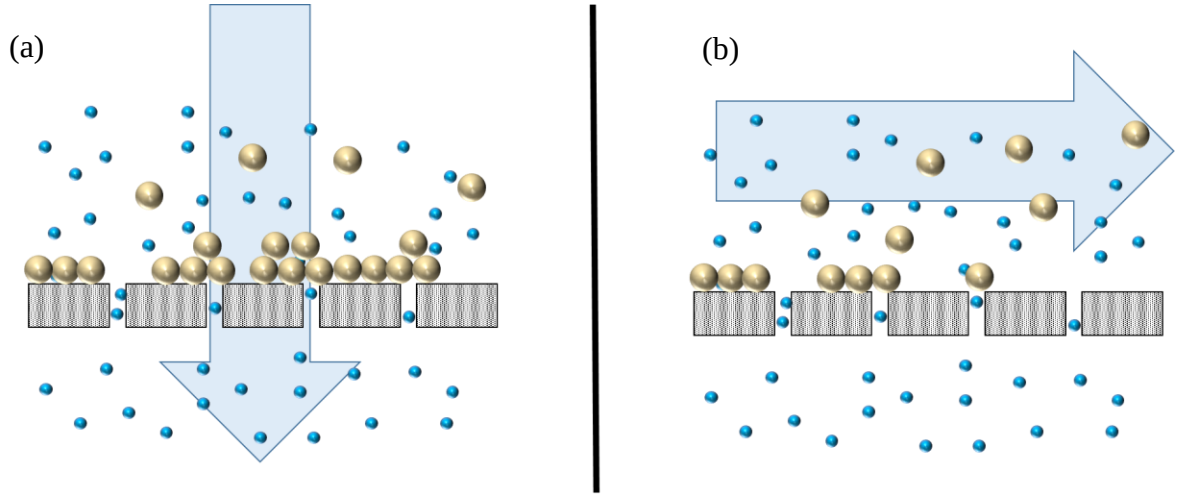

Fig. 2.3: Main flow types in membrane separations: (a) Dead-end filtration and (b) Crossflow filtration. Large (light yellow) spheres represent rejected particles, small (blue) spheres represent non-rejected particles or molecules, and the arrows indicate the feed flow direction.

2.4 MEMBRANE FOULING

As mentioned in the introduction, fouling is a major challenge for more widespread implementation of membrane systems. Fig. 2.4 shows a schematic diagram of a porous membrane in constant flux crossflow operation. The feed water flows parallel to the surface of the membrane and permeate water flows through the membrane pores. Ideally, clean water permeates through the membrane pores, while foulants are rejected due to their size, and then swept out of the system by the feed flow. Unfortunately, when the forces attracting foulants to the membrane are stronger than those rejecting them, they may accumulate on the membrane as external fouling. Some foulants may be small enough to enter and clog the pores as internal fouling.[8]

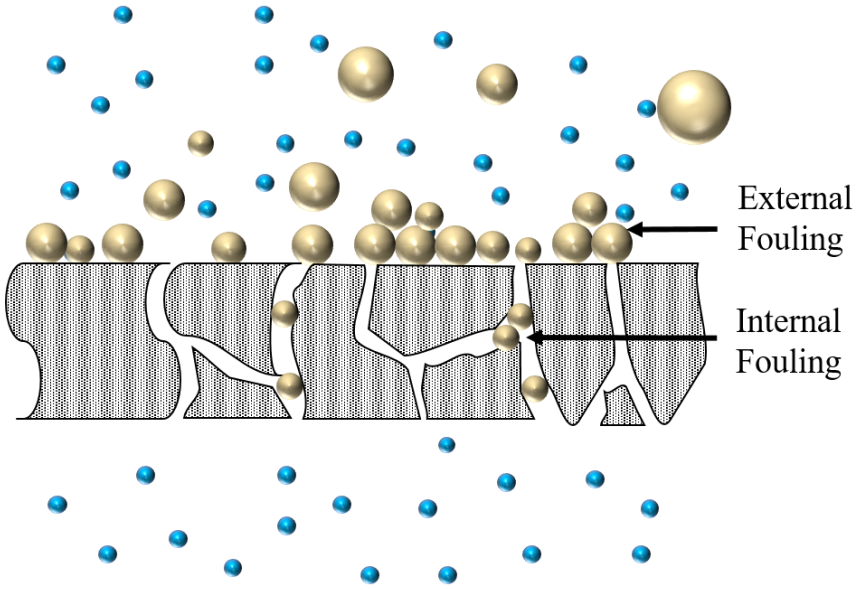

Fig. 2.4: Diagram of membrane fouling of a porous membrane in constant flux crossflow operation.

Darcy's Law can explain the effects of membrane fouling under constant flux crossflow system:[9]

$$Q = \frac{\Delta P a}{\mu R} \qquad \textbf{2.1}$$

where ΔP is the transmembrane pressure [Pa], μ is the fluid viscosity [Pa·s], R is the overall membrane mass transfer resistance [m^{-1}], Q is the volumetric flow rate [m^3/s], and a is the unobstructed (unblocked/unfouled) membrane surface area. In constant flux mode, the permeate flux, which is the volumetric flowrate normalized by the pristine membrane surface area (Q/a_0, where a_0 is the pristine membrane surface area), is constant, and ΔP is monitored. When fouling occurs, either the filtration area (a) decreases or the membrane resistance (R) increases. ΔP needs to increase during membrane fouling to maintain a constant overall flux, resulting in a higher energy requirement.

Fig. 2.5(a) and (b) show representative ΔP profiles in the low and high permeate flux regimes, respectively.[7] The ΔP in Fig. 2.5(a) increases gradually at the beginning of

the fouling experiment. After this initial rise, ΔP remains stable, indicating that the fouling rate is low. Under these conditions, filtration can continue for an extended period of time with no significant increase in transmembrane pressure. In contrast, ΔP in Fig. 2.5(b) increases sharply at the start, then rises nearly linearly over time. This ΔP rise is characterized as rapid fouling and stems from the accumulation of foulants on the membrane surface or the blockage of membrane pores. The transition flux between slow fouling (Fig. 2.5(a)) and rapid fouling (Fig. 2.5(b)) is defined as the threshold flux (TF), which was proposed by Field and Pearce.[10] TF is most commonly measured through flux stepping experiments. Detailed information on flux stepping can be found in the literature.[11-12]

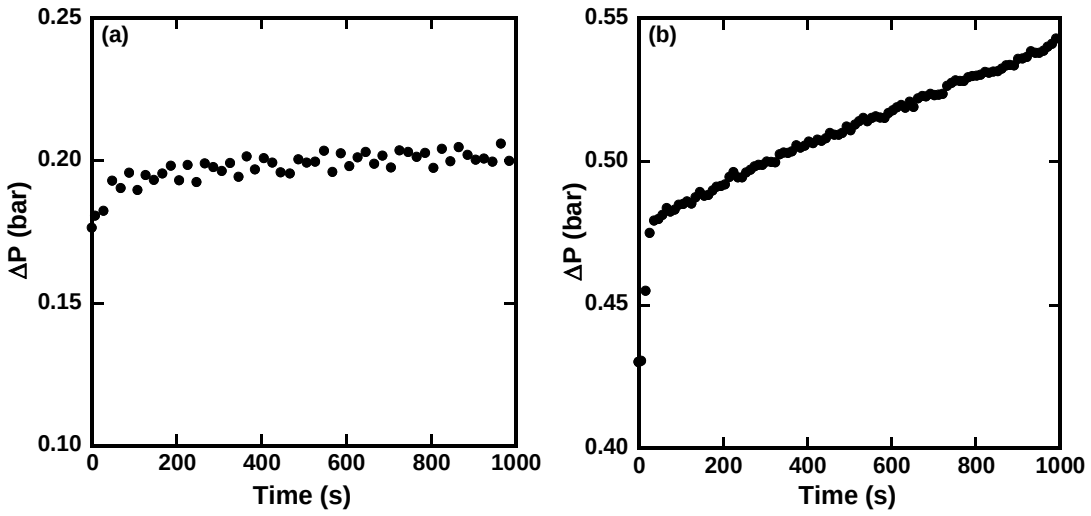

Fig. 2.5: Representative constant flux crossflow filtration ΔP profiles at (a) low permeate flux (below the TF), and (b) high permeate flux (above the TF). Operational conditions: 0.8 L/min crossflow rate, 200 ppm latex bead suspension, 40 LMH and 100 LMH permeate flux.

The balance of forces on a foulant will determine whether or not it will deposit onto the membrane under a given set of operating conditions. Two dominant forces in constant flux crossflow filtration are shown in Fig. 2.6: drag force from the permeate flow, which brings foulants towards the membrane, and shear force from the feed flow, which removes particles from the membrane. Many other forces contribute to the force balance (e.g., hydrophobic-hydrophilic interactions, electrostatic interactions, VDW forces, etc.), but the previously mentioned two forces are dominant.

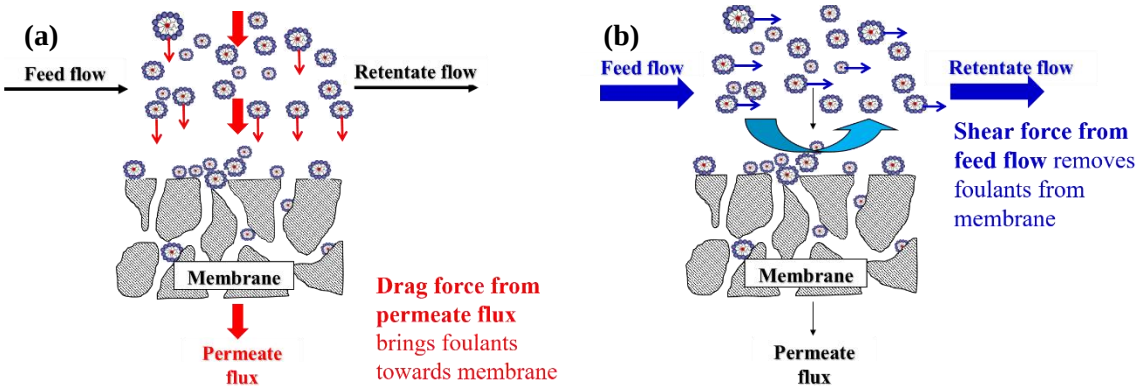

Fig. 2.6: Dominant forces in constant flux crossflow ultrafiltration: (a) Drag force caused by the permeate flow, (b) Shear force caused by the feed flow.

Because the increased energy demand caused by membrane fouling leads to increased operating costs, periodic membrane cleanings must be performed. Some membrane fouling is reversible by physical processes, such as backflow of water through the membrane, or chemical cleaning with acid or soda. However, some fouling, and especially internal fouling, cannot be removed and is deemed irreversible. When irreversible fouling becomes too severe, the entire membrane must be replaced with a new one. Therefore, understanding the mechanisms of fouling and developing solutions to mitigate fouling are important issues, and these are the main focus of this work.

2.5 REFERENCES

1. McKinnon, J. T. *Advanced Filtration of Pulp Mill Wastes*; Environmental Protection Agency: Washington, D.C., 1979.

2. AMTA. Industrial Applications for Membranes 2014.

3. Reverse Osmosis Vs. Nanofiltration and Other Filtration Technologies. https://aquaclearllc.com/technical-info/reverse-osmosis-vs-nanofiltration-and-other-filtration-technologies/.

4. Baker, R. W., *Membrane Technology and Applications. 2nd Ed.* Wiley: 2004.

5. Wijmans, J. G.; Baker, R. W., The Solution-Diffusion Model: A Review. *Journal of Membrane Science* **1995,** *107* (1), 1-21.

6. Van der Bruggen, B.; Vandecasteele, C.; Tim, V. G.; Doyen, W.; Leysen, R., A Review of Pressure-Driven Membrane Processes in Wastewater Treatment and Drinking Water Production. *Environmental Progress* **2003,** *22* (1), 46.

7. Kirschner, A. Y.; Cheng, Y. H.; Paul, D. R.; Field, R. W.; Freeman, B. D., Fouling Mechanisms in Constant Flux Crossflow Ultrafiltration. *Journal of Membrane Science* **2019,** *574*, 65-75.

8. Chang, I.-S.; Clech, P. L.; Jefferson, B.; Judd, S., Membrane Fouling in Membrane Bioreactors for Wastewater Treatment. *Journal of Environmental Engineering* **2002,** *128* (11), 1018-1029.

9. Hermia, J., Constant Pressure Blocking Filtration Laws: Application to Power-Law Non-Newtonian Fluids. **1982**.

10. Field, R. W.; Pearce, G. K., Critical, Sustainable and Threshold Fluxes for Membrane Filtration with Water Industry Applications. *Advances in Colloid and Interface Science* **2011,** *164* (1), 38-44.

11. Beier, S. P.; Jonsson, G., Critical Flux Determination by Flux-Stepping. *AIChE Journal* **2010,** *56* (7), 1739-1747.

12. Miller, D. J.; Kasemset, S.; Wang, L.; Paul, D. R.; Freeman, B. D., Constant Flux Crossflow Filtration Evaluation of Surface-Modified Fouling-Resistant Membranes. *Journal of Membrane Science* **2014,** *452*, 171-183.

Chapter 3: Materials and Methods

3.1 MATERIALS

Flat-sheet polysulfone (PS) and poly(ether sulfone) (PES) ultrafiltration membranes were purchased from Nanostone Water (Eden Prairie, MN). Dopamine hydrochloride, 4,7,10-trioxa-1,13-tridecanediamine (TTDDA), *p*-benzoquinone, Trizma hydrochloride (Tris-HCl), potassium chloride (KCl), cyclopentanone, and poly(ethylene glycol) (PEG) standards with molecular weights of 4, 8, 12, 20, 35, 100, 200 kDa were purchased from Sigma Aldrich (St. Louis, MO). Jeffamine® EDR 148, ED-600, and ED-900 were generously donated by Huntsman (The Woodlands, TX). *n*-Decane was purchased from Alfa Aesar (Ward Hill, MA). Sodium hydroxide (NaOH) and ethanol were purchased from Fisher Scientific (Pittsburgh, PA). Buffer solution with a pH of 6 was purchased from Fluka Analytical (Munich, Germany). Soybean oil (Wesson) was obtained from a local supermarket. Xiameter OFX-0193 non-ionic, silicone-based surfactant was purchased from Dow Corning (Midland, MI). A latex microsphere suspension containing 10 wt.% polystyrene particles (diameter: 0.22 μm) was purchased from Thermo Scientific, Inc. (Fremont, CA). Polysulfone (UDEL P-3500 LCD MB) was obtained from Solvay Specialty Polymers (Alpharetta, GA).

Glass plates with dimensions of 20 cm x 28 cm were used to mount membranes for modification. Acrylic plastic frames of the same dimensions with a 15 cm x 23 cm opening in the center were purchased from Interstate Plastics (Austin, TX). Rubber gaskets with the same dimensions as the acrylic plastic frames were obtained from Advanced Gasket & Supply, Inc. (Fort Worth, TX). Further details are provided elsewhere.[1-3] Silicon wafers (6" diameter) were purchased from Nova Electronic Materials, LLC (Flower Mound, TX). Ultrapure water (18.2 MΩ-cm at 25°C, <5 ppb TOC) was obtained from a Millipore Milli-

Q Advantage A10 water purification system (Billerica, MA). All chemicals were used as received.

3.2 METHODS

3.2.1 Membrane pretreatment

Membranes were pretreated using a previously developed pretreatment protocol.[1, 4-5] 20 cm × 28 cm flat membrane sheets were cut from PS or PES rolls. Membrane sheets were immersed in a dish of ethanol with the active layer facing down to wet the membrane pores. After 24 hr, the membranes were then soaked in ultrapure water for another 24 hr to replace the ethanol in the pores with water. Pretreated membranes were stored in ultrapure water until use.

3.2.2 Pure water permeance

Pure water permeance was measured using UHP43 dead-end filtration cells from Advantec MFS Inc. (Dublin, CA). The membrane sheets were cut into circular coupons (43 mm in diameter) using a steel die (4.3 cm in diameter, Tecre, Fond du Lac, WI). The cells were filled with ultrapure water, and the permeate tubes were fed into beakers, which were placed on mass balances (PR1203, Mettler Toledo) that were connected to a PC running LabVIEW® software. The measurements were started after the cells were pressurized to 30 psig (2.1 barg) and the permeate flowed steadily through the tube into the beaker. The LabVIEW® program automatically recorded the change of mass in the beakers as a function of time. The steady state flux (J) was calculated using Equation 3.1

$$J = \frac{\Delta V}{A \Delta t} \qquad \textbf{3.1}$$

where $\Delta V/\Delta t$ is the steady state volumetric flow rate [L/hr], A is the membrane surface area [m^2], and J is the steady-state flux [LMH]. The pure water permeance (Perm) was then calculated as follows:

$$Perm = \frac{J}{TMP} \quad \textbf{3.2}$$

3.2.3 Molecular weight cutoff (MWCO)

3.2.3.1 Experimental setup

MWCO tests were run according to ASTM standard E1343 – 90[6] with one modification: PEG, rather than dextran, was used as the solute. PEG solutions with different molecular weights were made by dissolving 4 g of a given molecular weight PEG standard into 4 L of ultrapure water. The PEG standards used in this experiment had molecular weights of 4, 8, 12, 20, 35, 100, and 200 kDa and low polydispersity values. Each solution was then filtered through the membrane separately, in order of increasing molecular weight. Amicon® 8200 (Millipore Corp.) dead-end filtration stirred cells were used for the filtration. To mitigate concentration polarization, the stirring speed was set to 250 rpm. The permeate flow rate was kept low (*i.e.*, 0.17 mL/min), which corresponds to a permeate flux of 0.0001 cm/s or 3.6 LMH.[6]

The PEG solution was circulated through the cells for 30 minutes to let the system reach steady state. The organic content of the feed and permeate solutions was analyzed using the Total Organic Carbon Analyzer (TOC-VCSH, Shimadzu Corp., Japan). The rejection and observed sieving coefficient (S_0) were calculated according to Equations 3.3 and 3.4, respectively. The observed sieving coefficient is defined as follows

$$R = \left(1 - \frac{C_p}{C_b}\right) \quad \textbf{3.3}$$

$$S_0 = 1 - R = \left(\frac{C_p}{C_b}\right) \quad \textbf{3.4}$$

where R is the percent rejection, and C_p/C_b is the ratio of permeate to feed organic carbon concentrations. All membranes and cells were washed with ultrapure water between runs.

Organic rejection curves were plotted as a function of PEG molecular weight. The MWCO of a specific membrane is the PEG molecular weight at which the organic rejection is 90%.[6] The nominal pore size was estimated by using Equation 3.5 to calculate the Stokes radius of PEG at this molecular weight:[7]

$$a = 16.73 \cdot 10^{-3} M_w^{0.557} \quad \textbf{3.5}$$

where a is the Stokes radius of PEG [nm], and M_w is the PEG molecular weight [g/mol].

3.2.3.2 MWCO concentration polarization correction

The organic content ratio of permeate to feed is defined as the observed sieving coefficient (S_0), as shown in Equation 3.4. However, S_0 may deviate from the actual sieving coefficient (S_a) defined in Equation 3.6.[8] S_a is the ratio between C_p and the concentration at the membrane surface, which cannot typically be measured directly.

$$S_a = \frac{C_p}{C_f} = 1 - R_a \quad \textbf{3.6}$$

where S_a is the actual sieving coefficient, C_f is the concentration at the membrane surface, and R_a is the actual rejection.

The stagnant film model can be used to calculate the actual sieving coefficient from the observed sieving coefficient, as shown in Equation 3.7.[9-10]

$$S_a = \frac{S_0}{(1 - S_0)\exp\left(\frac{J_v}{k}\right) + S_0} \quad \textbf{3.7}$$

where J_v is the measured average permeate flux [m/s] and k is the average mass transfer coefficient in the concentration boundary layer.

In this study, C_p and C_b were measured by TOC. These values were used to calculate the observed sieving coefficient S_o for each sample. J_v and k were calculated as described by Kasemset *et al.*[8] The actual sieving coefficient values were then calculated using Equation 3.6. The actual rejection was also calculated according to Equation 3.6.

3.2.3.3 Mean pore size and pore size distribution modeling

The Model proposed by Kasemset *et al.* was used to calculate the mean pore size and pore size distribution of membrane samples from MWCO data.[8] Briefly, the membranes are assumed to have a log-normal pore size distribution:[11-12]

$$n(r) = \frac{n_o}{r} \times \frac{1}{\sqrt{2\pi\, ln(1+(\sigma/\bar{r})^2)}} \times exp\left\{ -\left[ln(r/\bar{r}) \right]^2 \times \left[\frac{1+(\sigma/\bar{r})^2}{2ln[1+(\sigma/\bar{r})^2]} \right] \right\} \qquad \textbf{3.8}$$

where n(r) is the number of pores of radius r per unit area, n_o is the total number of pores per unit area, $\bar{r}$ is the mean pore size, and σ is the standard deviation of the log-normal distribution. By choosing $\bar{r}$ and σ as fitting parameters, the actual sieving coefficient (S_a) was simulated using hindered solute transport and concentration polarization models.[8] More details of the Kasemset model can be found in a previous publication. [8]

3.2.4 Contact angle (CA)

Contact angle (CA) was measured by a goniometer (ramé-hart, model 200-F1) using the captive bubble method.[13] A 3 mm strip of membrane was clamped tightly in a sample holder with the active layer facing down. The assembly was submerged into a box of ultrapure water. A droplet of *n*-decane was attached to the active layer of the strip using a syringe (Cole-Parmer, Vernon Hills, Illinois) equipped with a J-shaped needle. The

contact angle between the membrane and the tangent line of the *n*-decane droplet was calculated by DROPimage Standard software. An illustration of a contact angle measurement is shown in Fig. 3.1 and 3.2.

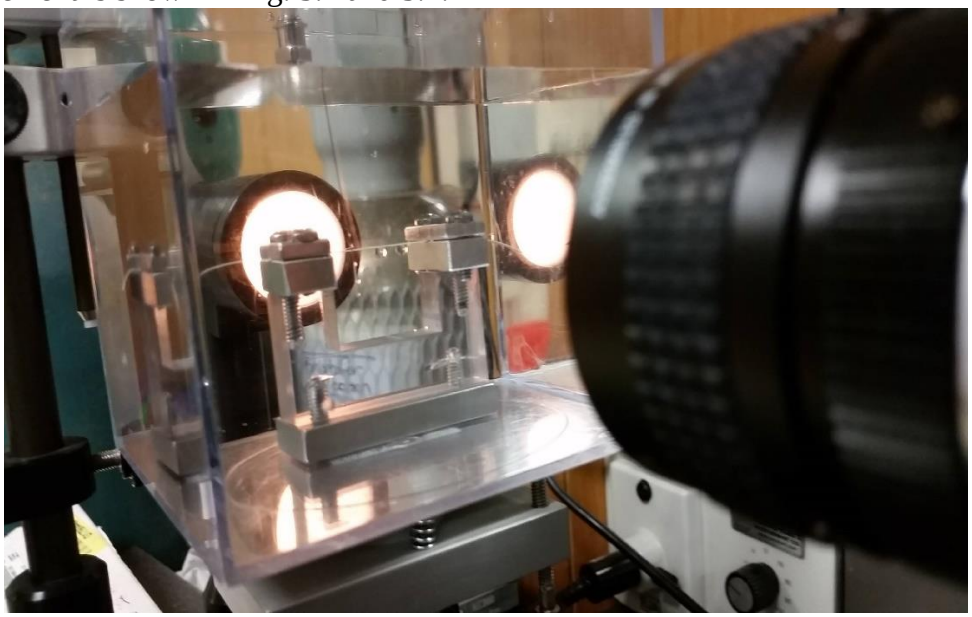

Fig. 3.1: Experimental setup for contact angle measurements

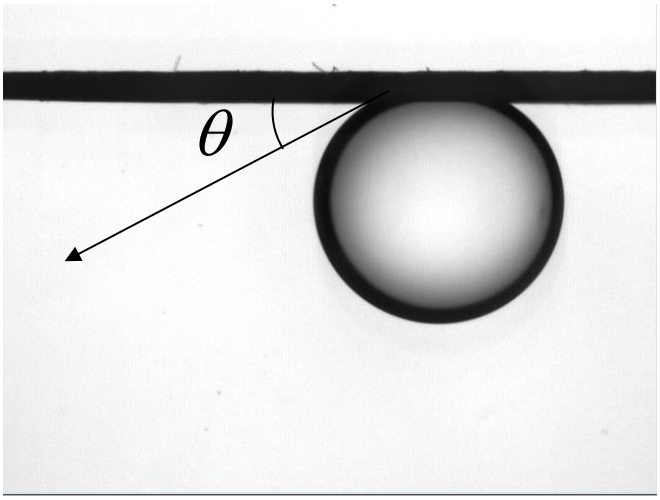

Fig. 3.2: Illustration of contact angle measurement, where θ is the contact angle measured by DROPimage.

3.2.5 Scanning electron microscope (SEM) image

SEM images of membranes were taken using an FEI Quanta 650 scanning electron microscope (Hillsboro, OR). The membrane samples were first fouled in the crossflow filtration system at desired conditions, and then gently rinsed with DI water to remove residual foulant solution. Membranes were air dried for 24 hours after the fouling procedure. Prior to imaging, the dried samples are sputtered with platinum for 60 seconds to minimize surface charging effects.

3.2.6 Zeta potential

Membrane zeta potential was measured with an AntonPaar (Ashland,VA) SurPASS electrokinetic analyzer. Two membrane coupons (25 mm x 55 mm) were separated by two polypropylene spacers to form a flow channel where the electrolyte solution could flow tangentially across the membrane surface. One sample was punched with two holes to allow flow into and out of the clamping cell. A 10^{-3} M KCl solution was used as the background electrolyte. Initially the pH was raised above 10 with a 0.1M NaOH solution. The instrument measured the membrane zeta potential at pH values ranging from 10 to 3, automatically adjusting the pH by auto-titrating with a 0.1M HCl solution. The applied pressure was 300 mBar.

3.2.7 Membrane fouling

3.2.7.1 Model foulant preparation

Fouling tests were conducted with either a model oil/water emulsion or a latex bead suspension.[2, 5, 14] Latex bead suspensions were made by first carefully rolling the latex bead container on a flat surface, followed by sonication in a bath for 30 s to uniformly disperse the latex beads. 10 wt.% latex bead suspension (0.22 μm) were diluted with 8 L of ultrapure

water to make the desired concentration of suspension. The ionic strength was adjusted to 10^{-5} M using 80 µL of 1 M KCl solution. The pH of the suspension was adjusted to 6 using 8 mL of pH 6 buffer.[14]

Soybean oil emulsions had a soybean oil-to-surfactant (OFX-0193) ratio of 9:1 (10.8 g soybean oil : 1.2 g OFX-0193 surfactant for a 1500 ppm emulsion, 1.44 g soybean oil : 0.16 g OFX-0193 surfactant for a 200 ppm emulsion) in 8L of emulsion. Oil and surfactant were added to 1 L of ultrapure water in a commercial heavy duty blender (Waring Laboratory, Stamford, CT). After mixing at 20,000 rpm for 3 minutes, the emulsion was diluted with 7 L of DI water (making sure to wash all residue from the blender). Oil droplets had an average diameter of ~3.4 ± 1.3 µm.[14]

3.2.7.2 Fouling system

Fouling experiments were conducted in a constant flux crossflow setup (*cf.* Fig. 3.5). [15] Crossflow cells had a rectangular flow path (31.75 mm wide x 82.55 mm long x 2.565 mm deep).[15] Three membrane samples (filtration area of 19.4 cm^2) were tested simultaneously during each run. The feed flow rate is controlled by a gear pump (Cat. No. Drive: 75211-30 Head: 07003-04 Cole-Parmer, Vernon Hills, IL). Most experiments have a feed flow rate of 0.8 L/min, except for the crossflow study in Chapter 4. This feed flow rate corresponds to a crossflow velocity of 0.164 m/s and a Reynolds number of ~1000. Feed pressure was set to 30 psig (~2.1 barg) and maintained at 30 psig (2.1 bar) using a back pressure regulator (Cat. No. EB1HF1, Equilibar, Fletcher, NC). The permeate flux of each cell was controlled by a peristaltic pump (Cat. No. Drive: 7523-80, Head: 7519-20, Cartridge: 7519-75, Cole-Parmer, Vernon Hills, IL). The permeate flow rates were measured by Coriolis-type flow meters (Cat. No. M13-ABD-11-0-S, Bronkhorst, Bethlehem, PA) downstream from the peristaltic pumps. Flow meters and pumps were

connected to a PC running LabVIEW®. Permeate and feed streams were continuously recycled to the feed tank to maintain constant foulant concentration.

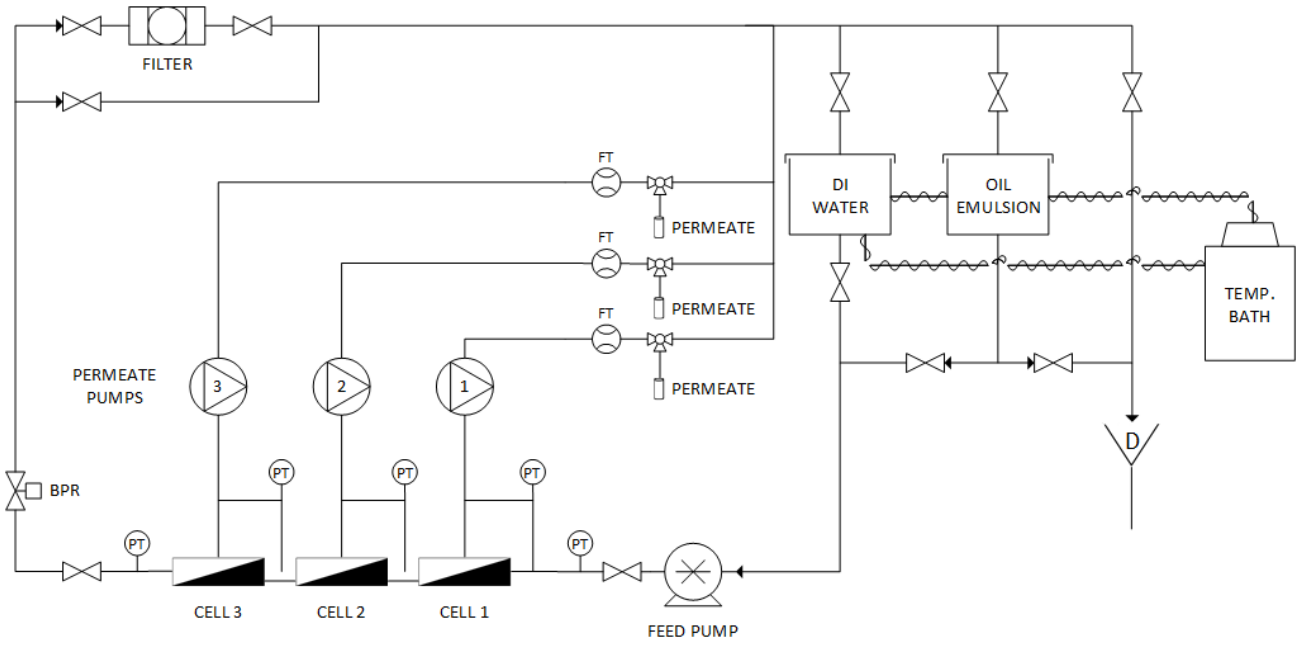

Fig. 3.3: Schematic of the crossflow fouling system employed in this work. (PT- pressure transducer, FT- flow transducer, BPR- back pressure regulator, D- drain)

3.2.7.3 Constant flux crossflow fouling

In constant flux crossflow fouling experiments, the operating parameters (*i.e.*, feed flow, feed pressure, and permeate flux) were initially adjusted to their desired values with DI water flowing through the system. While circulating DI water through the system, the flow was passed through a cartridge filter (Cat. No. Housing: 29820-11, Filter 01508-93, Cole-Parmer, Vernon Hills, IL). To ensure stable control of the permeate flux, air bubbles were removed from the permeate lines by flowing ultrapure water at the desired permeate flux for 20 minutes prior to initiating fouling. Fouling was initiated by switching the feed

inlet from the DI water tank to the foulant tank. Once the foulant emulsion was introduced as the feed solution, the cartridge filter was bypassed. To avoid dilution of the foulant with DI water present in the system, the solution was directed to the drain until it visibly looked like the fresh fouling solution, at which point both permeate and effluent streams were recycled back to the foulant feed tank to keep the feed concentration constant.

As the membranes fouled, the ΔP required to maintain the desired constant flux increased due to increasing mass transfer resistance or decrease in clean membrane surface area. Differential pressure transducers monitored the ΔP in each cell over time. A PID controller in the LabVIEW® program adjusted the voltage to the permeate pumps to maintain the permeate flux set point. For soybean oil emulsion, the organic content of both feed and permeate solutions was analyzed using a TOC analyzer, and rejection values were calculated using Equation 3.3, without applying a concentration polarization correction. Latex bead suspension rejection was based on turbidity using a Hach2100AN turbidity meter (Loveland, CO). Feed and permeate turbidities were measured, and the rejection was calculated using Equation 3.3, substituting turbidity for organic carbon concentration.

3.2.7.4 Flux stepping

The threshold flux (TF) was measured by flux stepping, a commonly used technique.[1-2, 16] Flux stepping experiments were run similarly to the constant flux crossflow fouling experiments described above, except the permeate flux was not kept constant throughout the experiment. Membranes were first challenged with foulant at a low constant flux (*i.e.*, 20 LMH) for 20 minutes, and then the permeate flux set point was increased by 10 LMH every 20 minutes. The experiment was terminated when ΔP reached 30 psig (*i.e.*, equal to the feed pressure), because ΔP larger than the feed pressure may lead to formation of air bubbles in the permeate line, disrupting the control loop. From the experiments, a

numerical value for the TF of each foulant-membrane pair was determined. Several methods of analysis, discussed in further detail in Chapters 4 and 6, can be used to determine the value of the threshold flux from such experiments.[1]

3.2.8 Membrane modification

A PS membrane sheet was placed on a glass plate (active side up) and held in place by a rubber gasket and plastic frame sealed with large metal binder clips (1" capacity) (*cf.* Fig. 3.1). The glass plate was placed on a rocking platform shaker (Cat. No. 12620-906, VWR International LLC, Randnor, PA). Membrane coating was performed at ambient temperature. Tris buffer (15 mM) was prepared by dissolving 2.364 g of Tris-HCl in ultrapure water (1L) and adjusting pH to 8.8 by adding sodium hydroxide. BQ and Jeffamine®, or dopamine hydrochloride, was dissolved in Tris buffer and poured onto the membrane surface. The rocking platform shaker is set to a rocking speed of 30 tilts/min and a tilt level of 4 to ensure thorough mixing. After the desired deposition time was reached, the membrane sheet was removed from the assembly and rinsed with ultrapure water. Before further use, these modified membrane sheets were soaked in water overnight to remove any weakly-bound coating materials.

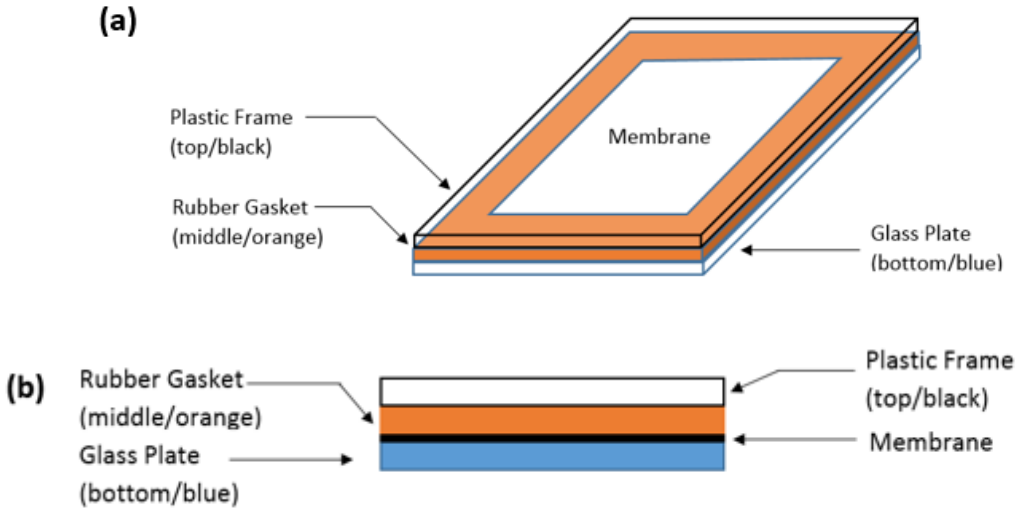

Fig.3.4: (a) Front view and (b) cross-sectional view of the membrane modification module employed in these studies.

3.3 REFERENCES

1. Miller, D. J.; Kasemset, S.; Wang, L.; Paul, D. R.; Freeman, B. D., Constant Flux Crossflow Filtration Evaluation of Surface-Modified Fouling-Resistant Membranes. *Journal of Membrane Science* **2014,** *452*, 171-183.

2. Kasemset, S.; He, Z.; Miller, D. J.; Freeman, B. D.; Sharma, M. M., Effect of Polydopamine Deposition Conditions on Polysulfone Ultrafiltration Membrane Properties and Threshold Flux During Oil/Water Emulsion Filtration. *Polymer* **2016,** *97*, 247-257.

3. Xie, W.; Geise, G. M.; Freeman, B. D.; Lee, H.-S.; Byun, G.; McGrath, J. E., Polyamide Interfacial Composite Membranes Prepared from M-Phenylene Diamine, Trimesoyl Chloride and a New Disulfonated Diamine. *Journal of Membrane Science* **2012,** *403-404*, 152-161.

4. Miller, D. J.; Kasemset, S.; Paul, D. R.; Freeman, B. D., Comparison of Membrane Fouling at Constant Flux and Constant Transmembrane Pressure Conditions. *Journal of Membrane Science* **2014,** *454*, 505–515.

5. Miller, D. J.; Paul, D. R.; Freeman, B. D., An Improved Method for Surface Modification of Porous Water Purification Membranes. *Polymer* **2014,** *55*, 1375–1383.

6. Standard Test Method for Molecular Weight Cutoff Evaluation of Flat Sheet Ultrafiltration Membranes. ASTM International: West Conshohocken, PA, 2001.

7. Singh, S.; Khulbe, K. C.; Matsuura, T.; Ramamurthy, P., Membrane Characterization by Solute Transport and Atomic Force Microscopy. *Journal of Membrane Science* **1998,** *142*, 111–127.

8. Kasemset, S.; Wang, L.; He, Z.; Miller, D. J.; Kirschner, A.; Freeman, B. D.; Sharma, M. M., Influence of Polydopamine Deposition Conditions on Hydraulic Permeability, Sieving Coefficients, Pore Size and Pore Size Distribution for a Polysulfone Ultrafiltration Membrane. *Journal of Membrane Science* **2017,** *522*, 100-115.

9. Zeman, L. J.; Zydney, A. L., *Microfiltration and Ultrafiltration: Principles and Applications*. Marcel Dekker, Inc.: New York, NY, 1996.

10. Opong, W. S.; Zydney, A. L., Diffusive and Convective Protein Transport through Asymmetric Membranes. *Aiche J.* **1991,** *37* (10), 1497–1510.

11. Zydney, A. L.; Aimar, P.; Meireles, M.; Pimbley, J. M.; Belfort, G., Use of the Log-Normal Probability Density Function to Analyze Membrane Pore Size Distributions: Functional Forms and Discrepancies. *Journal of Membrane Science* **1994,** *91* (3), 293-298.

12. Mehta, A.; Zydney, A. L., Permeability and Selectivity Analysis for Ultrafiltration Membranes. *Journal of Membrane Science* **2005,** *249* (1–2), 245-249.

13. Zhang, W.; Wahlgren, M.; Sivik, B., Membrane Characterization by the Contact Angle Technique: II. Characterization of UF-Membranes and Comparison between the Captive Bubble and Sessile Drop as Methods to Obtain Water Contact Angles. *Desalination* **1989,** *72* (3), 263-273.

14. He, Z.; Miller, D. J.; Kasemset, S.; Wang, L.; Paul, D. R.; Freeman, B. D., Fouling Propensity of a Poly(Vinylidene Fluoride) Microfiltration Membrane to Several Model Oil/Water Emulsions. *Journal of Membrane Science* **2016,** *514*, 659-670.

15. Miller, D. J.; Paul, D. R.; Freeman, B. D., A Crossflow Filtration System for Constant Permeate Flux Membrane Fouling Characterization. *Review of Scientific Instruments* **2013,** *84* (3), 035003.

16. Beier, S. P.; Jonsson, G., Critical Flux Determination by Flux-Stepping. *Aiche J.* **2010,** *56* (7), 1739-1747.

Chapter 4: Fouling mechanisms in constant flux crossflow ultrafiltration

4.1 MOTIVATION

Most fouling studies involve the constant pressure, dead-end filtration operation mode. Four fouling mechanisms of the Hermia model (complete pore blocking, intermediate pore blocking, cake filtration and standard pore blocking) have long been used to describe membrane filtration and fouling in constant transmembrane pressure (ΔP, TMP) operation of membranes.[1] Bowen used these models to identify the dominant fouling mechanism at different stages of microfiltration membrane fouling during BSA filtration.[2] Field *et al.* introduced a foulant removal term to Hermia's four mechanisms for constant ΔP, crossflow filtration.[3-5] However, most industrial filtrations are based on constant flux operation, and constant ΔP DEF filtration models are, therefore, not directly applicable.[6] Although there are a few models for fouling under constant flux—Ho and Zydney, for example, developed a constant flux DEF model for BSA protein fouling[7-8]—studies of fouling under constant flux crossflow filtration are still scarce.

In this study, we re-derived the Hermia model to describe fouling under constant flux, crossflow ultrafiltration.[9] We proposed a combined model that incorporated intermediate pore blocking (IPB) and cake filtration and can qualitatively describe fouling progression under these operating conditions.

---

* This chapter has been adapted with permission from sections of: Kirschner, A.Y.; Cheng, Y.H; Paul, D.R.; Field, R.W.; Freeman; B.D. Fouling mechanisms in constant flux crossflow ultrafiltration. *Journal of Membrane Science* **2019**, 574, 65-75. Kirschner wrote the manuscript and performed experimental and modeling work; Cheng performed experimental and modeling work and assisted with writing; Field, Paul, and Freeman advised the project and assisted with writing.

4.2 FOULING MECHANISMS

The fouling model for constant flux crossflow ultrafiltration is inspired by the classic Hermia model, which has a few key fundamental assumptions fundamental assumptions: (1) membrane pores are cylindrical, parallel to each other, and uniform in diameter, and (2) foulant particles are uniform, non-deformable spheres.[1] The Hermia model includes four distinct fouling mechanisms, each with its own unique assumptions in addition to these two common assumptions. *Complete pore blocking* (*cf.* Fig. 4.1(a)) assumes that fouling is a surface phenomenon, where foulant particles deposit only on unobstructed (clean) surface areas, and then completely block the pores in the covered area (the projection of particles onto the membrane surface). This fouling mechanism assumes that particles do not deposit on top of each other.[1] *Intermediate pore blocking* (*cf.* Fig. 4.1(b)) is similar to complete pore blocking, but particles are allowed to deposit on top of each other. Each foulant can deposit either on a clean area of the membrane or onto previously deposited foulant particles.[1] Complete pore blocking and intermediate pore blocking describe fouling as a decrease in filtration area, rather than a change in overall filter mass transfer resistance, so the overall mass transfer resistance was taken to be constant.[1] For *cake filtration* (*cf.* Fig. 4.1(c)), foulants completely cover a membrane surface in several layers. Based on Hermia model, the layers of particles that cover the entire membrane surface are defined as cake, which increases the overall mass transfer resistance. The increase in resistance is proportional to the cake layer thickness.[1] Finally, *standard pore blocking* (*cf.* Fig. 4.1(d)) is fundamentally different, assuming that blocking occurs only inside the pores, where deposited particles reduce the pore diameter and increase the mass transfer resistance of the membrane.[1]

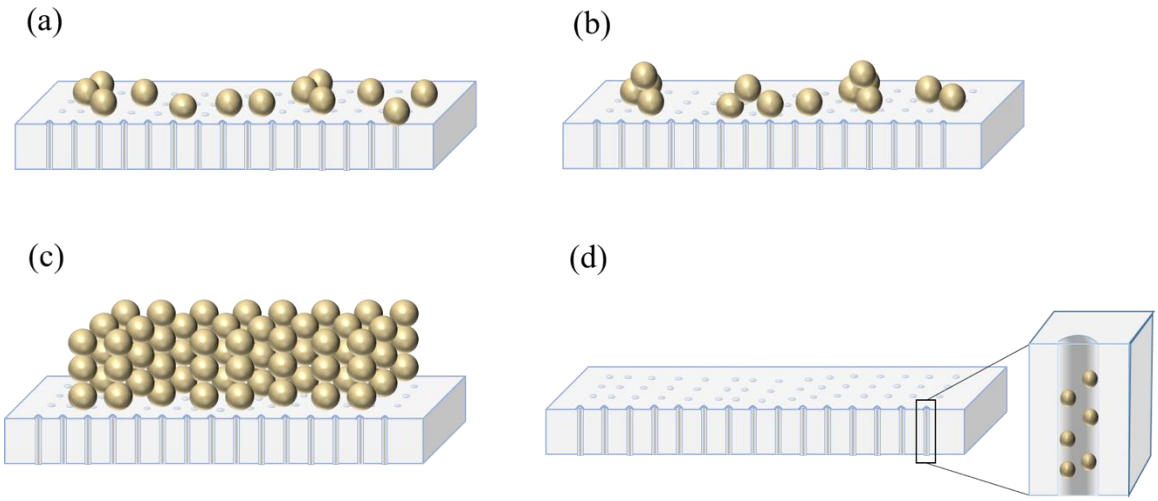

Fig. 4.1: Schematic representation of Hermia's fouling mechanisms: (a) Complete pore blocking, (b) Intermediate pore blocking, (c) Cake filtration and (d) Standard pore blocking.[1]

4.3 MODEL DEVELOPMENT

As mentioned above, this model is inspired by Hermia's model with modifications for a constant flux crossflow system. In this system, shear force from the feed flow may remove foulants from the membrane surface.[10] Field *et al.* include a crossflow foulant removal term in the surface fouling mechanisms (*i.e.*, complete pore blocking, intermediate pore blocking, and cake filtration).[5] Standard pore blocking assumes that fouling occurs in the membrane pores, so the addition of crossflow should not affect this fouling mechanism.[3] Constant flux refers to the volumetric flowrate divided by the pristine membrane surface area. As the membrane fouls, the open pore area decreases, causing the local flux through some pores to decrease while the flow through others increases to compensate. However, at all times the total flux through the entire membrane is constant.[11] A summary of the ΔP relations for all four fouling mechanisms is provided in Table 4.1.

4.3.1 Complete pore blocking

According to Darcy's Law for flow through a porous membrane:[1]

$$Q = \frac{\Delta P a}{\mu R} \qquad \textbf{4.1}$$

where Q is the volumetric flow rate [m^3/s], ΔP is transmembrane pressure [N/m^2], a is the clean (unobstructed, unfouled) membrane surface area [m^2], μ is the fluid viscosity [$N{\cdot}s/m^2$], and R is the overall filter mass transfer resistance [m^{-1}].

For constant flux, Q at time t=0 (Q_0) should equal Q at all time (Q_t). Following Hermia's assumption, the overall filter resistance is presumed constant, so the increase in ΔP during fouling is due to a reduction in unobstructed membrane surface area. Therefore, comparing the expressions for Q_0 and Q_t from Equation 4.1:

$$\Delta P_t = \frac{\Delta P_0 a_0}{a_t} \qquad \textbf{4.2}$$

where the subscripts 0 and t mean initial conditions and conditions at time t, respectively.

Based on Hermia's assumption of the complete pore blocking mechanism, the unobstructed membrane surface area is a function of the filtered volume of foulant solution:[1]

$$a_t = a_0 - \sigma V \qquad \textbf{4.3}$$

where V is the filtrate (*i.e.*, permeate) volume [m^3] that has passed through the membrane, and σ is the blocked membrane surface area per unit filtrate volume [m^{-1}].

In constant flux operation, the permeation flux will not change over time, and V can be expressed as the product of the initial flux, surface area and the filtration time:

$$V = Q_0 t = a_0 J t \qquad \textbf{4.4}$$

where J is the local permeate flux [m/s]. In this chapter, we assume local permeate flux is equal to the overall permeate flux, so J is a constant. The impacts of particle deposition on local permeate flux and fouling progression will be discussed in the next chapter. Substituting Equation 4.4 into Equation 4.3 and rearranging gives:

$$-\frac{da}{dt} = \sigma a_0 J \qquad \textbf{4.5}$$

Based on Field *et al.*, the rate of change in clean membrane surface area is a function of two counteracting processes: foulant deposition and foulant removal.[3, 5] Foulant removal is taken to be proportional to the blocked filtration area, and the particle resuspension rate per unit membrane area is proportional to the feed flowrate.[5] The decrease in unobstructed membrane surface area is given by:[5]

$$-\frac{da}{dt} = \sigma a_0 J - B(a_0 - a) \qquad \textbf{4.6}$$

where B is the particle resuspension rate, a constant reflecting the frequency of foulant removal from the membrane surface by the crossflow shear force [s^{-1}]. The first term on the right-hand side of Equation 4.6 is the foulant deposition term, and the second term is the foulant removal term.

Integration of Equation 4.6 yields the unobstructed membrane surface area as a function of time:

$$a_t = a_0\left(1 - \frac{\sigma J}{B}(1 - \exp(-Bt))\right) \qquad \textbf{4.7}$$

Substituting Equation 4.7 into Equation 4.2 results in:

$$\Delta P_t = \frac{\Delta P_0}{\left(1 - \frac{\sigma J}{B}(1 - \exp(-Bt))\right)} \qquad \textbf{4.8}$$

which is the ΔP for complete pore blocking as a function of time.

A simulation of Equation 4.8 is shown in Fig. 4.2(a). When the second term in the denominator of Equation 4.8, $\frac{\sigma J}{B}\left(1-\exp(-Bt)\right)$, is between 0 and 1, the model predicts a rise in ΔP with time. When this term equals 1, all pores have been blocked, and ΔP increases to infinity. Once this term is larger than 1, Equation 4.8 predicts a negative pressure, which is not reasonable.

Complete pore blocking was a reasonable mechanism for constant ΔP operation. When all pores are blocked, the permeate flowrate simply declines to zero. However, assuming constant flux with all pores completely blocked is not realistic. Although complete pore blocking predicts a reasonable ΔP profile at certain conditions, it is not universally applicable in a constant flux crossflow system.

4.3.2 Intermediate pore blocking (IPB)

As mentioned above, IPB allows particles to deposit on top of each other. The probability that a particle will deposit onto an open pore, rather than on a previously deposited particle, is proportional to the instantaneous clean membrane surface area.[1] The rate of change of clean membrane surface area is expressed by:

$$-\frac{da}{dt} = \sigma a J \qquad \textbf{4.9}$$

The only difference between Equation 4.9 and Equation 4.5 is the right-hand side of the equation. In intermediate pore blocking, each foulant particle has a probability to deposit either on clean surface area or on previously deposited foulant particles.[1] The probability of blocking unobstructed surface area decreases as more particles cover the membrane surface. Therefore, $\sigma a_0 J$ from Equation 4.5 is changed to $\sigma a J$ to account for the decreasing blocking rate during fouling.

In crossflow filtration, the foulant removal term is identical to that introduced for complete pore blocking (*cf.* Equation 4.6):

$$-\frac{da}{dt} = \sigma aJ - B(a_0 - a) \qquad \textbf{4.10}$$

Integration of Equation 4.10 yields the following expression for the unobstructed membrane surface area as a function of time:

$$a_t = a_0\left(\frac{1}{K_i} + \left(1 - \frac{1}{K_i}\right)\exp(-K_i Bt)\right) \qquad \textbf{4.11}$$

where K_i is the IPB constant for crossflow filtration and is defined as:

$$K_i = \frac{B + \sigma J}{B} \qquad \textbf{4.12}$$

Substitution of Equation 4.11 into Equation 4.2 results in:

$$\Delta P_t = \frac{\Delta P_0}{\left(\frac{1}{K_i} + \left(1 - \frac{1}{K_i}\right)\exp(-K_i Bt)\right)} \qquad \textbf{4.13}$$

which is IPB ΔP evolution as a function of time.

A simulation of Equation 4.13 is shown in Fig. 4.2(b). Equation 4.13 reveals no inconsistencies in constant flux operations like those found for complete pore blocking. The denominator of this equation is always positive, with a minimum value of $1/K_i$ and a maximum value of 1. The equation predicts an initial rise in ΔP, plateauing at long times to a constant value: $\Delta P_{t\to\infty} = \Delta P_o K_i$. The plateau in ΔP results from the decreasing probability of a foulant particle blocking unobstructed surface area as more and more of the membrane surface becomes covered. A balance between particle deposition and particle removal is reached, which does not violate the constant flux assumption.

4.3.3 Cake filtration

As mentioned above, the cake filtration expresses fouling as an increase in overall mass transfer resistance, rather than a decrease in unobstructed surface area. The overall filter resistance is the sum of the clean membrane resistance and the resistance of the cake.[1] An erosion term is added to account for removal of foulant layers due to crossflow:[3]

$$R_t = R_0 + \frac{\alpha W}{a_0} - \alpha S t \qquad \textbf{4.14}$$

where α is the cake specific resistance [m/kg], W is the cake mass [kg] and S is the rate of erosion of cake per unit area [kg/(m^2·s)], which is assumed to be invariant with time.[3]

Based on a mass balance on the cake:[1, 12]

$$W = \frac{V \gamma s}{(1 - ms)} \qquad \textbf{4.15}$$

where γ is the filtrate density [kg/m^3], s is the mass fraction of solids in the fouling solution, and m is the mass ratio of wet to dry cake.

Substitution of Equations 4.4 and 4.15 into Equation 4.14 results in an expression for overall filter resistance as a function of time:

$$R_t = R_0 (1 + K_c J t) \qquad \textbf{4.16}$$

where K_c is the cake filtration constant for crossflow filtration [m^{-1}], defined as:

$$K_c = \frac{\alpha \gamma s}{R_0 (1 - ms)} - \frac{\alpha S}{J R_o} \qquad \textbf{4.17}$$

Substitution of Equation 4.16 into Darcy's Law (Equation 4.1) yields:

$$\Delta P_t = \Delta P_0 \left(1 + K_c J t\right) \qquad \textbf{4.18}$$

which is ΔP for cake filtration as a function of time.

Equation 4.18 predicts a linear rise in ΔP with filtration time, as shown in Fig. 4.2(c). The assumption that the cake covers the entire membrane surface area cannot be true before the first layer of cake has deposited. The formation of the first layer of foulants depends on the permeate flux, crossflow rate, foulant concentration and filtration time. This assumption also implies that the cake filtration is more applicable when membranes are severely fouled.

4.3.4 Standard pore blocking

In contrast to the previously described fouling mechanisms, standard pore blocking assumes that fouling occurs *inside* the membrane pores rather than on the surface.[1]

Membrane permeate flow rate through straight cylindrical pores can be described using the Hagen-Poiseuille equation:[1, 13]

$$Q = N\left(\frac{\pi r^4 \Delta P}{8\mu L}\right) \qquad \textbf{4.19}$$

where N is the number of membrane pores, r is the pore radius [m], and L is the pore length (*i.e.*, membrane thickness) [m].

The standard pore blocking model expresses fouling as a decrease in membrane radii. Given that μ and L are constant, the relationship of ΔP_t to ΔP_0 is a function of the initial radius, r_0, and the radius at time t, r_t:

$$\Delta P_t = \left(\frac{r_0}{r_t}\right)^4 \Delta P_0 \qquad \textbf{4.20}$$

Following Hermia, a solids mass balance yields:[1]

$$N\pi(r_0^2 - r_t^2)L = CV \qquad \textbf{4.21}$$

where C is the volume of particles deposited per unit volume of filtrate [-]. Rearranging Equation 4.21 yields the desired ratio:

$$\left(\frac{r_t}{r_0}\right)^4 = \left(1 - \frac{CV}{N\pi L r_0^2}\right)^2 \qquad \textbf{4.22}$$

Defining the constant for standard pore blocking K_s [m^{-3}] as:

$$K_s = \frac{C}{N\pi L r_0^2} \qquad \textbf{4.23}$$

Substitution of Equation 4.22 into Equation 4.20 gives:

$$\Delta P_t = \frac{\Delta P_0}{\left(1 - K_s a_o J t\right)^2} \qquad \textbf{4.24}$$

which is the time dependence of ΔP for standard pore blocking.

A simulation of Equation 4.24 is shown in Fig. 4.2(d). Standard pore blocking occurs inside the pores, so it is not influenced by crossflow-induced forces. Consequently, Equation 4.24 is valid for both crossflow and dead-end operations. In Equation 4.24, $K_s a_o J t$ is always positive. Therefore, when $K_s a_o J t$ is between 0 and 1, the denominator will be smaller than 1, and a rise in ΔP with time is predicted. When $K_s a_o J t = 1$, all the pores have been blocked, and ΔP increases to infinity. When $K_s a_o J t > 1$, Equation 4.24 predicts a decrease in pressure over time, which is not reasonable.

Similar to complete pore blocking, a breakdown of the constant flux assumption occurs when all pores have been blocked by foulants. A correction should be made to account for removal of foulants inside the pore. As the pore radius decreases, the filtrate velocity through the remaining open area must increase to maintain constant flux. An increase in velocity will translate to stronger shear forces, which may remove previously deposited particles. Such a correction is beyond the scope of this paper, as standard pore

blocking is much more likely to be significant under conditions where the foulant particle size is smaller than the pore diameter, which is not the case for the work reported here.

Table 4.1: Summary of the relationships between ΔP and filtration time for the four proposed fouling mechanisms in constant permeate flux crossflow filtration.

Complete	**Intermediate**	**Cake**	**Standard**
$\Delta P_t = \frac{\Delta P_0}{\left(1-\frac{\sigma J}{B}(1-\exp(-Bt))\right)}$	$\Delta P_t = \frac{\Delta P_0}{\left(\frac{1}{K_i}+\left(1-\frac{1}{K_i}\right)\exp(-K_i Bt)\right)}$	$\Delta P_t = \Delta P_0\left(1+K_c Jt\right)$	$\Delta P_t = \frac{\Delta P_0}{\left(1-K_s a_o Jt\right)^2}$

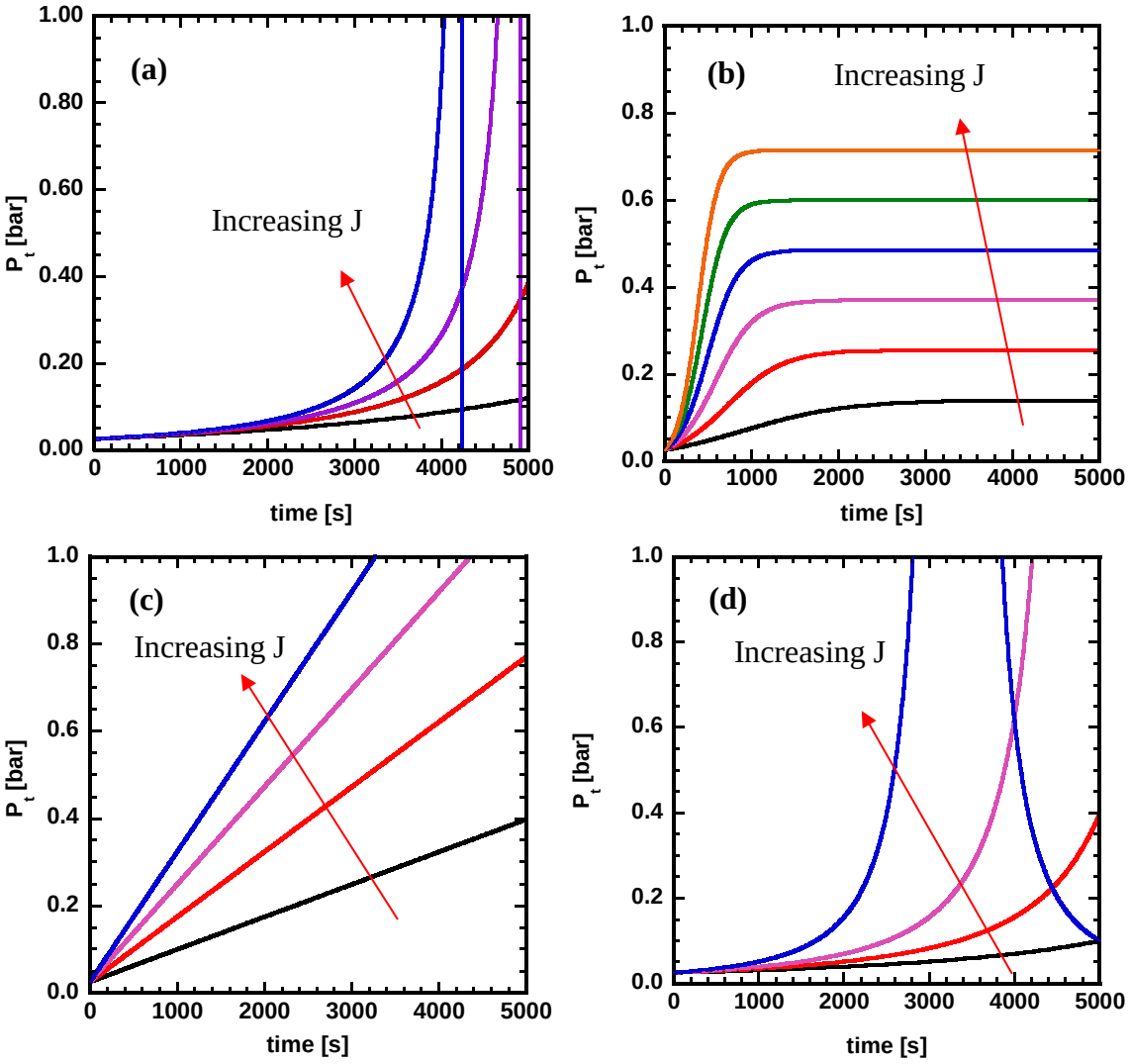

Fig. 4.2: Simulation of Hermia's fouling mechanisms after modifying for constant flux, crossflow filtration: (a) Complete pore blocking, (b) Intermediate pore blocking, (c) Cake filtration and (d) Standard pore blocking.[1]

4.4 RESULTS AND DISCUSSION

4.4.1 Constant flux crossflow fouling experiments

Constant flux crossflow fouling experiments were conducted at a 0.8 L/min crossflow rate, 200 ppm latex beads or soybean oil concentration, and permeate fluxes ranging from 20 LMH to 130 LMH in intervals of 10 LMH. Latex bead suspensions are often used as model foulants in fouling research because their physical properties match with the model assumptions of uniform, spherical, non-deformable foulant particles. In practice, foulants often do not meet these restrictions. For example, emulsified oil droplets, found in hydraulic fracturing wastewater, are deformable and can coalesce into larger droplets.[10] To investigate whether this non-ideality affects the applicability of fouling models to this class of foulants, soybean oil emulsions were used to model deformable foulants.

ΔP was monitored as a function of filtration time. To minimize the effect of permeance variation on model parameters, membrane samples selected carefully for constant flux crossflow experiments had permeance values as close to each other as possible. Membrane samples used with the latex bead suspension had permeance values ranging from 221 to 238 LMH/bar, with an average permeance of 228 ± 5 LMH/bar. Membrane samples used with the soybean oil emulsion had permeance values ranging from 227 to 238 LMH/bar, with an average permeance of 234 ± 4 LMH/bar. Latex bead rejection was 100%. Soybean oil rejection was 98.7 ± 0.3%. Representative results of the constant flux experiments for both foulants are presented in Fig. 4.3.

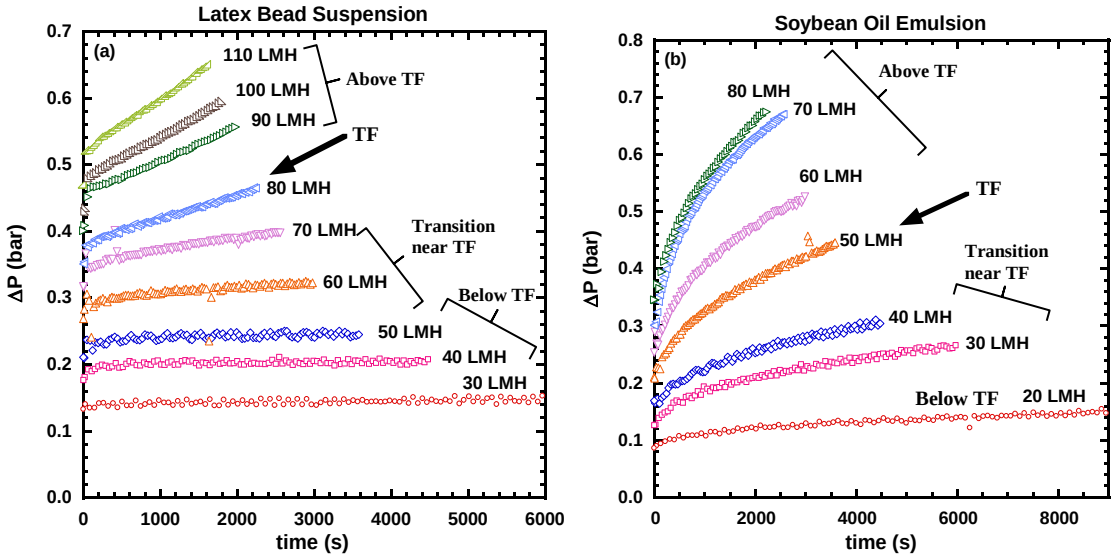

Fig. 4.3: Influence of filtration time on ΔP in constant flux fouling experiments conducted with: (a) 200 ppm 0.22 μm latex bead suspension and (b) 200 ppm soybean oil emulsion. TF - Threshold Flux.

As permeate flux increases, the ΔP of both foulants changes very slowly with time at low flux and rapidly increases at higher flux, particularly above the threshold flux (TF). The TF is the flux below which the membrane fouls slowly and above which the membrane fouls severely.[4, 14] As discussed in more detail below, TF values were measured using flux stepping experiments. The latex bead suspension had a TF value around 80 LMH, and the soybean oil emulsion had a TF value of around 50 LMH. Fig. 4.3(a) shows experimental results using latex bead suspension. The behavior of the ΔP profiles can be divided into three regimes: far below the TF, near but below the TF, and above the TF. For far below the TF regime (*i.e.*, 30 – 50 LMH), ΔP increases initially and then reaches a plateau with long filtration time (*cf.* Fig. 4.4(a)). These ΔP evolutions are similar to the IPB model simulation (*cf.* Fig. 4.2(a)). This result implies that IPB may be the dominant fouling mechanism far below TF. As the permeate flux approaches the TF (*i.e.*, 60 – 70 LMH), ΔP displays a more rapid initial increase with time, and it rises gradually at long filtration

times. Above the measured TF (*i.e.*, 90 – 110 LMH), there is a sharp increase in ΔP at the start, followed by an abrupt transition to a slower rate of increase in ΔP with time (*cf.* Fig. 4.4(b)). The gradual increase in ΔP at long filtration time is similar to the theoretical profile predicted by the cake filtration mechanism (*cf.* Fig. 4.2(c)), implying that cake filtration may be the dominant fouling mechanism and that the foulant cake continues to grow indefinitely. Under assumptions of constant flux filtration, constant crossflow rate and uniform foulant size, the net particle deposition rate is also constant. Evidence for this comes from the near linear increase in transmembrane pressure observed during the later stages of fouling experiments above the threshold flux.

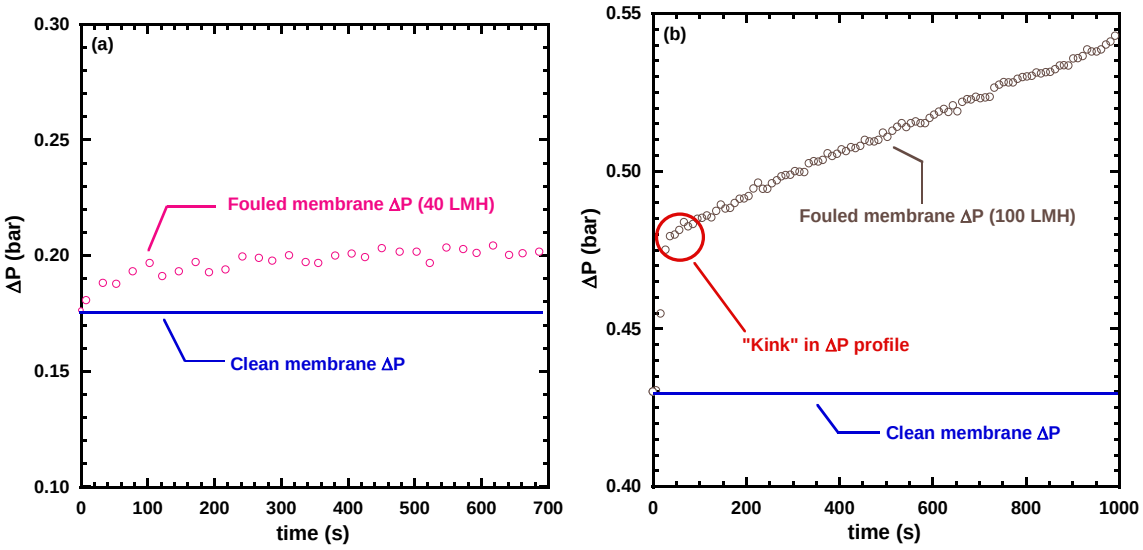

Fig. 4.4: Influence of filtration time on ΔP in constant flux fouling experiments conducted with 200 ppm 0.22 µm latex bead suspension: (a) close-up view of ΔP behavior at 40 LMH (below the TF), (b) close-up view of ΔP behavior at 100 LMH (above the TF).

Fig. 4.3(b) presents experimental results for the soybean oil emulsion. The TF of this foulant is around 50 LMH. At permeate fluxes approaching the TF of this foulant (*i.e.*, 30 – 40 LMH), ΔP profiles are similar to those of the latex bead suspension near but below its TF, which show an initial ΔP increase followed by a region of slower ΔP rise. However, above the TF of the soybean oil emulsion (*i.e.*, 60 – 80 LMH), the transition between the initial ΔP increase and the slow ΔP rise region is more gradual. Consequently, the ΔP profiles of the soybean oil emulsion do not display the "kink" seen in the latex bead suspension ΔP profiles. Furthermore, the slow ΔP rise region has a diminishing increase rate as opposed to a constant rate in latex bead experiments.

The difference between the ΔP profiles of the latex bead suspension and the soybean oil emulsion above the TF may come from at least two sources. First, in contrast to the complete rejection of latex bead suspension, soybean oil emulsion's rejection rate is not 100%. At high fluxes, emulsified oil droplets can deform and "squeeze" through membrane pores, even if they have a diameter larger than that of the membrane pores.[10] Second, oil droplets can coalesce into larger droplets, which are more easily removed from the surface of the membrane by the crossflow shearing force.[10] These two phenomena lead to foulant removal from the membrane surface, perhaps moderating the increase in ΔP, smoothing the transition from intermediate pore blocking to cake filtration.

In conclusion, ΔP profiles from constant flux tests (especially for the latex bead suspension) suggest that two fouling mechanisms are involved under this operation mode. At low permeate flux (relative to the TF), fouling is dominated by intermediate pore blocking, where the initial ΔP increase is followed by a plateau. At high fluxes (relative to the TF), the ΔP increases sharply at the start, but it reaches a region of approximately linear ΔP rise, which is more consistent with cake filtration (*cf.* Fig. 4.2(b)).

4.4.2 Combined intermediate pore blocking and cake filtration model

Based on the observations in section 4.4.2, a model combining intermediate pore blocking and cake filtration was proposed to describe the fouling results presented in Fig. 4.3. Standard pore blocking is expected to be negligible because the particle sizes (0.22 μm latex beads and ~3.4 μm oil droplets [15]) are much larger than the nominal membrane pore diameter (~3 nm) and rejection is high (100% for latex beads and >98% for oil droplets).

The combined model considers fouling to occur by both mechanisms simultaneously, but each mechanism dominates at different fouling stages. Before the first layer of cake forms (at the beginning of filtrations), intermediate pore blocking is dominant, transitioning over time to cake filtration. Equation 4.11 describes the reduction in unobstructed membrane surface area as the membrane initially fouls by intermediate pore blocking. During this initial intermediate pore blocking stage, the change of overall filter resistance is assumed negligible. Equation 4.16 describes the increase in total resistance as foulant layers accumulate on the membrane due to cake buildup. Comparing the initial and final flowrates using Darcy's Law (Equation 4.1) and substituting in Equations 4.11 and 4.16 results in:

$$\Delta P_t = \frac{\Delta P_0 (1 + K_c J t)}{\left(\frac{1}{K_i} + \left(1 - \frac{1}{K_i} \right) \exp(-K_i B t) \right)} \qquad \textbf{4.25}$$

which is the time dependence of ΔP for the combined model.

The exponential term in the denominator of Equation 4.25 decreases monotonically and approaches zero over time, so the intermediate pore blocking stage could be considered complete when this exponential term is small enough (0.01 in this study). The term K_i in Equations 4.13 and 4.25 is the ratio of the stable ΔP at the end of the intermediate pore blocking stage to the initial ΔP. Because the exponential term decreases much faster than

the cake filtration term (K_cJt) increases, the ΔP at the end of the intermediate pore blocking stage is the initial ΔP for cake filtration. The minimum value of K_i is 1, representing either zero flux through the membrane or very high foulant removal rate. In either case, fouling is negligible, and intermediate pore blocking does not contribute to ΔP.

K_c in Equations 4.18 and 4.25 represents the rate of accumulation of cake on the membrane. When K_c is small (*i.e.*, $(1+K_cJt)\approx 1$), Equation 4.25 reduces to Equation 4.13, the intermediate pore blocking equation. If both K_i and K_c are at their minimum values, ΔP is constant and equal to ΔP_0.

When t is close to 0 (At the start of membrane filtrations), the numerator of Equation 4.25 approaches one (*i.e.*, $(1+K_cJt)\approx 1$), and Equation 4.25 reduces to Equation 4.13 for pure intermediate pore blocking behavior. At long times ($t\to\infty$), the exponent in the denominator approaches zero (*i.e.*, $\exp(-K_iBt)\approx 0$) and Equation 4.25 becomes:

$$\Delta P_t = \Delta P_0 K_i (1+K_cJt) \qquad \textbf{4.26}$$

Equation 4.26 predicts a linear increase with time, which is similar to the cake filtration prediction. As described in Section 4.3.2, the intermediate pore blocking always converges to a constant value of $\Delta P_0 K_i$. Afterwards, ΔP becomes steady or increases linearly with time, following the cake filtration model. This time-dependent behavior is at least qualitatively consistent with the fouling progression observed in Fig. 4.2. Initially, the pristine membrane is fouled according to the intermediate pore blocking mechanism. After some time has passed and enough foulant has accumulated on the membrane as the first layer of cake, ΔP becomes controlled by the rate of cake buildup.

4.4.3 Modeling

Model fittings were done by the least squares method using Matlab R2019b® software. First, B, K_i and K_c were allowed to vary (three-parameter fitting), and σ was calculated according to the values. For three-parameter fitting, σ values have large variances, ranging from 31 to 613 m^{-1}. However, σ is expected to remain constant with flux for rigid foulant (latex beads), so this variation is most likely an artifact of the fitting algorithm. Allowing three dependent parameters to be varied independently does not yield a unique and physically meaningful set of parameter values. Therefore, a stricter fitting method was used after the three parameters fitting. According to the combined model, ΔP should rise approximately linearly later in the experiment, and the slope should equal $\Delta P_0 K_i K_c J$ (*cf.* Equation 4.26). Combining this expression for the slope and Equation 4.12, K_c can be expressed in terms of B as follows:

$$K_c = \frac{slope \cdot B}{\Delta P_o (B + \sigma J) J} \qquad \textbf{4.27}$$

K_i and K_c were expressed in terms of B and σ using Equations 4.12 and 4.27, respectively, and the model was fit to experimental data by treating B as the only adjustable parameter.

To determine the optimum value for σ, a grid search method was used.[16] B was allowed to vary to fit the ΔP vs. time data for each flux, and the values of K_i and K_c were calculated according to Equations 4.12 and 4.27, respectively. σ values ranged from 0 to 600 m^{-1} in intervals of 50 m^{-1}. A sum of the fitting errors for all tested fluxes was calculated to determine the best value of σ. More details can be found in another publication from our lab.[9]

The above description applies to the non-deformable latex beads. For the deformable oil droplets, σ is not expected to remain invariant with flux. The shape of deposited oil droplets may change with different hydraulic conditions.[17] Therefore, both σ

and B were allowed to vary during the second stage of fitting for the soybean oil emulsion fouling experiments.

Fig. 4.5 compares the model fits with the experimental data for representative constant flux experiments. The model parameters are summarized in Table 4.2 to Table 4.4. At fluxes far below the TF (*i.e.*, 20 and 40 LMH for the latex beads and 20 LMH for the soybean oil emulsion), both the intermediate pore blocking model and the combined model fit the data well, and the intermediate pore blocking model by itself is sufficient to describe the data. (The fitting curves using the combined model far below the TF are not presented in Fig. 4.5(a) because they would overlap with fitting curves of the intermediate pore blocking model.) All K_c terms in the combined model are close to zero at low permeate flux, and the combined model equation can be reduced to the intermediate pore blocking equation. As the flux approaches the TF and goes above it (60, 80, 100 and 120 LMH for the latex beads, and 40, 60, 80, and 100 LMH for the soybean oil emulsion), the combined model is required for an accurate fit. For comparison, attempts were made to fit the experimental data using only the intermediate pore blocking (*cf.* Equation 4.13) or cake filtration (*cf.* Equation 4.18) models (Fig. 4.6). These fouling models were unable to accurately describe the experimental data, which supports the qualitative description of fouling proposed in Section 4.4.2.

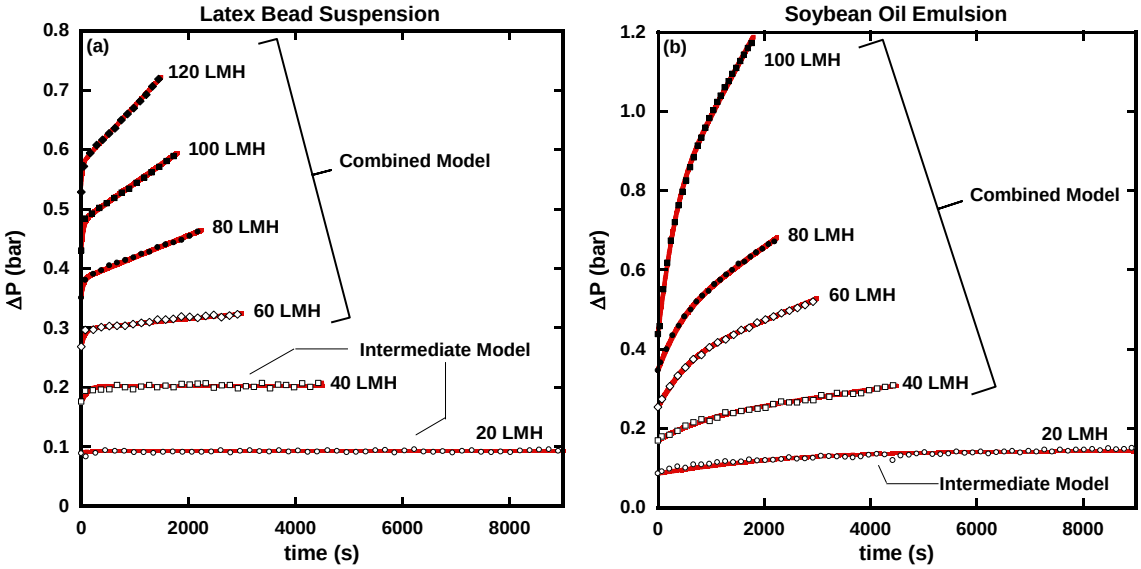

Fig. 4.5: Model fits for constant flux experiments conducted with: (a) 200 ppm 0.22 µm latex bead suspensions (TF ~80 LMH) and (b) 200 ppm soybean oil emulsions (TF ~50 LMH). Experimental data are shown with markers. Model fits are shown with red curves.

Table 4.2: Fitted parameter values used for model plots in Fig. 4.5(a). The intermediate pore blocking model is used for low permeate flux fitting (20-50 LMH), and the rest is fitted with the combined model.

Flux (LMH)	**B (s^{-1})**	**K_i**	**K_c (m^{-1})**
20	0.014	1.04	
30	0.010	1.08	
40	0.007	1.15	
50	0.009	1.15	
60	0.015	1.11	1.73
70	0.017	1.11	2.70
80	0.025	1.09	4.32
90	0.018	1.14	4.38
100	0.024	1.11	4.80
110	0.029	1.10	5.03
120	0.037	1.09	5.05
130	0.052	1.07	5.43

Table 4.3: Fitted parameter values when all data in Fig. 4.5(a) is fitted with the combined model.

Flux (LMH)	**B (s^{-1})**	**K_i**	**K_c (m^{-1})**
20	0.018	1.03	0.35
30	0.016	1.05	1.04
40	0.008	1.14	0.44
50	0.011	1.12	1.03
60	0.015	1.11	1.73
70	0.017	1.11	2.70
80	0.025	1.09	4.32
90	0.018	1.14	4.38
100	0.024	1.11	4.80
110	0.029	1.10	5.03
120	0.037	1.09	5.05
130	0.052	1.07	5.43

Table 4.4: Fitted parameter values used for model plots in Fig. 4.5(b).

Flux (LMH)	B (s^{-1})	K_i	K_c (m^{-1})	σ (m^{-1})
20	0.0003	1.66		43
30	0.001	1.46	9.13	81
40	0.001	1.30	7.94	32
50	0.002	1.39	10.86	55
60	0.002	1.43	9.00	48
70	0.002	1.53	9.45	64
80	0.002	1.36	9.04	36
90	0.003	1.42	11.22	52
100	0.003	1.71	11.85	73

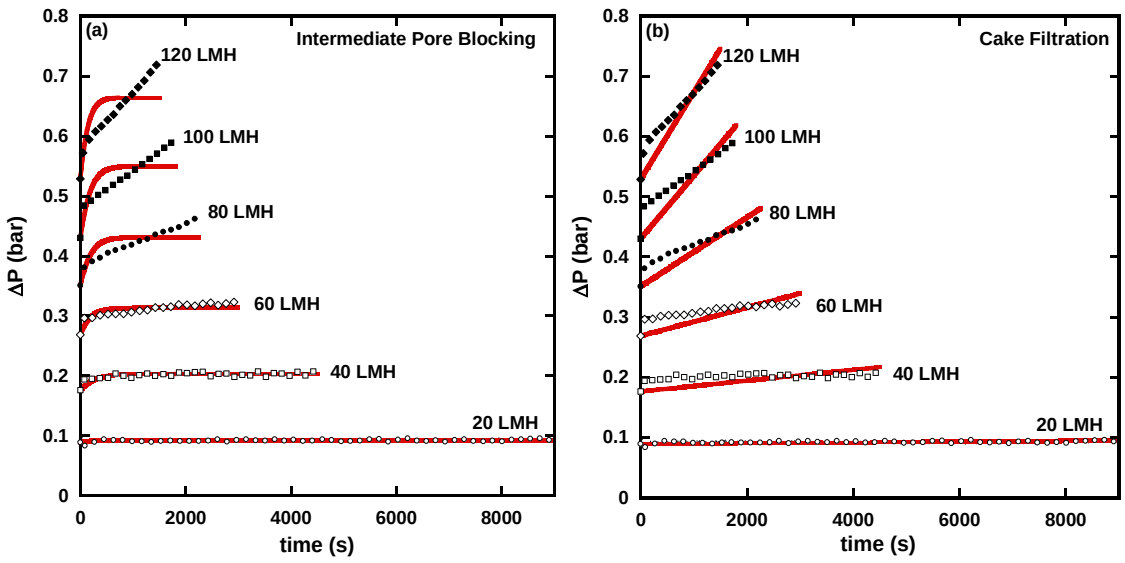

Fig. 4.6: Comparison of experimental data with model fits for constant flux filtration of a 200 ppm 0.22 µm latex bead suspension with: (a) intermediate pore blocking model (Equation 4.13) and (b) cake filtration model (Equation 4.18). Experimental data are shown with markers. Model fits are shown with red curves. The threshold flux was estimated to be 80 LMH.

4.4.4 Refining the definition of threshold flux

As mentioned in Chapter 3, TF is often measured by doing a flux stepping experiment.[18-19] Flux stepping was originally developed to investigate fouling in membrane bioreactor (MBR) systems.[20] Miller *et al.* adapted the method for constant flux crossflow fouling studies.[21]

As discussed above, both the combined model and the intermediate pore blocking model can describe the experimental data far below the TF, while near and above the TF, the combined model must be used. Furthermore, K_c values began increasing rapidly around the TF (*cf.* Fig. 4.7) if all the data is fitted with the combined model, which also indicates a fouling mechanism transition around the TF. Therefore, we propose the following physical definition of the TF in constant flux crossflow filtration: *the flux below which cake buildup is negligible and above which cake filtration becomes the dominant fouling mechanism*. Below the TF, ΔP is steady except for the beginning of filtrations. The steady pressure implies that the foulant removal rate of feed flow is equal to the foulant deposition rate of permeate flow. Crossflow shear force prevents the cake from growing thick enough to strongly influence ΔP. Above the TF, fast foulant deposition onto the membrane overwhelms foulant removal by crossflow shear, and the cake grows and contributes significantly to the continuous rise in ΔP with filtration time.

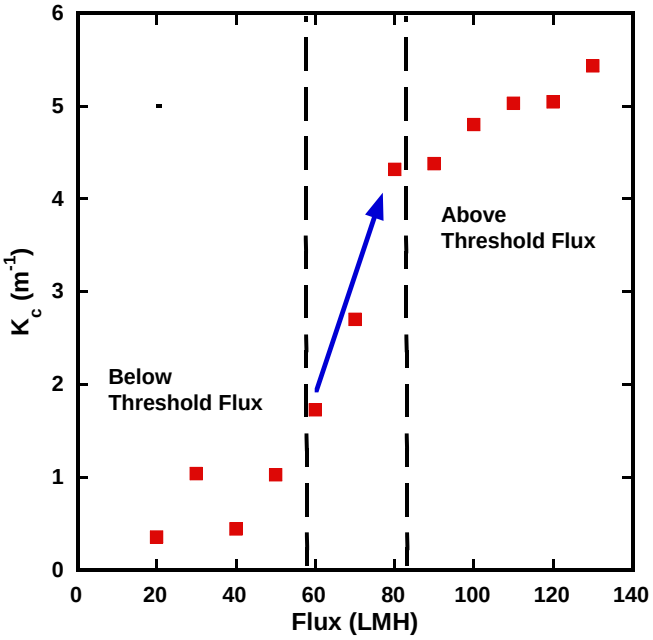

Fig. 4.7: Influence of permeate flux on K_c when all latex bead data are fitted with the combined model. The dashed lines and blue arrow indicate the transition region approaching the threshold flux, which was 80 LMH in this case.

Fig. 4.8(a) presents the results of a flux stepping experiment conducted with the latex bead suspension, as well as a simulation. Details of the flux stepping simulation can be found in section 4.4.4.4. Three common methods for determining the TF are discussed below in the context of our proposed definition of TF. A more thorough explanation is provided through a mathematical analysis of each method, using the combined intermediate pore blocking and cake filtration model. Only the first step in the flux stepping experiment is affected by intermediate pore blocking, because it is the only step in which the membrane surface is initially clean. Therefore, the mathematical analysis assumes that the fouling time is long enough where cake filtration (Equation 4.26) is applicable.

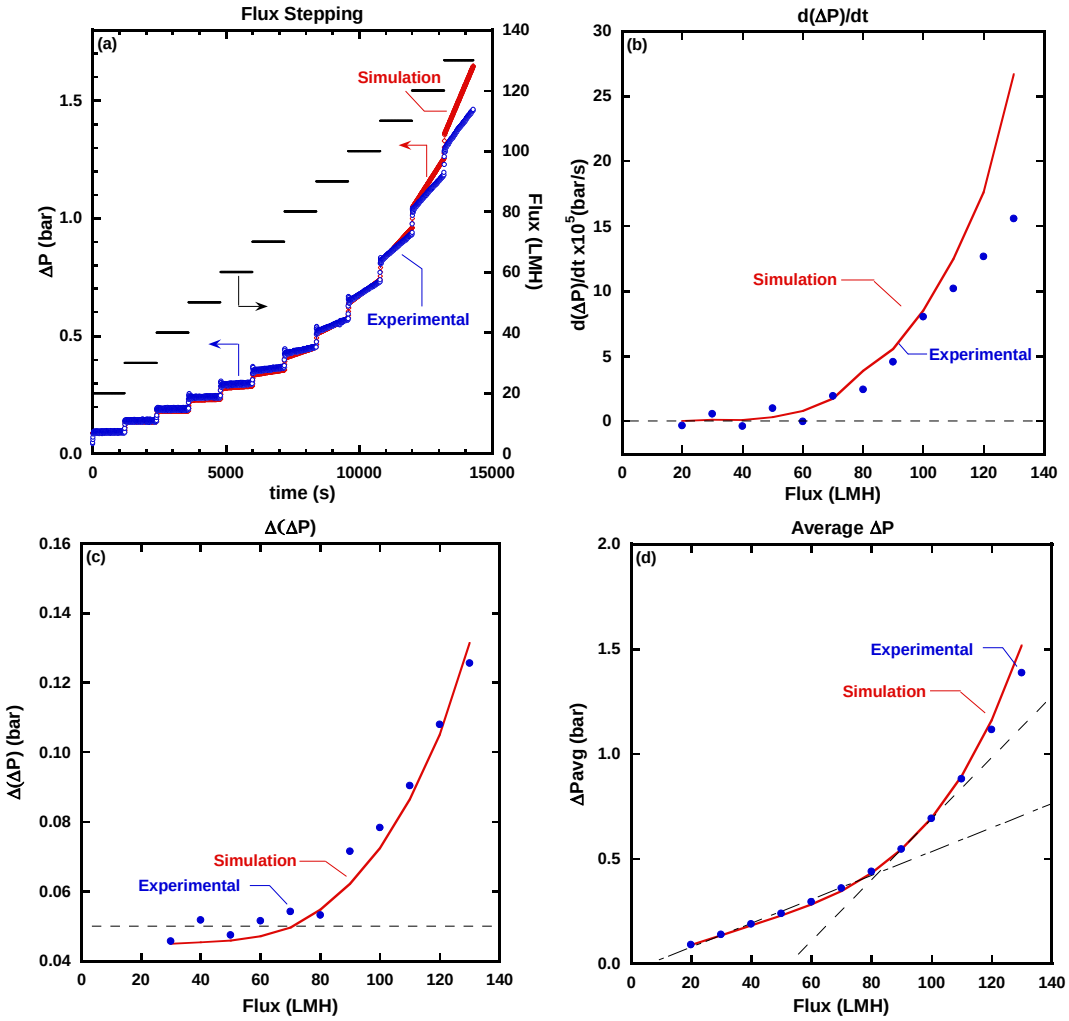

Fig. 4.8: Flux stepping experiments and analysis to determine TF: (a) ΔP and flux vs. time data for a flux stepping experiment conducted with a 200 ppm 0.22 µm latex bead suspension and a flux stepping simulation based on constant flux model fits. Analysis of experimental and simulated data using: (b) d(ΔP)/dt method, (c) $\Delta(\Delta P)$ method and (d) Average ΔP method.

4.4.4.1 d(ΔP)/dt:

In this method, the slope (d(ΔP)/dt) of increasing ΔP (excluding the initial jump) during each step is calculated. The value of d(ΔP)/dt for each step is plotted vs. permeate flux, and the TF is identified as the flux where d(ΔP)/dt begins to increase rapidly.[18, 20-21]

This method corresponds to the definition of the TF as marking the transition between slow and rapid fouling.

Taking the derivative with time of Equation 4.26:

$$\frac{d(\Delta P)}{dt} = \Delta P_0 K_i K_c J \qquad \textbf{4.28}$$

Based on constant flux fitting results (*cf.* Table 4.2 and 4.3), K_i for the latex bead fouling experiments was constant at ~1.1. The permeate flux is $\approx O\,(10^{-5}\ m/s)$. As a result, d(*ΔP*)/dt≈0 when K_c is small (*i.e.*, negligible cake accumulation). Either an increase in permeate flux or K_c contributes to a rise in d (*ΔP*) /dt. In flux stepping, permeate flux increases in a step-wise fashion, while d(*ΔP*)/dt remains more or less constant below the TF. Thus, a rapid increase in d(*ΔP*)/dt depends on an increase in K_c.

According to Table 4.3 and Fig. 4.7, K_c values increase sharply from around zero below the TF to ~4.3 at the TF (80 LMH). This result is consistent with the experimental results shown in Fig. 4.8(b), where d(*ΔP*)/dt values are near zero at low fluxes and begin to increase rapidly around 60 LMH. Above the TF, K_c begins to reach a plateau, and d(*ΔP*)/dt values increase more linearly with increases in permeate flux.

4.4.4.2 Δ(ΔP):

When permeate flux increases in a flux stepping experiment, the *ΔP* profile shows a corresponding sharp increase right after the increase in permeate flux (*cf.* Fig. 4.5(a)). The step increment is constant (10 LMH), so the increase in *ΔP* between steps should be constant if there is no change in fouling behavior. *Δ*(*ΔP*) is calculated as the difference between the first *ΔP* measurement of a new step (n+1) and the last *ΔP* measurement of old step n. In our experiments, the first measurement in step n+1 is taken 120 seconds after the

flux increase to give ΔP time to stabilize. $\Delta(\Delta P)$ values are then plotted vs. permeate flux, and the TF is identified as the flux where $\Delta(\Delta P)$ increases rapidly.[18, 20-21]

Using Equation 4.26, the ΔP difference between the first measurement of step n+1 and the last measurement of step n is:

$$\begin{aligned}\Delta(\Delta P) &= \Delta P_{initial}^{n+1} - \Delta P_{final}^{n} \\ &= \Delta P_0^{n+1} K_i^{n+1}(1 + K_c^{n+1} J^{n+1} t_{initial}^{n+1}) - \Delta P_0^{n} K_i^{n}(1 + K_c^{n} J^{n} t_{final}^{n})\end{aligned} \qquad \textbf{4.29}$$

At small values of K_c, the second terms in the parentheses are negligible, and Equation 4.29 becomes:

$$\Delta(\Delta P) = \Delta P_0^{n+1} K_i^{n+1} - \Delta P_0^{n} K_i^{n} \qquad \textbf{4.30}$$

K_i is taken as a constant, as mentioned above. The initial ΔP of each step is replaced with the flux divided by the membrane permeance at the end of step n, $permeance^n$ (*cf.* Equation 3.1) (assuming a negligible change in permeance during the time between measurements):

$$\Delta(\Delta P) = K_i \frac{\left(J^{n+1} - J^{n}\right)}{permeance^n} \qquad \textbf{4.31}$$

A constant of 1.1 is used for K_i (see Section 4.4.4.1). The difference between consecutive flux steps is 10 LMH. During the first flux steps, fouling is low, and permeance is taken to be constant (~230 LMH/bar, which is the clean membrane permeance). Using these values, $\Delta(\Delta P) \approx 0.0478\ bar$. When K_c becomes large enough that the second terms in parentheses of Equation 4.29 are not negligible, $\Delta(\Delta P)$ begins to rise. This result is consistent with the experimental results shown in Fig. 4.8(c). Below the TF, $\Delta(\Delta P)$ values are ≈ 0.05 bar, and they begin to increase around the TF (80 LMH).

4.4.4.3 Average ΔP:

The average ΔP for each flux step is calculated and plotted vs. permeate flux. A linear trend line is plotted through the data until the point where the R^2 value of the best fit of a line through the data is lower than 0.99.[22-23] A second linear trend line is then plotted through the next two points. As shown in Fig. 4.8(d), the TF is identified as the point of intersection of these two lines.

The running time average of ΔP, ΔP_{avg}, may be calculated by averaging Equation 4.26 over a step time interval Δt, as shown below:

$$\Delta P_{avg} = \frac{1}{\Delta t}\int_{t}^{t+\Delta t} \Delta P_0 K_i (1 + K_c J t')dt' = \Delta P_0 K_i (1 + K_c J t + 0.5 K_c J \Delta t) \qquad \textbf{4.32}$$

Substituting ΔP_0 according to Equation 3.1:

$$\Delta P_{avg} = \frac{K_i}{permeance}(J + K_c J^2 t + 0.5 K_c J^2 \Delta t) \qquad \textbf{4.33}$$

For small values of K_c, Equation 4.33 reduces to: $\Delta P_{avg} = \frac{K_i J}{permeance}$. At low fluxes, fouling is low, and permeance is taken to be constant (~230 LMH/bar). Therefore, at low fluxes, ΔP_{avg} is a linear function of flux. For larger K_c values, ΔP_{avg} in Equation 4.33 deviates from linearity. This result is consistent with the experimental results shown in Fig. 4.8(d) and with our proposed definition of the TF.

4.4.4.4 Threshold flux prediction

The proposed definition of TF is *the flux below which cake buildup is negligible and above which cake filtration becomes the dominant fouling mechanism*. This definition is consistent with the current three empirical methods of identifying the TF discussed above. To further support the proposed new definition, a flux stepping experiment was simulated based on fitting results for the constant flux latex bead suspension fouling

experiments (*cf.* Table 4.3). Because the membrane is clean and the permeate flux is below the TF during the first step (20 LMH), ΔP for the first flux step was calculated using only the intermediate pore blocking model:

$$\Delta P_t = \frac{\Delta P_0^{n=1}(the.)}{\left(\frac{1}{K_i} + \left(1 - \frac{1}{K_i}\right)\exp(-K_i B t)\right)} \qquad \textbf{4.34}$$

where $\Delta P_0^{n=1}(the.)$ is the theoretical initial ΔP of the first flux step, which was calculated:

$$\Delta P_0^{n=1}(the.) = \frac{J_{initial}}{Permeance} \qquad \textbf{4.35}$$

B and K_i values were taken from fitting the 20 LMH constant flux experiment with the combined model (*cf.* Table 4.3).

Following 20 minutes of filtration, the membrane should have experienced some fouling. Therefore, model fittings after the first step are done according to:

$$\Delta P_t = \Delta P_0^n \left[1 + K_c^n J^n (t - t_{end}^{n-1})\right] \qquad \textbf{4.36}$$

where n is the number of the current flux step. $\Delta P_{0,n}$ is the initial ΔP of step n. Calculation of $\Delta P_{0,n}$ is explained below. The following equations detail the simulation of a single flux step from step n to step n+1.

The instantaneous permeance of the fouled membrane at the end of step n was calculated according to:

$$Permeance^n(end) = \frac{J^n}{\Delta P_{t(end)}^n} \qquad \textbf{4.37}$$

The theoretical initial ΔP for step n+1 was calculated by substituting the permeance calculated in Equation 4.37 into:

$$\Delta P_0^{n+1} = \frac{J^{n+1}}{Permeance^n(end)} \qquad \textbf{4.38}$$

The theoretical ΔP jump due to the increase in permeate flux is:

$$\Delta(\Delta P)_{n\to n+1} = \Delta P_0^{n+1} - \Delta P_{t(end)}^n \qquad \textbf{4.39}$$

The ΔP jump typically spanned ~20 seconds from the moment the permeate flux was increased. Therefore, $\Delta(\Delta P)_{n\to n+1}$ was divided by 20 and added linearly to ΔP_t over 20 seconds to simulate the flux step.

The ΔP at the end of those 20 seconds was equal to the initial ΔP of permeate flux step n+1 (*i.e.*, ΔP_0^{n+1}). Calculation of ΔP_t then followed Equation A.4 using K_c values from Table 4.3. All following flux steps were simulated similarly, using the appropriate fluxes and K_c values from Table 4.3. The final simulation result is presented in Fig. 4.8(a).

Clearly, the simulation is at least qualitatively consistent with the experiments. At higher permeate fluxes (*i.e.*, 110-130 LMH) there is a more significant divergence between the simulation and experimental results. This deviation may be due to the effect of fouling history and error propagation from previous steps. The simulation is based on the fitted parameters from constant flux experiments, which are based on the fouling progression of a pristine membrane. In a flux stepping experiment, the surface has been gradually exposed to foulant at lower fluxes and some cake has accumulated prior to reaching high permeate fluxes. Cake packing may depend on permeate flux, and during the flux stepping experiment, the cake structure may evolve differently, thereby influencing fouling rates at higher fluxes.

In conclusion, the models could theoretically be applied to flux stepping data to predict the change in ΔP with filtration time during fouling for rigid particles. The first flux step is modelled using only intermediate pore blocking, and data from this experiment can

be used to calculate K_i (Equation 4.13). In subsequent steps, the slope of each step can be calculated from the experimental data. Using the slope and K_i values, we can calculate K_c for each step (Equation 4.26). Although the combined model (Equation 4.25) requires the value of B, the duration of the initial rapid ΔP rise is typically short, and Equation 4.26 should give a good estimate of ΔP during constant flux fouling.

Table 4.5: List of symbols (Chapter 4)

NOMENCLATURE	
SYMBOL	**DEFINITION & UNITS**
a	Unobstructed membrane surface area [m^2]
B	Particle resuspension rate [s^{-1}]
C	Volume of solid particles retained per unit filtrate volume
C_p	Organic carbon concentration in the permeate [mg/L]
C_f	Organic carbon concentration in the feed [mg/L]
J	Permeate flux [m/s]
K_j	Constant depending on fouling mechanism: j= i (intermediate), s (standard), c (cake)
L	Pore length (membrane thickness) [m]
m	Mass ratio of wet to dry cake
n	Step number in flux stepping experiment
N	Number of membrane pores
ΔP	Transmembrane pressure [N/m^2]
Q	Flow rate [m^3/s]
R	Overall filter resistance [m^{-1}]
r	Pore radius [m]

Table 4.5, continued.

s	Mass fraction of solids in the fouling solution
S	Rate of erosion of cake per unit area [kg/(m^2·s)]
t	Filtration time [s]
t*	Time at which the intermediate pore blocking stage is predicted to end [s]
TF	Threshold flux [L/(m^2·h)]
V	Filtrate volume [m^3]
W	Cake mass [kg]
α	Cake specific resistance [m/kg]
γ	Filtrate density [kg/m^3]
μ	Fluid viscosity [N·s/m^2]
σ	Blocked area per unit filtrate volume [m^{-1}]
Superscript - X^N	Superscript N indicates the step number that parameter X is being examined at, where X can be K_j, ΔP_0, J, permeance, or t.

4.5 REFERENCES

1. Hermia, J., Constant Pressure Blocking Filtration Laws – Application to Power-Law Non-Newtonian Fluids. *Transactions of the American Institute of Chemical Engineers* **1982,** *60*, 183–187.

2. Bowen, W. R.; Calvo, J. I.; Hernández, A., Steps of Membrane Blocking in Flux Decline During Protein Microfiltration. *Journal of Membrane Science* **1995,** *101* (1), 153-165.

3. Field, R. W.; Wu, D.; Howell, J. A.; Gupta, B. B., Critical Flux Concept for Microfiltration Fouling. *Journal of Membrane Science* **1995,** *100* (3), 259-272.

4. Field, R. W.; Pearce, G. K., Critical, Sustainable and Threshold Fluxes for Membrane Filtration with Water Industry Applications. *Advances in Colloid and Interface Science* **2011,** *164* (1), 38-44.

5. Field, R. W.; Wu, J. J., Modelling of Permeability Loss in Membrane Filtration: Re-Examination of Fundamental Fouling Equations and Their Link to Critical Flux. *Desalination* **2011,** *283*, 68-74.

6. The AWWA Subcommittee On Periodical Publications Of The Membrane Process, Microfiltration and Ultrafiltration Membranes for Drinking Water. *Journal (American Water Works Association)* **2008,** *100* (12), 84-97.

7. Ho, C. C.; Zydney, A. L., A Combined Pore Blockage and Cake Filtration Model for Protein Fouling During Microfiltration. *Journal of Colloid and Interface Science* **2000,** *232* (2), 389-399.

8. Ho, C. C.; Zydney, A. L., Transmembrane Pressure Profiles During Constant Flux Microfiltration of Bovine Serum Albumin. *Journal of Membrane Science* **2002,** *209* (2), 363-377.

9. Kirschner, A. Y.; Cheng, Y. H.; Paul, D. R.; Field, R. W.; Freeman, B. D., Fouling Mechanisms in Constant Flux Crossflow Ultrafiltration. *Journal of Membrane Science* **2019,** *574*, 65-75.

10. Tummons, E. N.; Tarabara, V. V.; Chew, Jia W.; Fane, A. G., Behavior of Oil Droplets at the Membrane Surface During Crossflow Microfiltration of Oil–Water Emulsions. *Journal of Membrane Science* **2016,** *500*, 211-224.

11. Le-Clech, P.; Chen, V.; Fane, T. A. G., Fouling in Membrane Bioreactors Used in Wastewater Treatment. *Journal of Membrane Science* **2006,** *284* (1), 17-53.

12. Ruth, B. F., Studies in Filtration III: Derivation of General Filtration Equations. *Industrial & Engineering Chemistry* **1935,** *27* (6), 708-723.

13. Baker, R. W., *Membrane Technology and Applications*. Third ed.; John Wiley & Sons Ltd.: West Sussex, UK, 2012.

14. Kirschner, A. Y.; Chang, C.-C.; Kasemset, S.; Emrick, T.; Freeman, B. D., Fouling-Resistant Ultrafiltration Membranes Prepared via Co-Deposition of Dopamine/Zwitterion Composite Coatings. *Journal of Membrane Science* **2017,** *541*, 300-311.

15. He, Z.; Miller, D. J.; Kasemset, S.; Wang, L.; Paul, D. R.; Freeman, B. D., Fouling Propensity of a Poly(Vinylidene Fluoride) Microfiltration Membrane to Several Model Oil/Water Emulsions. *Journal of Membrane Science* **2016,** *514*, 659-670.

16. Bevington, P. R.; Robinson, D. K., *Data Reduction and Error Analysis for the Physical Sciences*. 3rd ed.; The McGraw-Hill Companies, Inc.: New York, NY, 2003.

17. Fux, G.; Ramon, G. Z., Microscale Dynamics of Oil Droplets at a Membrane Surface: Deformation, Reversibility, and Implications for Fouling. *Environmental Science & Technology* **2017,** *51* (23), 13842-13849.

18. Beier, S. P.; Jonsson, G., Critical Flux Determination by Flux-Stepping. *AIChE Journal* **2010,** *56* (7), 1739-1747.

19. Bacchin, P.; Aimar, P.; Field, R. W., Critical and Sustainable Fluxes: Theory, Experiments and Applications. *Journal of Membrane Science* **2006,** *281*, 42–69.

20. Le Clech, P.; Jefferson, B.; Chang, I. S.; Judd, S. J., Critical Flux Determination by the Flux-Step Method in a Submerged Membrane Bioreactor. *Journal of Membrane Science* **2003,** *227* (1–2), 81-93.

21. Miller, D. J.; Kasemset, S.; Wang, L.; Paul, D. R.; Freeman, B. D., Constant Flux Crossflow Filtration Evaluation of Surface-Modified Fouling-Resistant Membranes. *Journal of Membrane Science* **2014,** *452*, 171-183.

22. Kasemset, S.; He, Z.; Miller, D. J.; Freeman, B. D.; Sharma, M. M., Effect of Polydopamine Deposition Conditions on Polysulfone Ultrafiltration Membrane Properties and Threshold Flux During Oil/Water Emulsion Filtration. *Polymer* **2016,** *97*, 247-257.

23. Luo, J.; Morthensen, S. T.; Meyer, A. S.; Pinelo, M., Filtration Behavior of Casein Glycomacropeptide (Cgmp) in an Enzymatic Membrane Reactor: Fouling Control by Membrane Selection and Threshold Flux Operation. *Journal of Membrane Science* **2014,** *469*, 127–139.

Chapter 5: Complete Coverage Model (CCM)

5.1 MOTIVATION

In the previous chapter, we re-derived the Hermia model to describe fouling under constant flux, crossflow ultrafiltration.[1] A combined model that incorporated intermediate pore blocking (IPB) and cake filtration was developed. The model qualitatively described fouling progression, but we found that the IPB model fails at high foulant concentrations or high permeate fluxes. To resolve this issue, the IPB model is replaced here with a new complete coverage model (CCM). Furthermore, the influence of variable local flux during membrane fouling, which is not discussed in the chapter 4, will be discussed in this study. The new combined model between CCM and cake filtration better describes how operational parameters (*e.g.*, permeate flux, crossflow velocity, and foulant concentration) affect fouling progression than did the previous model.

5.2 THEORETICAL BACKGROUND

5.2.1 IPB model behavior at high concentration/permeate flux

As mentioned in the previous chapter, the IPB model predicts a steady transmembrane pressure (ΔP, TMP) at long filtration time:

$$\Delta P_t = \frac{\Delta P_0}{\left(\frac{1}{K_i} + \left(1 - \frac{1}{K_i}\right)\exp(-K_i B t)\right)} = K_i \Delta P_0 \ (t \to \infty) \qquad \textbf{5.1}$$

$$K_i = 1 + \frac{\sigma J}{B} \qquad \textbf{5.2}$$

$$\sigma = 1.5\frac{\gamma s}{\gamma_0 d\psi} \qquad \textbf{5.3}$$

When permeate flux is far below the threshold flux (TF), and cake filtration is negligible, Equation 5.1 shows that K_i represents the ratio between the steady TMP and the initial

TMP. K_i increases linearly with concentration and permeate flux according to Equations 5.2 and 5.3. Therefore, the normalized TMP, $\Delta P_t/\Delta P_0$, should also increase linearly with these two parameters if B is only a function of crossflow rate. However, predictions based on the IPB model deviate from experimental data at high foulant concentration/permeate flux. Fig. 5.1 presents the normalized TMP profile using the data from Fig. 4.3(a). At low permeate flux (Fig. 5.1(a)), the normalized TMP data sets overlap one other. There is no clear increasing trend in the long-time, steady, normalized TMP (*i.e.*, $\Delta P_t/\Delta P_0$ as $t \rightarrow \infty$). At permeate fluxes near the TF **(**Fig. 5.1(b)), both cake filtration and IPB are active according to the results in Chapter 4. IPB dominates at the beginning of the filtration, when the cake filtration term in Equation 4.25 is still small. In this case, K_i can be defined as the normalized TMP where the fouling mechanism transitions from IPB to cake filtration (the "kink" in Fig. 5.1(b)). All normalized TMP curves in Fig. 5.1(b) increase rapidly to around 1.1 and then transition to linear increases, indicating that the transition from IPB to cake filtration starts at roughly the same normalized TMP regardless of permeate flux. This result does not agree with the prediction of Equation 5.1-5.3. Fig. 5.1(c) summarizes the fitted K_i values below the TF. All fitted K_i values are in a narrow range of 1.08 to 1.14, and there is no clear linear increasing trend. These fitted values also disagree with those estimated from Equation 5.1-5.3, which has prompted the modification of the model considered in this study.

A similar challenge was found while investigating the influence of foulant concentration on the evolution of TMP. Fig. 5.2(a) compares constant flux fouling experiments and model fits at 1 and 10 ppm foulant concentrations, 40 LMH permeate flux, and 0.8 L/min crossflow rate. The red lines represent model fits to the following combined model equation:

$$\Delta P_t = \frac{\Delta P_0 (1 + K_c J t)}{\left(\frac{1}{K_i} + \left(1 - \frac{1}{K_i} \right) \exp(-K_i B t) \right)} \qquad \textbf{5.4}$$

The detailed fitting methods are recorded in the Chapter 4.[1] The normalized TMP curve at 1 ppm increases slowly over time and has an average normalized TMP value of 1.05 at long filtration time. In contrast, $\Delta P_t/\Delta P_0$ for the 10 ppm experiment initially increases sharply to around 1.1, followed by a slow rise. The fitted K_i values at 1 and 10 ppm are 1.036 and 1.125, respectively. These fitted values agree with the IPB model prediction, where the theoretical TMP ratios increase with concentration. Fig. 5.2(b) presents the normalized TMP data and model fits at 10 and 25 ppm with the same permeate flux and crossflow rate. Both data and model curves overlap, and the fitted K_i values are roughly the same (1.125 and 1.126 for 10 and 25 ppm, respectively). Fitted K_i values with a wider range of foulant concentrations are presented in Fig. 5.2(c). For a dilute foulant solution (< 25 ppm), an increase in foulant concentration leads to an increase in the fitted K_i value. However, K_i plateaus around 1.12 if the concentration is higher than about 25 ppm. These results disagree with the K_i equation (*i.e.*, Equation 5.2), which predicts that increases in concentration should lead to increases in steady normalized TMP. Based on Fig. 5.1 and 5.2, the IPB model fails at high concentration and permeate flux. The differences between the experimental data and model predictions are believed to result from IPB model assumptions, which therefore need to be revised. In the IPB model, the membrane pores of projected surface area obstructed by particles are assumed fully blocked and impermeable to water, which yields unreasonably high TMP values when the membrane surface is mostly covered by particles. To address this issue, this assumption is modified in the complete coverage model. More details will be discussed later.

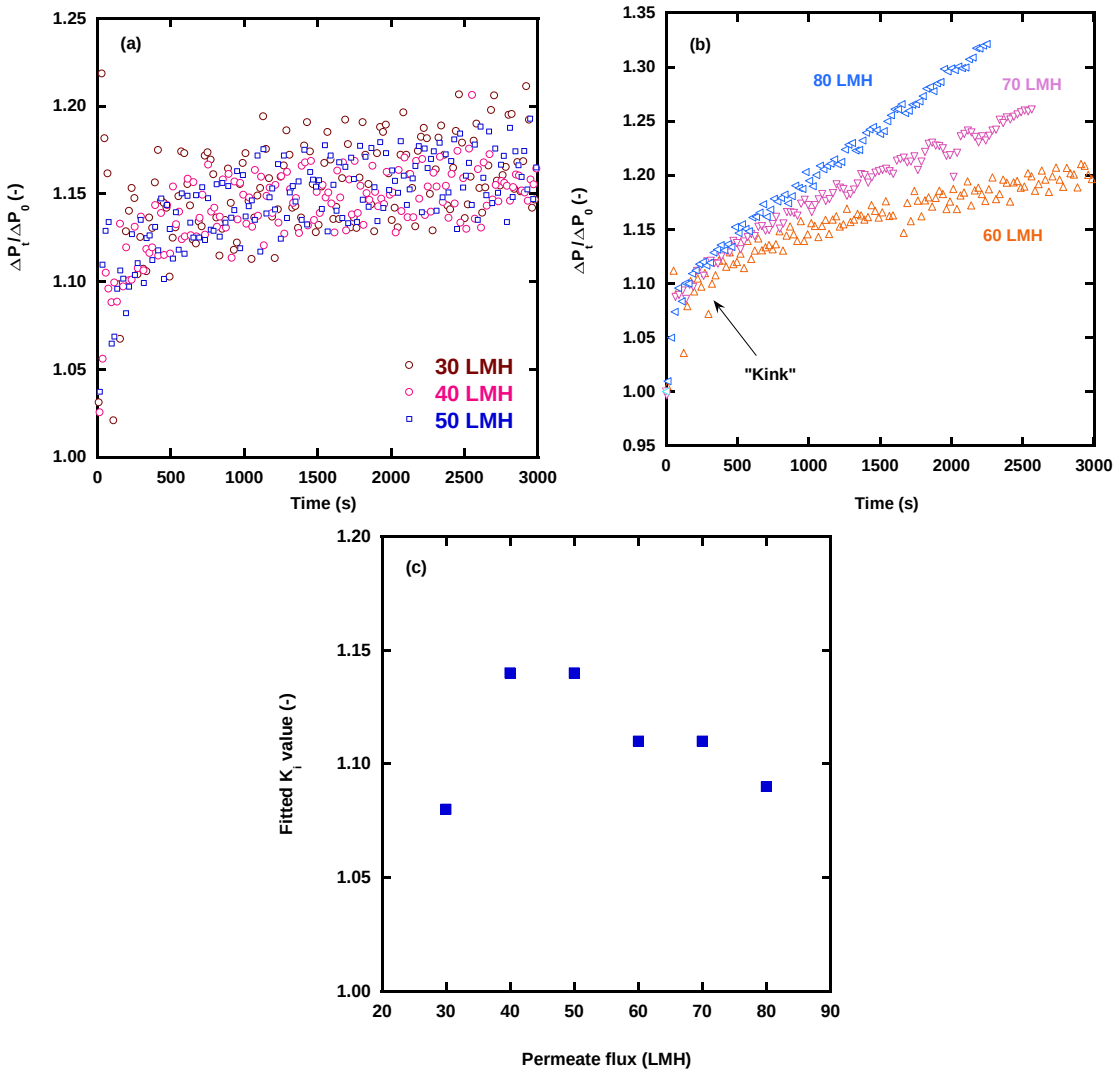

Fig. 5.1: Normalized ΔP profile of constant flux fouling experiments at (a) 30 to 50 LMH, (b) 60 to 80 LMH. (c) Fitted Ki values at various permeate fluxes. Other operational conditions: 0.8 L/min crossflow rate and 200 ppm latex bead concentration.

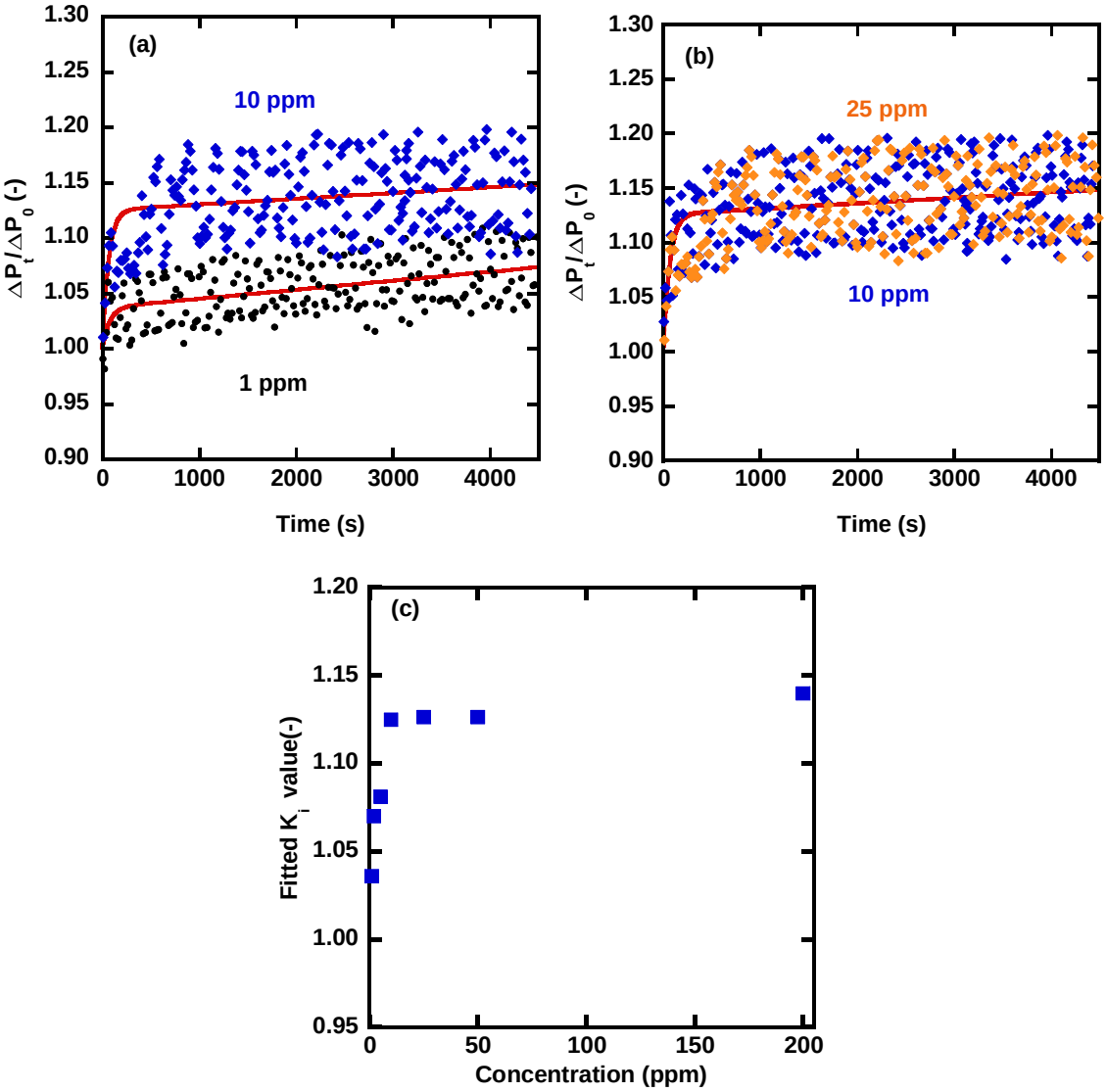

Fig. 5.2: Normalized *ΔP* profile of constant flux fouling experiments at (a) 1 and 10 ppm, (b) 10 and 25 ppm latex bead concentration. Red curves are the fitting results using the combined model from Chapter 4.[1] (c) Fitted Ki values as a function of latex bead concentrations. Other operational conditions: 0.8 L/min crossflow rate and 40 LMH permeate flux.

5.2.2 The influence of changing local flux on TMP evolution with filtration time

In Chapter 4, the probability for a particle to deposit onto an unobstructed area of membrane, rather than on previously deposited particles, was proportional to the instantaneous unobstructed membrane surface area. The foulant removal rate was proportional to the obstructed surface area. As a result, the rate of change for the obstructed membrane surface area, assuming there is no adsorption, was expressed as follows:[1]

$$\frac{da_p}{dt} = \sigma J(a_0 - a_p) - Ba_p \qquad \textbf{5.5}$$

where a_0 and a_p are the surface area of the unobstructed (*i.e.*, pristine) membrane at time 0 and the membrane surface area obstructed by particles at any time [m^2], respectively. Previously, Equation 5.5 was solved by setting that the permeate flux (J) equals to the constant overall (*i.e.*, global) permeate flux (*i.e.*, the volumetric flowrate through the membrane divided by the total membrane surface area). In constant flux crossflow filtration, the overall permeate flux is constant. However, the local permeate flux through unobstructed sections of the membrane must increase during fouling to maintain a constant overall flux through the membrane. Fig. 5.3 depicts this change in local permeate flux as the membrane fouls. Therefore, J in Equation 5.5 should be the average local flux through the unobstructed surface of the membrane, which is a function of the remaining unobstructed surface area, rather than the overall flux, which is a constant. Based on other studies, changes in local permeate flux play an important role in fouling evolution.[2-3] In the model development section of this chapter, complete coverage model with and without variable local flux will be derived, and they will be compared later.

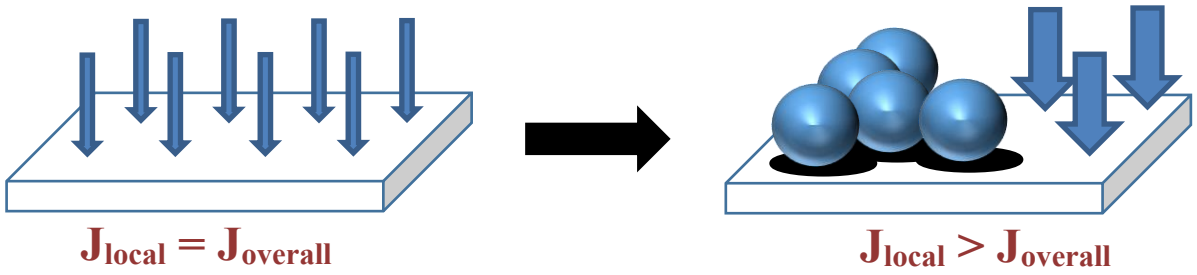

Fig. 5.3: Illustration of the changes in local permeate flux as fouling progresses. The vertical arrows represent local flux values at various locations of the membrane, with larger arrows indicating higher local flux values after the membrane is partially fouled by particles.

5.3 Model Development

5.3.1 IPB vs. CCM - assumption comparison

Fig. 5.4 highlights differences between the IPB and CCM model assumptions. In the IPB model, the projected surface area obstructed by particles is assumed to be fully blocked and therefore, impermeable to water. As a result, the unblocked surface area of the membrane decreases, and ΔP increases during fouling. This assumption may fail when the foulant concentration or permeate flux is high. An SEM image of a membrane fouled by a high concentration solution of latex beads (200 ppm) is shown in Fig. 5.5. Latex beads cover a large portion of the membrane surface. Based on the IPB model, ΔP should approach infinity as membrane pore area goes to zero, to maintain a constant overall flux. However, this prediction disagrees with the experimental data in Fig. 5.1(a). This issue is addressed in the new complete coverage model by assuming that the obstructed area (*i.e.*, projected surface area covered by foulant particles) is still permeable, but its resistance to flow is higher than the initial membrane resistance by a factor of f (*i.e.*, an obstruction does not completely block permeate flow through the pores, but it does causes a hindrance to permeate flow). This hindrance factor, f, is assumed to be an intrinsic function of

membrane/foulant properties and not affected by operational conditions (*e.g.*, foulant concentration, permeate flux, etc.). Based on Darcy's Law (*i.e.*, Equation 4.1), ΔP should increase to maintain a constant overall flux when membrane resistance increases due to membrane fouling. At complete coverage, ΔP equals $f\Delta P_0$, rather than infinity as predicted by the IPB model.

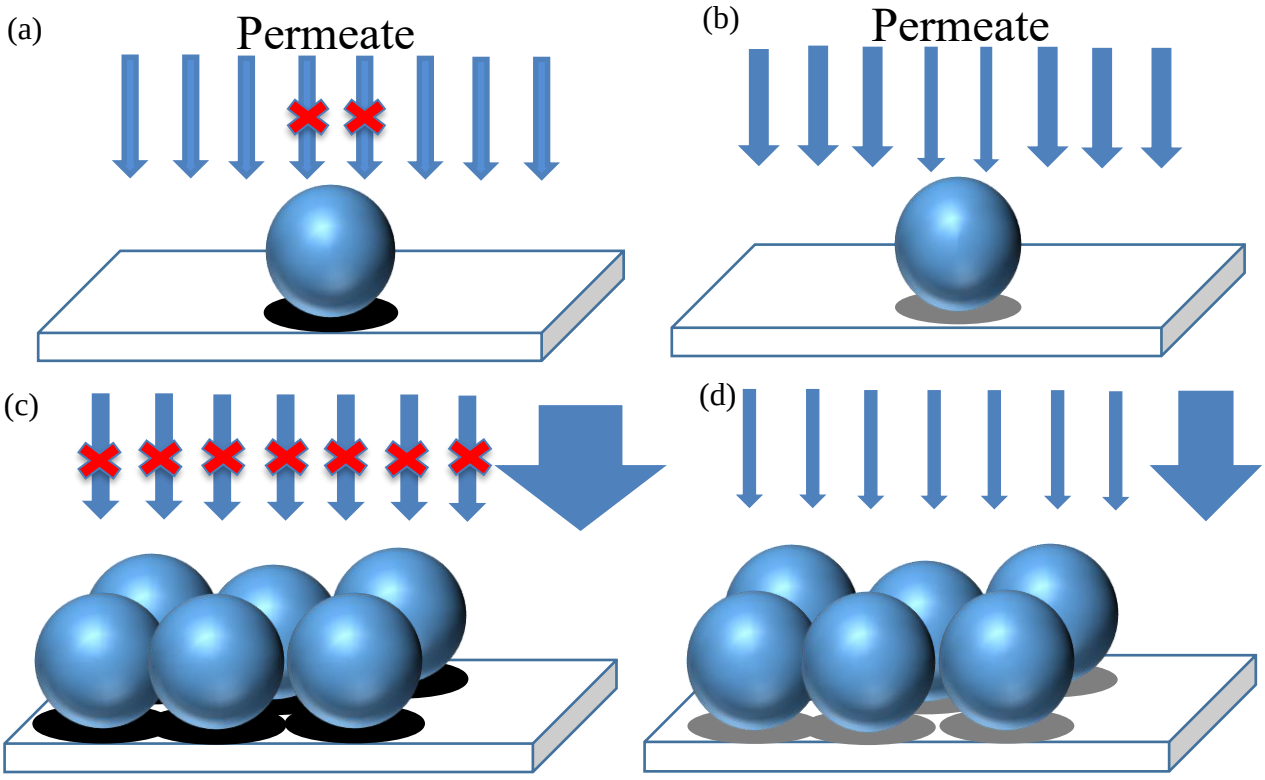

Fig. 5.4: IPB and CCM model assumptions: (a) IPB model with a single particle, (b) CCM with a single particle, (c) IPB model with high surface coverage of foulant particles, and (d) CCM with high surface coverage of foulant particles. The vertical arrows represent local flux values with larger arrows representing higher local flux values.

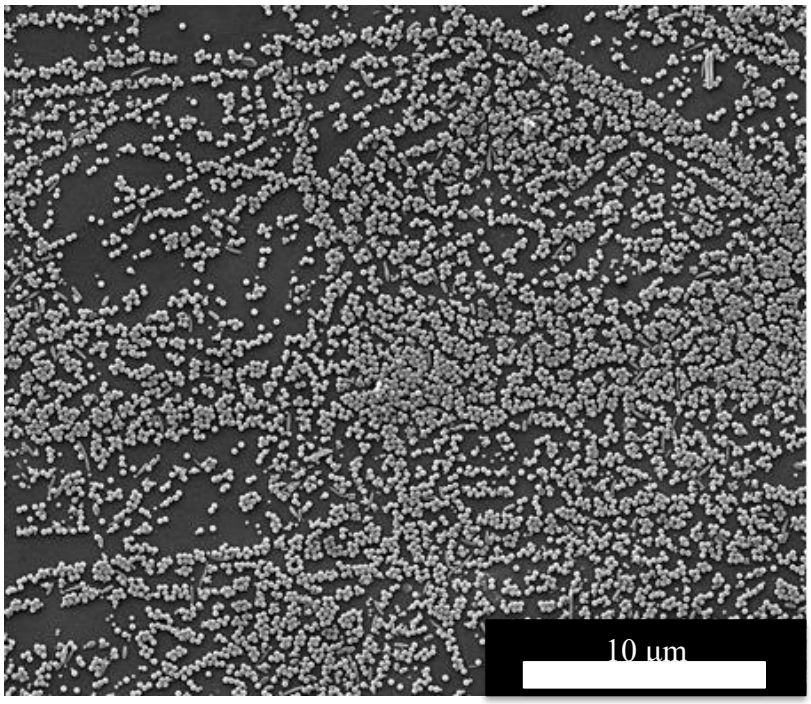

Fig. 5.5: SEM image of the top surface of a membrane fouled with high concentration. Fouling conditions: 200 ppm latex bead suspension, 40 LMH permeate flux, and 0.8 L/min crossflow rate.

5.3.2 Complete coverage model derivation

As mentioned in Section 5.2.2, the rate of change in the obstructed membrane surface area is expressed by Equation 5.5, assuming no foulant adsorption. However, foulant adsorption/desorption could play an important role in membrane fouling, as pointed out by Howe and Clark.[4] Consequently, adsorption and desorption terms are incorporated into Equation 5.5 using first order kinetics. That is, the foulant adsorption rate is proportional to the foulant concentration and unobstructed surface area, and the desorption rate is proportional to the obstructed surface area:

$$\frac{da_p}{dt} = \sigma(a_0 - a_p)J - Ba_p + k_a c(a_0 - a_p) - k_d a_p \qquad \textbf{5.6}$$

where k_a and k_d are the adsorption [$ppm^{-1}s^{-1}$] and desorption [s^{-1}] rate constants, respectively, and c is the foulant concentration in the bulk feed solution [ppm]. Equation 5.6 assumes J is constant, so changes in local permeate flux are not considered. The impact of changing local flux will be discussed later. Integrating Equation 5.6 yields the expression for the obstructed membrane surface area as a function of time:

$$a_p(t) = a_0 \frac{\sigma J + k_a c}{\lambda}(1 - e^{-\lambda t}) \qquad \textbf{5.7}$$

where the exponential decay constant, λ, is defined as:

$$\lambda = \sigma J + k_a c + B + k_d \qquad \textbf{5.8}$$

For the CCM model, the sum of permeate flows from the obstructed area and the clean membrane area at any time should equal to the initial volumetric flow rate, since the membrane is operated at constant flux. If deposited particles increase the resistance to flow by a factor of f, the flowrate through the unobstructed and obstructed area can be expressed by Darcy's Law:

$$\frac{\Delta P_t(a_0 - a_p)}{\mu R_0} + \frac{\Delta P_t a_p}{\mu f R_0} = \frac{\Delta P_0 a_0}{\mu R_0} \qquad \textbf{5.9}$$

Rearranging Equation 5.9 yields the relationship between ΔP and obstructed membrane surface area:

$$\frac{\Delta P_t}{\Delta P_0} = \frac{a_0}{a_0 - a_p(1 - 1/f)} \qquad \textbf{5.10}$$

Substitution of Equation 5.7 into Equation 5.10 yields

$$\Delta P_t = \frac{\Delta P_0}{1 - K_{CCM}\left(1 - e^{-\lambda t}\right)} \qquad \textbf{5.11}$$

where K_{CCM} is the model constant defined as follows:

$$K_{CCM} = \frac{\sigma J + k_a c}{\lambda}(1 - 1/f) \qquad \textbf{5.12}$$

Table 5.1 compares predicted trends in normalized ΔP from the IPB and CCM models. In Equation 5.2, K_i is taken to be a linear function of concentration and permeate flux. Consequently, the IPB model predicts a linear change in the normalized ΔP with these two parameters at long filtration time. Equation 5.2 also predicts a decrease in K_i with increasing crossflow rate. In contrast, the normalized ΔP prediction by the CCM varies with foulant concentration. At high concentration, the particle deposition terms (*i.e.*, σJ and $k_a c$) dominate the particle removal terms (*i.e.*, B and k_d), so $(\sigma J + k_a c)/\lambda$ of K_{CCM} in Equation 5.12 always approaches one. Changes in the permeate flux or crossflow rate have little effect on the K_{CCM} values, which approach the theoretical maximum (1-1/f) in this case. At low foulant concentrations, where particle deposition terms are not much larger than removal terms, increases in crossflow rate should decrease the K_{CCM} value. Increases in permeate flux or concentration should increase K_{CCM}, but the rate of increase slows and eventually nears zero when the concentration or permeate flux is high enough to make foulant removal terms negligible. Therefore, an increasing permeate flux at low concentration leads to an increase-then-plateau behavior in K_{CCM}.

As mentioned above, analytical solutions of Equations 5.11 and 12 neglect the influence of changing local flux mentioned in Section 5.2.2. To evaluate how changes in the local permeate flux affects particle deposition, we must determine the relationship

between the flux through the unobstructed area (J_{uo}) and a_p, projected surface area. Based on Darcy's Law:

$$J_{uo} = \frac{\Delta P_t}{\mu R_0} \qquad \textbf{5.13}$$

The influence of a_p on J_{uo} can be found by combining Equation 5.13 with Equation 5.9:

$$J_{uo} = \frac{a_0 J_0}{a_0 - a_p(1-1/f)} \qquad \textbf{5.14}$$

The J in Equation 5.6 should be replaced with J_{uo} when we consider the effect of changing local flux:

$$\frac{da_p}{dt} = \sigma(a_0 - a_p)J_{uo} - Ba_p + k_a c(a_0 - a_p) - k_d a_p \qquad \textbf{5.15}$$

However, because Equation 5.15 is a nonlinear differential equation, the solution is lengthy and cannot be used with Darcy's Law to obtain a simple analytical form for ΔP_t as a function of time. The alternative is solving Equation 5.15 numerically, and then applying the solution to Darcy's Law. In the following discussion of this chapter, both the analytical solution of constant local flux (Equations 5.11 and 12) and the numerical solution of changing local flux will be used for experimental data fitting. More fitting details are presented in Appendix A1.

Table 5.1: Prediction of steady normalized TMP $\Delta P_t/\Delta P_0$

	IPB model $\Delta P_t = \frac{\Delta P_0}{\left(\frac{1}{K_i} + \left(1 - \frac{1}{K_i}\right)\exp(-K_i B t)\right)}$ $K_i = 1 + \frac{\sigma J}{B}$	CCM model $\Delta P_t = \frac{\Delta P_0}{1 - K_{CCM}\left(1 - e^{-\lambda t}\right)}$ $K_{CCM} = \frac{\sigma J + k_a c}{\sigma J + B + k_a c + k_d} \times (1 - 1/f)$
Steady normalized TMP	$\frac{\Delta P_t}{\Delta P_0} = K_i$	$\frac{\Delta P_t}{\Delta P_0} = \frac{1}{1 - K_{CCM}}$
Increasing permeate flux (high foulant concentration)	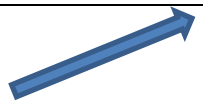	
Increasing permeate flux (low foulant concentration)	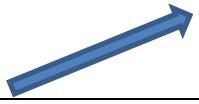	
Increasing crossflow rate (high foulant concentration)	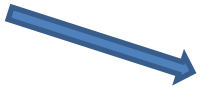	
Increasing crossflow rate (low foulant concentration)	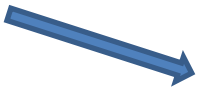	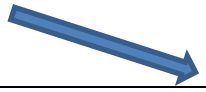
Increasing foulant concentration	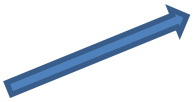	

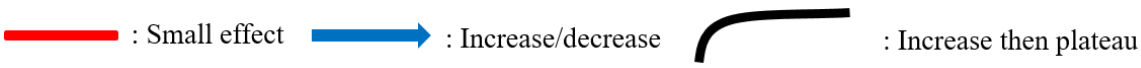

5.4 RESULTS AND DISCUSSION

5.4.1 CCM fitting

To compare the CCM and IPB, the experimental and fitting methods for CCM are similar to those for IPB in Chapter 4. Because the CCM and IPB focus on external fouling, the particle size of the latex beads (0.22 μm) is selected to be much larger than the average membrane pore size (3 nm), so the rejection of latex beads is 100%. For model fitting, the CCM alone can fit the data far below the TF, which is similar to results from the IPB model in Chapter 4. However, the CCM must be combined with the cake filtration model to fit data near and above the TF because the cake filtration mechanism begins to influence the ΔP in these flux regimes. The model combining CCM and cake filtration is shown as follows:

$$\Delta P_t = \frac{\Delta P_0 (1 + K_C J t)}{1 - K_{CCM}\left(1 - e^{-\lambda t}\right)} \qquad \textbf{5.16}$$

where J is the overall (*i.e.*, global) flux, which is set to a constant value in the experiment. The CCM and cake filtration models are combined as described in in Chapter 4.[1] Three parameter fittings were done using Matlab 2019b to roughly estimate K_{CCM}, K_c and λ. As mentioned above, the CCM is expected to describe fouling at short filtration times, before cake filtration becomes significant. The transition time, t^*, marks the transition between these two mechanisms and is arbitrarily defined as the time when the exponential term of Equation 5.16 equals 0.01. t^* is calculated using the fitted λ value. Based on the new combined model, ΔP_t should rise linearly with time later in the experiment when cake filtration is dominant, and slope is equal to $\Delta P_0 K_c J/(1-K_{CCM})$ slope. K_c can be related to K_{CCM} as follows:

$$K_C = \frac{slope(1-K_{CCM})}{\Delta P_0 J} \qquad \textbf{5.17}$$

where "*slope*" is the slope of the ΔP vs. time plot in the linear cake filtration region. Next, λ is treated as the only adjustable parameter for one parameter fit because other parameters can be measured. The hindrance factor, *f*, is measured by fouling the membrane with concentrated latex bead suspensions (*cf.* Appendix A.2.1). The adsorption and desorption rate constants were measured using the adsorption test (*cf.* Appendix A.2.2). Estimations of projected surface area per unit filtrate volume (σ) and the shape factor (ψ in Equation 5.3) are described in Appendix A.2.3. The estimated shape factor value , ψ, was 0.12, which is much smaller than the theoretical value of 1 for perfect spheres. This difference is ascribed to the uneven particle deposition during membrane fouling (*cf.* Appendix A.2.3). K_{CCM} and K_c are calculated using Equations 5.12 and 17. Details of fitting methods and parameter estimation strategies are presented in the Appendix A.1.

The results of one parameter fitting using the data as Fig. 4.3 are shown in Fig. 5.6. In this case, the TF is around 80 LMH at 200 ppm foulant concentration and 0.8 L/min crossflow rate. The combined CCM and cake filtration model fits the data well. In the next section, the influence of operational conditions (*i.e.*, foulant concentration, permeate flux,

and crossflow rate) on fitted K_{CCM} values are investigated and compared to the CCM model predictions from Table 5.1.

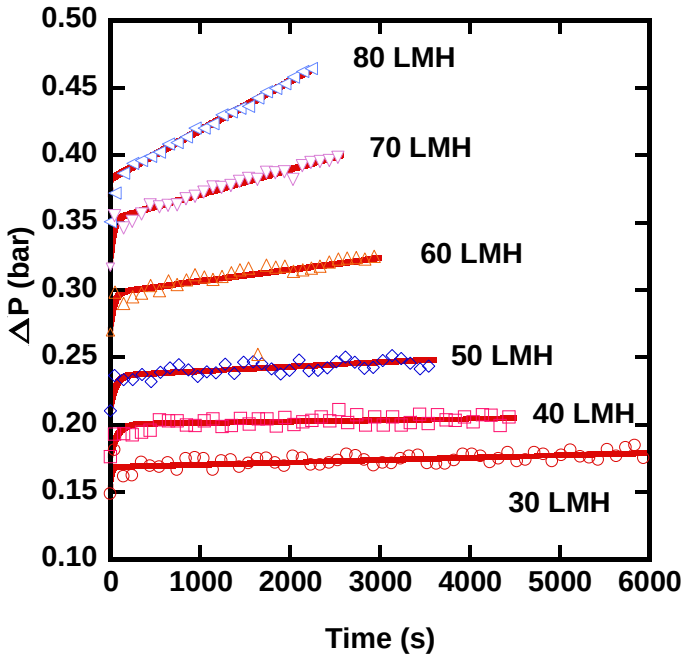

Fig. 5.6: Influence of permeate flux on TMP. The open symbols are experimental data, and the solid curves are fits to the combined CCM/cake filtration model (Equation 5.16). Other experimental conditions: 200 ppm latex bead suspension, 0.8 L/min crossflow rate.

5.4.2 Influences of operating conditions on K_{CCM} values

5.4.2.1 Foulant concentration

Representative normalized TMP profiles as a function of foulant concentration are presented in Fig. 5.2. As discussed above, an increase in foulant concentration leads to an increase in steady normalized TMP for dilute suspensions. However, at high foulant concentrations, changing foulant concentration barely affects the steady normalized TMP. A series of constant flux crossflow fouling experiments were conducted at various foulant

concentrations (1-200 ppm) and three permeate fluxes (40, 50 and 60 LMH). Fitted K_{CCM} values for these experiments are presented in Fig. 5.7. The increase in foulant concentration contributes to sharply increasing fitted K_{CCM} values at low concentration for all three permeate fluxes. However, the influence of increasing concentration on K_{CCM} diminish above 25 ppm, where the rate of increase in K_{CCM} decreases significantly. These trends agree qualitatively with the CCM prediction in Table 5.1. Furthermore, the fitted K_{CCM} values at the highest concentration (200 ppm) are around 0.11 for all three permeate fluxes. Based on Equations 5.12, the K_{CCM} should come close to its theoretical maximum of (1-1/*f*) at high concentration or high permeate flux. The theoretical maximum is 0.12 for our foulant/membrane pair (*f* equals 1.137, and this measurement is presented in Appendix A.2.1). These fitted K_{CCM} values approach the maximum value, which agrees with model expectations.

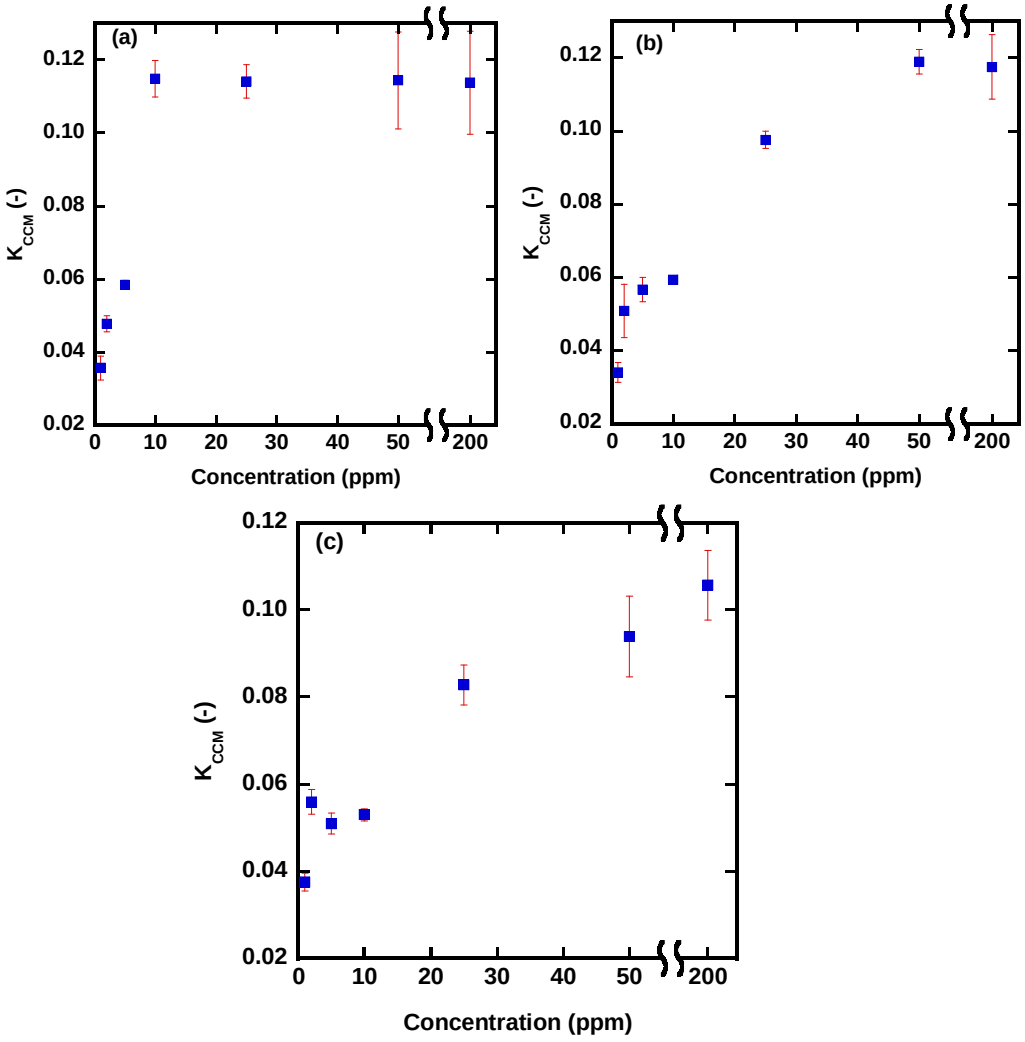

Fig. 5.7: Fitted K_{CCM} values at various latex bead concentrations at: (a) 40 LMH, (b) 50 LMH, and (c) 60 LMH permeate flux. The crossflow rate is 0.8 L/min.

5.4.2.2 Permeate flux

As discussed in section 5.3, in the CCM, the influence of changing permeate flux on K_{CCM} will vary with foulant concentration. Increasing permeate flux should have little effect on K_{CCM} at high concentration and should lead to an 'increase-then-plateau' behavior at low concentration. Based on the results presented in Fig. 5.7, 200 ppm was chosen as a

representative high concentration because the fitted K_{CCM} values are close to the theoretical maximum for all three fluxes considered, and 5 ppm data is used to represent low concentration.

Fig. 5.1 presents normalized TMP curves at various permeate fluxes at high foulant concentration. All normalized TMP curves far below TF (Fig. 5.1(a)) increase rapidly to around 1.12 at the beginning of fouling followed by gradual increases in TMP. The "kinks" in normalized TMP of Fig. 5.1(b) (*i.e.*, near the TF) also occur around 1.1. The fitted K_{CCM} values at high concentrations and various permeate fluxes are presented in Fig. 5.8 and are all in the range of 0.1 to 0.12, which is close to the theoretical maximum of 0.12. There is no clear increasing or decreasing trend with permeate flux. These results agree with the qualitative predictions in Table 5.1.

Representative normalized TMP profiles at low concentration and their fitted K_{CCM} values are shown in Fig. 5.9. The normalized TMP increases as permeate flux increases from 30 to 60 LMH. The normalized TMP for 80 LMH has a sharp initial increase, and then increases linearly with time, because 80 LMH is close to the TF, which is 100 LMH for this experimental condition. At this condition, the dominant fouling mechanism changes from CCM to cake filtration at a normalized transmembrane pressure value of ~1.09 (*i.e.*, the location of the sharp change in gradient in the normalized TMP curve, which is referred to as a "kinks" in the data), which is higher than the steady normalized TMP at 30 and 60 LMH. Fig. 5.9(b) summarizes the fitted K_{CCM} values with changing permeate fluxes at a latex bead concentration of 5 ppm. The K_{CCM} values increase with increasing permeate flux in the range of 30 to 70 LMH, but the rate of increase slows above 70 LMH. This trend agrees with the expectation set forth Table 5.1. The maximum K_{CCM} value in Fig. 5.9(b) is 0.076 at 80 LMH, which is still lower than any of the K_{CCM} values when

foulant concentration is high (*cf.* Fig. 5.8). This result is reasonable because the concentration in Fig. 5.9 (5 ppm) is 40 times more dilute than the high concentration case (200 ppm). The particle deposition terms of K_{CCM} (*i.e.*, σJ and $k_a c$) at high concentration are much higher than their values at low concentration, even at high permeate flux. As a result, the K_{CCM} values at high concentration are close to the theoretical maximum and higher than those at low concentration.

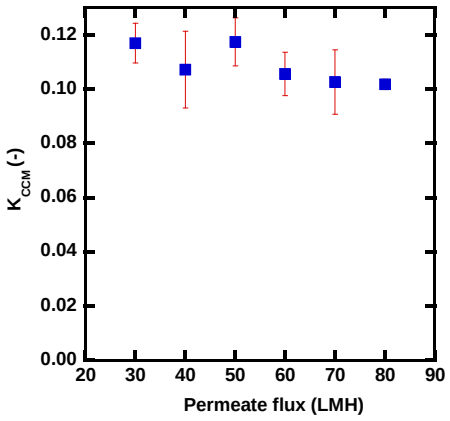

Fig. 5.8: Influence of permeate flux on K_{CCM} at 200 ppm foulant concentration. The crossflow rate is 0.8 L/min.

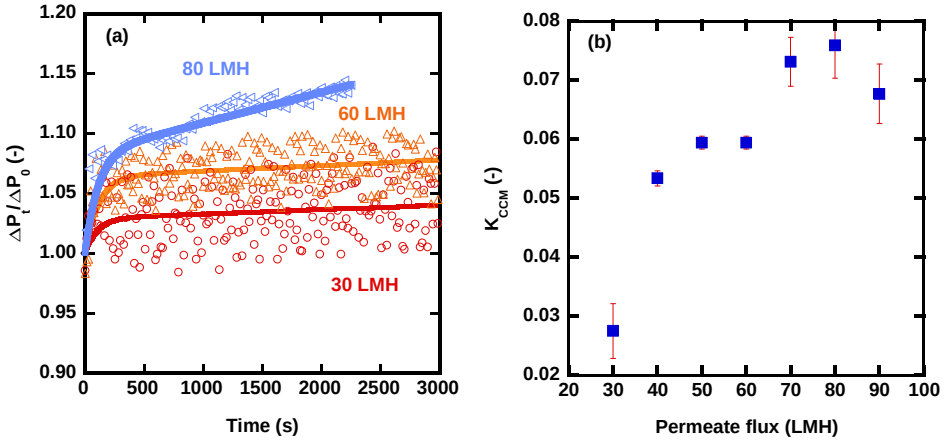

Fig. 5.9: (a) Representative normalized pressure profiles (open data point symbols) and fits of the model (solid curves). (b) Influence of permeate flux on K_{CCM} values at 5 ppm foulant concentration. The cross flowrate is 0.8 L/min.

5.4.2.3 *Crossflow rate*

As mentioned in the previous section, the influence of crossflow rate on steady, normalized TMP at high or low concentration will be discussed separately. Fig. 5.10 presents representative normalized TMP curves and fitted K_{CCM} values at high concentration (200 ppm), various crossflow rates (0.6 – 1.2 L/min), and permeate fluxes (30 – 80 LMH). As shown in Fig. 5.10(a), all three TMP profiles overlap, so changes in crossflow rate have little influence on the steady normalized TMP at high concentration. There is no clear trend to increase or decrease with changing permeate flux or crossflow rate. Similar to the results presented in Fig. 5.8, most fitted K_{CCM} values (*cf.* Fig. 5.10(b)-(d)) are also around 0.1, which is close to the theoretical maximum. All these fitting results agree with the expectations in Table 5.1.

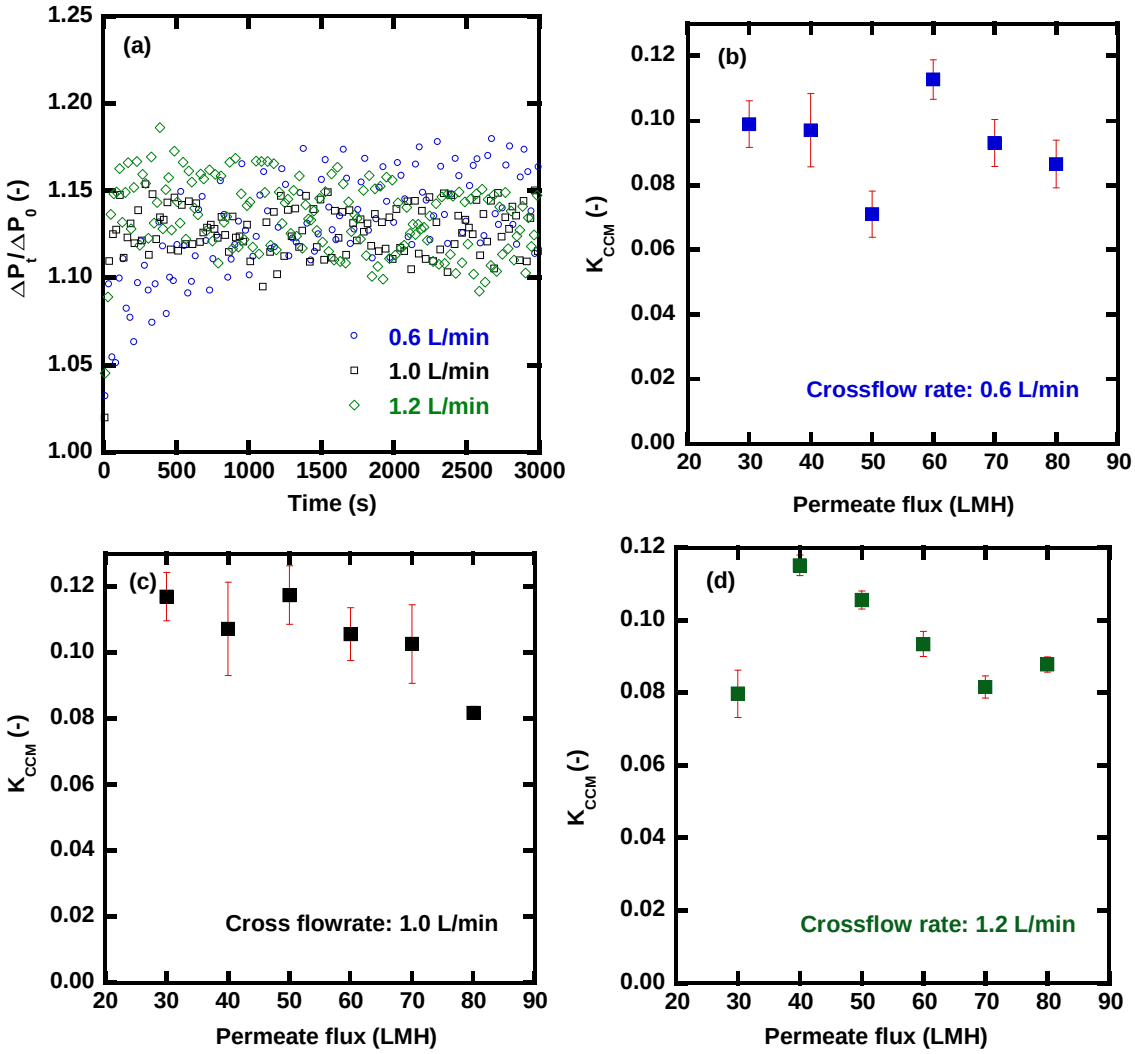

Fig. 5.10: (a) Representative normalized TMP profiles at 40 LMH, and (b-d) fitted KCCM values at various permeate fluxes, crossflow rates, and 200 ppm foulant concentration. Crossflow rates of 0.6, 1.0, and 1.2 L/min correspond to Reynolds numbers of 800, 1400, and 1700, respectively, based on the Reynolds number calculation method in the literature.[5]

Fig. 5.11(a) presents representative experimental normalized TMP data and model results at various crossflow rates, 5 ppm foulant concentration, and 40 LMH permeate flux. Although the steady normalized TMP decreases from around 1.1 to 1.05 as crossflow rate increases from 0.6 to 1.2 L/min, any further increase in crossflow rate has little influence

on the steady (*i.e.*, long-time) pressure. Fig. 5.11(b) summarizes the fitted K_{CCM} values at various crossflow rates. K_{CCM} decreases from 0.075 to around 0.05 with increasing crossflow rate, but most values are close to 0.05 and within the margin of error. The reason for the weak influence of crossflow rate on steady TMP may be due to the low fouling rate at this concentration. At low fouling rates, few particles deposit on the membrane surface even at low crossflow rates, so increases in crossflow rate have a limited effect on foulant removal. To further investigate how crossflow rate affects the K_{CCM} values, fouling experiments were run at 25 ppm at the same permeate flux (*i.e.*, 40 LMH). A concentration of 25 ppm was chosen because this is near the upper limit for the low concentration regime based on Fig. 5.7. The results are presented in Fig. 5.12. Compared to Fig. 5.11(a), the increase in crossflow rate leads to a small decrease in steady normalized TMP. The K_{CCM} values also decreased, from 0.11 to 0.05 as crossflow rate increased from 0.6 to 2.0 L/min (Fig. 5.12(b)).

In conclusion, the influence of crossflow rate on TMP at high and low concentrations is minimal. The high particle deposition rate at 200 ppm overwhelms particle removal rate, so the surface is mostly covered with foulant particles regardless of the crossflow rate. At low concentrations (*e.g.*, 5 ppm), the surface is mostly clean even at low crossflow rates, so increasing the crossflow rate has a minimal influence on the normalized steady TMPs. The effects of crossflow rate on TMP will be stronger at concentrations between these extremes.

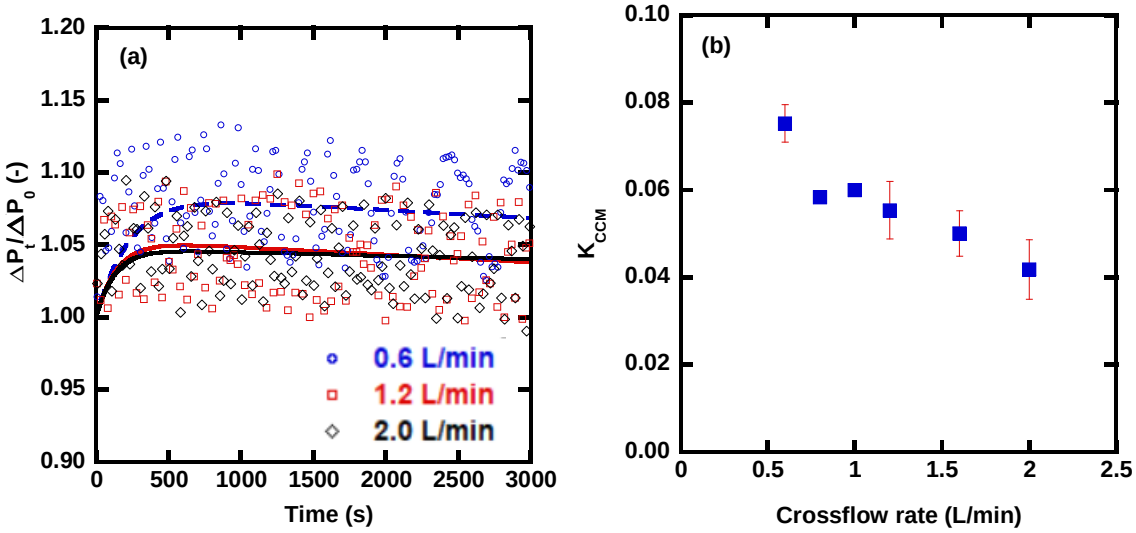

Fig. 5.11: (a) Representative experimental normalized TMP profiles and model fits (solid curves), and (b) K_{CCM} values as a function of crossflow rate. The foulant concentration is 5 ppm, and the permeate flux is 40 LMH.

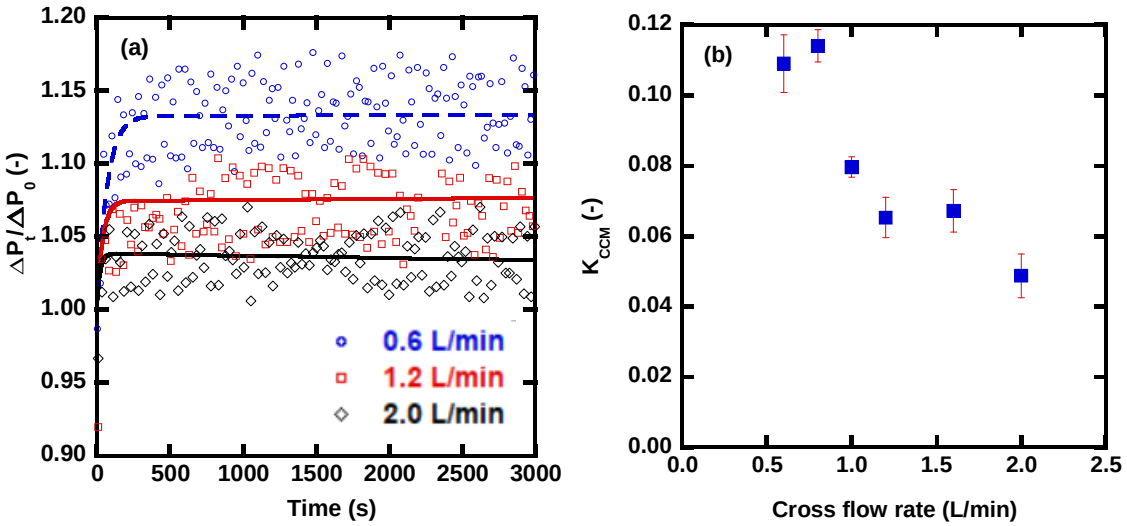

Fig. 5.12: (a) Representative experimental normalized TMP profiles and model fits (solid curves), and (b) fitted K_{CCM} values with various crossflow rate. The foulant concentration is 25 ppm and the permeate flux is 40 LMH.

5.4.3 Influence of changing local flux

In our previous discussion, Equations 5.11 and 5.12 were used for fitting. These analytical solutions assume that the local permeate flux: (1) does not change during membrane fouling and (2) is equal to the initial overall (*i.e.*, global) flux. However, the local permeate flux through a clean, unobstructed pore will be different from that through an fouled, partially obstructed pore due to the increase in resistance to mass transfer due to pore blockage by foulants. Equations 5.14 and 5.15 include this effect by making J_{uo}, the flux through unobstructed area, a function of obstructed pore area. This nonlinear differential equation can be solved numerically, and then applied to Darcy's Law to compute the TMP curve. Fig. 5.13 compares simulations based on Equations 5.11 (*i.e.*, constant local flux) and 5.15 (*i.e.*, variable local flux). All parameters except foulant concentration were measured from other experiments and then applied to the simulations (measurement details can be found in the Appendix A). All simulations computed using Equation 5.15 have higher steady normalized TMP than those from Equations 5.11. This result is reasonable because particle deposition due to permeate flux, σJ_{uo} in Equations 5.14 and 5.15, is higher than that in Equation 5.11 (σJ). In other words, Equation 5.15 predicts that foulant particles deposit on unobstructed surface area preferentially due to increases in local permeate flux. Consequently, the obstructed surface area and transmembrane pressure predicted by Equation 5.15 are slightly higher than those of Equation 5.11. The J_{uo} value is close to J_0 when the membrane surface is mostly clean, so the predicted steady pressure difference is minimal at the lowest foulant concentration (*i.e.*, 5 ppm). The prediction difference is also small at the highest concentration (*i.e.*, 200 ppm), when the membrane surface is almost completely covered by particles. The largest differences between simulations occur between 25 and 50 ppm. Therefore, data for 25 ppm

concentration will be used to investigate the fitting differences between Equation 5.11 and Equation 5.15.

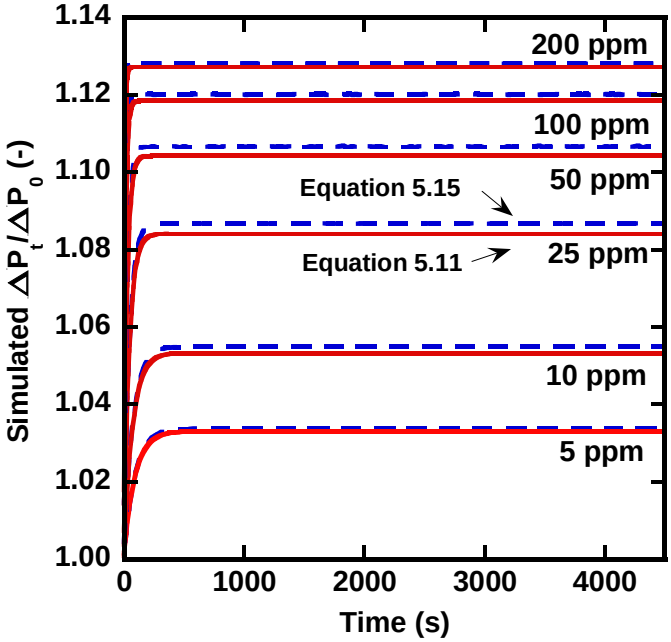

Fig. 5.13: The influence of latex bead (*i.e.*, foulant) concentration on calculated normalized TMP profiles based on models assuming variable local flux (blue dashed curves) and constant local flux (red curves). Other parameter values: f=1.137, k_a=4.594×10^{-7} ppm^{-1}s^{-1}, B=0.0083 s^{-1}, J_0 = 1.11×10^{-5} m/s (corresponding to 40 LMH and 0.8 L/min crossflow rate). Parameter measurement details can be found in Appendix A.2.

The experimental data at 25 ppm, 40 LMH permeate flux, and various crossflow rates (*cf.* Fig. 5.12) was fitted with Equation 5.15 using resuspension rate (B) as the fitting parameter. The representative fitting result is shown in Fig. 5.14(a). The fitting result from Equation 5.15 is similar to that from Equation 5.11, which means it can also describe pressure evolution during fouling. To compare the numerical fitting results with Equation 5.11, the λ values of numerical fits are calculated using the definition in Equation 5.8. The λ value differences between numerical fitting and analytical fitting (Equation 5.11) are shown in Fig. 5.14(b). λ values from numerical fits are higher than those from Equation

5.11 under the same fouling conditions. This is because the resuspension rate (B) in λ must increase to compensate for the increase in local permeate flux. However, the differences are small due to the f factor, which for our membrane/foulant pair is 1.137, close to unity. Based on Equation 5.14, the J_{uo} is only 10% stronger than the initial flux even when the surface is mostly covered, so the effect of changing local flux is small. In this case, the analytical solution assuming constant local flux (Equation 5.11) could be a good approximation for model fitting. To further support this statement, λ values from fittings with Equation 5.15 were applied to Equations 5.11 for simulation. This simulation was then compared to experimental data, and the results are presented in Fig. 5.15. The Equation 5.11 simulation leads to only a small decrease in steady pressure compared to the fitting from Equation 5.15. This error is smaller than the background noise of the pressure measurement. However, this approximation is not applicable if f is large. Fig. 5.16 presents simulations of Equations 5.11 and 5.15 using the same parameters as in Fig. 5.15 except for f. The error between Equation 5.11 and 5.15 grows with increasing f factor, which means that Equation 5.11 loses its validity when foulants have a stronger impact on the membrane resistance (large f value). In conclusion, the analytical solution of the CCM model assuming constant local flux is a good approximation if the f factor is sufficiently small, but Equation 5.15 must be used if the foulant strongly affects the resistance of membranes.

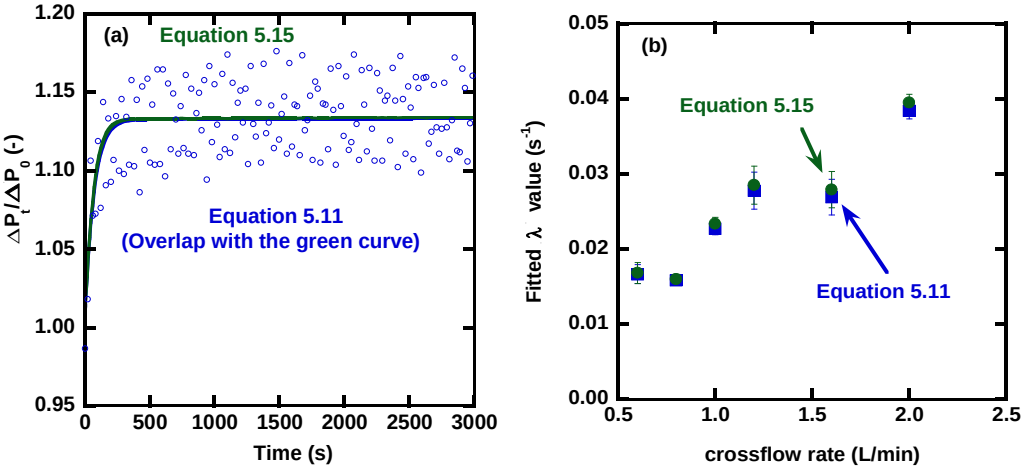

Fig. 5.14: (a) Representative CCM fitting comparison with changing local flux (green curve) and constant local flux (blue curve, which overlaps with the green curve). The exprimental data, shown as unfilled circles, are for the following conditions: 25 ppm foulant concentration, 0.6 L/min crossflow rate, and 40 LMH permeate flux. (b) Influence of crossflow rate on exponential decay constant, λ, using Equation 5.11 (blue filled squares) and 5.15 (green filled squares) Fouling conditions: 25 ppm foulant concentration and 40 LMH permeate flux.

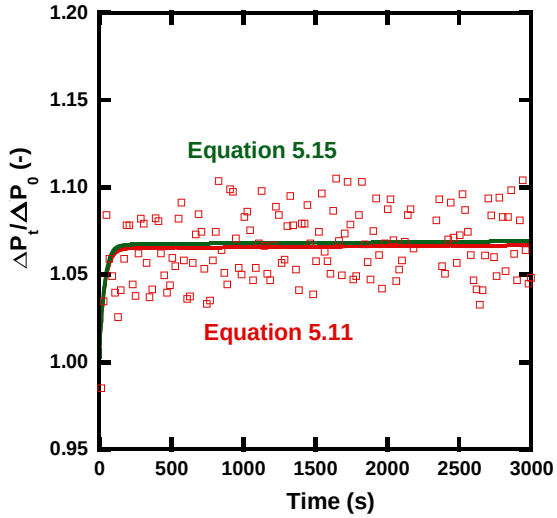

Fig. 5.15: Representative simulation result of Equation 5.11 and its comparison to real data. The experimental data were fit with Equation 5.15 first, then the fitted λ value (0.0303) was used for the simulation. Fouling conditions: 40 LMH permeate flux, 1.2 L/min crossflow rate, and 25 ppm foulant concentration.

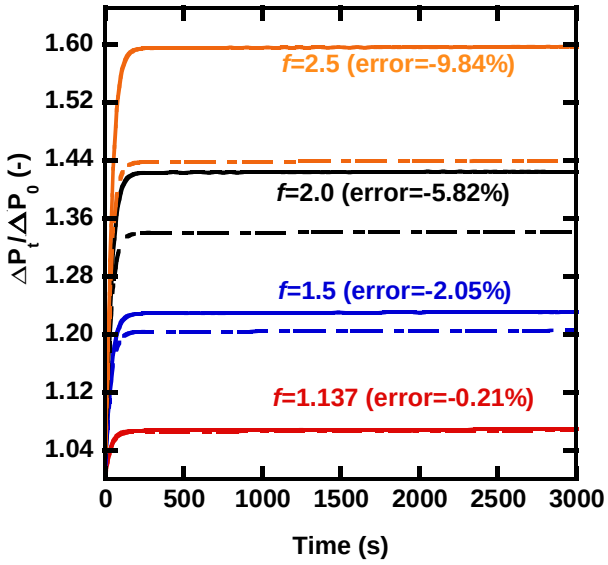

Fig. 5.16: The influence of f (*i.e.*, hindrance factor) on calculated normalized TMP profiles using Equation 5.11 (dash dotted curves) and Equation 5.15 (solid curves) with various f factors. The simulation parameters and λ value (0.0303) are the same as those used in Fig. 5.15. The error values reported here correspond to the the steady normalized TMP calculated using Equation 5.15 and were estimated using the following equation:

$$error\% = \frac{\text{Steady TMP (Equation 5.15)-Steady TMP (Equation 5.11)}}{\text{Steady TMP (Equation 5.15)}} \times 100\% \qquad \textbf{5.18}$$

Table 5.2: List of symbols (Chapter 5)

NOMENCLATURE	
SYMBOL	**DEFINITION & UNITS**
A	Total membrane surface area [m^2]
a	Unobstructed membrane surface area [m^2]
a_0	Unobstructed membrane surface area at time zero [m^2]
a_p	Obstructed (projected) membrane surface area by particles [m^2]
B	Particle resuspension rate [s^{-1}]
c	Particle concentration [ppm]

Table 5.2, continued.

J	Permeate flux [m/s]
J_{uo}	Permeate flux through unobstructed membrane surface area [m/s]
f	Hindrance factor [-]
K	Model Constant depending on fouling mechanism
k_a	Adsorption constant [$ppm^{-1}s^{-1}$]
k_d	Desorption constant [$ppm^{-1}s^{-1}$]
L	Pore length (membrane thickness) [m]
m	Mass ratio of wet to dry cake [-]
ΔP	Transmembrane pressure [N/m^2]
ΔP_t	Transmembrane pressure at time t [N/m^2]
ΔP_0	Transmembrane pressure at time 0 [N/m^2]
$\Delta P_t/ \Delta P_0$	Normalized transmembrane pressure [-]
Q	Volumetric flow rate [m^3/s]
R	Overall membrane resistance [m^{-1}]
R_0	Initial membrane resistance [m^{-1}]
r	Pore radius [m]
s	Mass fraction of solids in the fouling solution [-]
S	Rate of erosion of cake per unit area [$kg/(m^2 \cdot s)$]
t	Filtration time [s]
t*	Time at which the intermediate pore blocking ends [s]
TF	Threshold flux [$L/(m^2 \cdot h)$]
V	Filtrate volume [m^3]
W	Cake mass [kg]

Table 5.2, continued.

α	Cake specific resistance [m/kg]
γ	Filtrate density [kg/m^3]
λ	Exponential decay constant [1/s]
μ	Fluid viscosity [N·s/m^2]
σ	Blocked area per unit filtrate volume [m^{-1}]

5.5 REFERENCES

1. Kirschner, A. Y.; Cheng, Y. H.; Paul, D. R.; Field, R. W.; Freeman, B. D., Fouling Mechanisms in Constant Flux Crossflow Ultrafiltration. *Journal of Membrane Science* **2019,** *574*, 65-75.

2. Ognier, S.; Wisniewski, C.; Grasmick, A., Membrane Bioreactor Fouling in Sub-Critical Filtration Conditions: A Local Critical Flux Concept. *Journal of Membrane Science* **2004,** *229* (1), 171-177.

3. Miller, D. J.; Kasemset, S.; Paul, D. R.; Freeman, B. D., Comparison of Membrane Fouling at Constant Flux and Constant Transmembrane Pressure Conditions. *Journal of Membrane Science* **2014,** *454*, 505-515.

4. Howe, K. J.; Clark, M. M., Fouling of Microfiltration and Ultrafiltration Membranes by Natural Waters. *Environmental Science & Technology* **2002,** *36* (16), 3571-3576.

5. E.M. Van Wagner, A.C. Sagle, M.M. Sharma, B.D. Freeman, Effect of Crossflow Testing Conditions, Including Feed PH and Continuous Feed Filtration, on Commercial Reverse Osmosis Membrane Performance, Journal of Membrane Science, 345 (2009) 97-109.

Chapter 6: Surface Modification of Ultrafiltration Membranes with 1, 4-Benzoquinone and Polyetheramines

6.1 INTRODUCTION

Produced water from oil and gas production, together with flow back water from hydraulic fracturing, represents one of the largest anthropogenic waste streams.[1] Due to the highly impaired nature of this water and the energy investment required to purify it using conventional technology, most of it is disposed of via deep well injection.[2] Removal of emulsified oil from such wastewater could be an important step in making it useful for beneficial purposes, such as enhanced oil recovery and hydraulic fracturing.[2] Ultrafiltration membranes can efficiently remove emulsified oil droplets from water,[3-5] but fouling is a key challenge in using membranes to purify such wastewater streams.[3, 6]

Membrane surface modification to impart hydrophilic character to the surface can lead to formation of a strongly-bound layer of water molecules that reduces hydrophobic foulant adhesion.[7] Many modification strategies, such as poly(ethylene glycol) (PEG)-based coatings,[6, 8-9] grafted polymers (e.g., PEG brushes),[10-11] and zwitterionic polymers[12-14] have been considered as potential surface modification agents.[15] Polydopamine (pDA) has been widely studied as a membrane modification material and can be deposited onto almost any membrane by immersing the membrane in a slightly alkaline aqueous solution of dopamine.[16-17] The influence of pDA modification on membrane properties, such as hydrophilicity, surface charge, and surface roughness, has been reported previously.[16, 18-21] For example, Miller *et al.* observed enhanced fouling resistance of pDA modified UF membranes relative to unmodified UF membranes when challenged with an oily water emulsion.[22] Messersmith *et al.* suggested that the catechol and amine groups of dopamine

play critical roles in the oxidative polymerization and adhesion processes of pDA.[16] Therefore, materials with both amine and phenol groups may possess similar adhesion and hydrophilic properties. For example, Wang *et al.* found that polymerization between catechol and polyamine yielded a hydrophilic polymer.[22] The researchers used this material to modify polypropylene membranes for Li-ion battery separators. In addition, Xu *et al.* co-deposited catechol and polyethylenimine (PEI) to modify polyacrylonitrile (PAN) nanofiltration (NF) membranes.[23] These modified membranes showed excellent performance in separating a cationic dye and common inorganic salts from water.

Prior to the recent increase in surface modification research, Erhan *et al.* had reported an anti-corrosion coatings based on commercially available Jeffamine® and *p*-benzoquinone (BQ).[24-26] The reaction between diamines and quinones has been reported by others (*i.e.*, Fig. 6.1).[27] This chapter describes how commercially available flat-sheet polysulfone (PS) UF membranes were modified with BQ and several Jeffamines® and subjected to oily water fouling experiments. Among all tested samples considered, membranes modified with BQ and Jeffamines® EDR 148 (p(BQ-EDR148) modified membrane) were the most hydrophilic, as judged by contact angle experiments. The influence of these surface modifications on membrane pore size and distribution was investigated by molecular weight cut off (MWCO) experiments. MWCO results were used to calculate mean pore size and pore size distribution using the hindered transport model.[28]

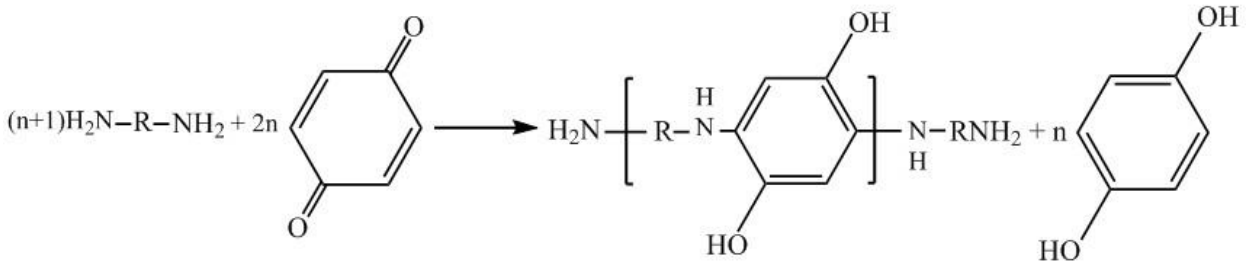

Fig. 6.1: Reaction mechanism between diamines and benzoquinones

6.2 RESULTS AND DISCUSSION

6.2.1 Pure water permeance and contact angle measurements of different poly(benzoquinone-Jeffamine®) modified membranes

In this chapter, different Jeffamines® containing 2 to 20 poly(ethylene oxide) (PEO) repeating units (*i.e.*, Jeffamine® EDR 148, ED-600, ED-900, and TTDDA, with chemical structures shown in Fig. 6.2) were polymerized with BQ to modify membrane surfaces. PEO is very hydrophilic, and many studies report that grafting PEO-monoamine (PEO-NH_2) to membrane surfaces improves hydrophilicity and fouling resistance of such modified membranes.[18, 20, 22] The influence of PEO backbone length on the modified membrane properties was investigated using the diamines listed above. Table 6.1 summarizes pure water permeance and contact angle values of PS membranes (UM PS-A, and UM PS-B), pDA modified membranes, and membranes modified with BQ and the different Jeffamines® mentioned above.

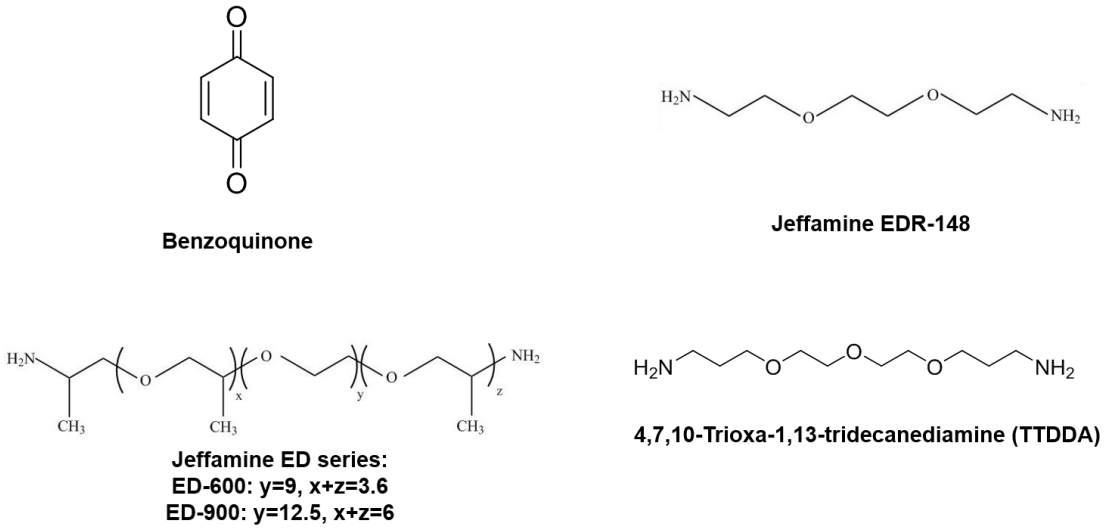

Fig. 6.2: The chemical structures of benzoquinone and Jeffamines®

Table 6.1: Permeance and contact angle of unmodified, pDA modified and p(BQ-Jeffamine) modified membranes. p(BQ-Jeffamine) modification conditions: 0.5 mg/mL of BQ, 1 hr deposition time, and a molar ratio of BQ to Jeffamine of 1:1. pDA modification conditions: 2 mg/mL and 1 hr of deposition time. Surface modification studies were performed on UM PS-B membranes.

Membrane	Permeance (LMH/bar)	Contact angle (^{0})
UM PS-A	900±200	109±1
UM PS-B	1620±230	83±5
pDA	910±90	32±7
p(BQ-ED 900)	1110±180	57±8
p(BQ-ED 600)	970±120	48±4
p(BQ-TTDDA)	1070±130	50±3
p(BQ-EDR 148)	960±130	32±3

One challenge in investigating the effect of surface modification on membrane performance is isolating the influence of surface modification on a variety of membrane properties (*e.g.*, hydrophilicity, permeance, surface roughness) that can change as a consequence of the modification. For example, pDA modification usually leads to an increase in surface hydrophilicity but a decrease in membrane permeance.[22] Fouling performance is affected by both of these factors, so comparing membrane performance before and after surface modification is a challenge. To address this difficulty, two PS membranes, UM PS-A and UM PS-B, with different pure water permeance values were used in this study. Surface modifications were performed on UM PS-B, which has a higher pure water permeance than UM PS-A. The deposition times were adjusted such that the pure water permeance of all modified membranes was similar to that of UM PS-A (900±200 LMH). Comparing the fouling performance of membranes with similar pure water permeance values helps to separate the influence of hydrophilicity and permeance on membrane fouling performance.

Contact angle measurements, with *n*-decane as the probe liquid, were used to characterize membrane surface hydrophilicity. Lower contact angle indicates higher surface hydrophilicity. As shown in Table 6.1, the modified membranes exhibit lower contact angles than those of the two unmodified PS-20 membranes, which suggests improved hydrophilicity after modification. However, the use of diamines containing more PEO repeat units did not result in coatings that were more hydrophilic, which may be due to the less hydrophilic poly(propylene oxide) moieties in coatings. Moreover, most of the p(BQ-Jeffamine) modified membranes possess lower hydrophilicity relative to the pDA modified membranes. The exception is p(BQ-EDR 148), whose contact angle is similar to that of the pDA modified membrane. Among the p(BQ-Jeffamine) coating materials

evaluated in this work, p(BQ-EDR 148) is the most hydrophilic and is comparable to results obtained with pDA. The following section will focus on p(BQ-EDR 148).

6.2.2 MWCO of unmodified, pDA and p(BQ-EDR 148) modified membranes

The influence of surface modification on pore size properties was investigated using molecular weight cut-off (MWCO) experiments, and the results are presented in Fig. 6.3. The MWCO and nominal pore size of UM PS-B membranes are slightly higher than those of UM PS-A, which may be part of the reason that UM PS-B has a higher pure water permeance than UM PS-A. The p(BQ-EDR 148) modified membranes have a higher MWCO than do the pDA modified membranes, but both modified membranes show lower MWCO, as well as steeper rejection curves, compared to the two unmodified membranes. The slope of the rejection curve is a qualitative indicator of pore size distribution.[29-30] The steeper curves of both modified membranes imply a narrower pore size distribution than those of unmodified membranes. The decrease in nominal pore sizes and the steep rejection curves confirm that surface modification leads to pore blocking or shrinkage.

Pore size properties strongly affect membrane filtration/fouling performance.[31] For example, pore blocking due to surface modification, along with the reduced nominal pore size, allows fewer oil droplets to penetrate through the pores, so rejection increases. However, the local flux through the remaining open pores after surface modification may be higher to maintain an overall constant flux. As a result, pore blocking by modification sometimes makes membranes more vulnerable to internal fouling.[31] The impacts on fouling performance of different membrane pore size properties will be discussed in the following sections.

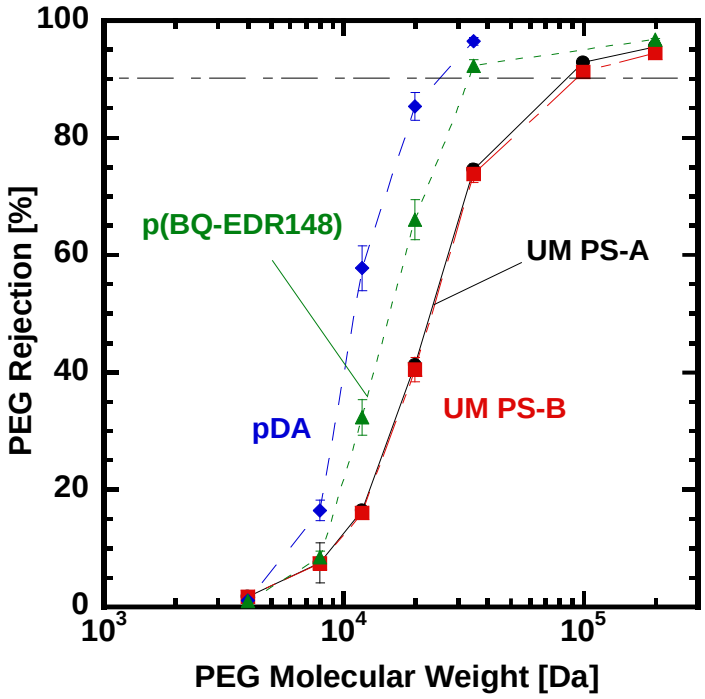

Membrane	MWCO (kDa)	Nominal pore size (nm)
UM PS-A	85±1	9.3±0.1
UM PS-B	93±6	9.8±0.3
pDA	25±4	4.7±0.4
p(BQ-EDR 148)	33±2	5.5±0.2

Fig. 6.3: MWCO curves of unmodified, pDA and p(BQ-EDR 148) modified membranes, and a table of the corresponding MWCO and nominal pore size values. The modification conditions are the same as those in Table 6.1.

6.2.3 Flux stepping and constant flux fouling experiments of unmodified, pDA and p(BQ-EDR 148) modified membranes

Fig. 6.4 presents results from flux stepping experiments to determine the threshold flux (TF) for membranes modified with p(BQ-EDR 148). Detail of TF determination can be found in Section 4.4.4.1-4.4.4.4. Results from a representative flux stepping experiment are presented in Fig. 6.4(a). TMP_{avg} values at each flux, calculated from the data in Fig. 6.4(a), are shown in Fig. 6.4(b). The TMP_{avg} values were calculated by excluding the first two minutes of data collected at the beginning of each step, while the TMP is still in transition from the previous flux step, and then computing the mean TMP for the remaining 18 minutes. All TMP_{avg} values from 10 LMH to 70 LMH in Fig. 6.4(b) lie on a single linear regression line having R^2 values larger than 0.99. The linearity indicates that the membrane mass transfer resistance is constant at these fluxes. However, flux vs. TMP_{avg} relation changes abruptly at about 80 LMH. A second line was drawn between the first two points following this break in linearity (*i.e.*, the TMP_{avg} values at 80 and 90 LMH). The flux at the intersection of this line and the first regression line, 76 LMH, is defined as the threshold flux by the TMP_{avg} method.[22]

Fig. 6.4(c) shows ΔTMP as a function of flux. These ΔTMP values are calculated from the step change in TMP when the flux is increased to the flux on the x-axis (e.g., the TMP rose by 0.02 bar when the flux was increased from 10 LMH to 20 LMH). No value is shown at 10 LMH because 10 LMH is the lowest flux considered in the flux stepping experiment. The threshold flux is the flux above which the relationship between ΔTMP and flux becomes convex to the flux axis.[22] At flux values below 70 LMH, ΔTMP changed approximately linearly with flux, but it increased sharply when the flux was above about 70 LMH. Thus, the threshold flux is approximately 70 LMH, as determined by the ΔTMP method.

Fig. 6.4(d) shows d(TMP)/dt as a function of flux. At flux values below about 80 LMH, d(TMP)/dt values are low and fluctuate around zero. However, the d(TMP)/dt increased dramatically at 90 LMH, significantly exceeding the highest value observed between 10 LMH and 80 LMH, indicating that 90 LMH exceeds the threshold flux. Therefore, a line was drawn through the d(TMP)/dt values at 80 LMH and 90 LMH, in addition to a horizontal line through the highest d(TMP)/dt value (*i.e.*, 2.6×10^{-6} at 70 LMH observed at fluxes between 10 and 80 LMH). The threshold flux was determined by finding the intersection of these two lines.[22]

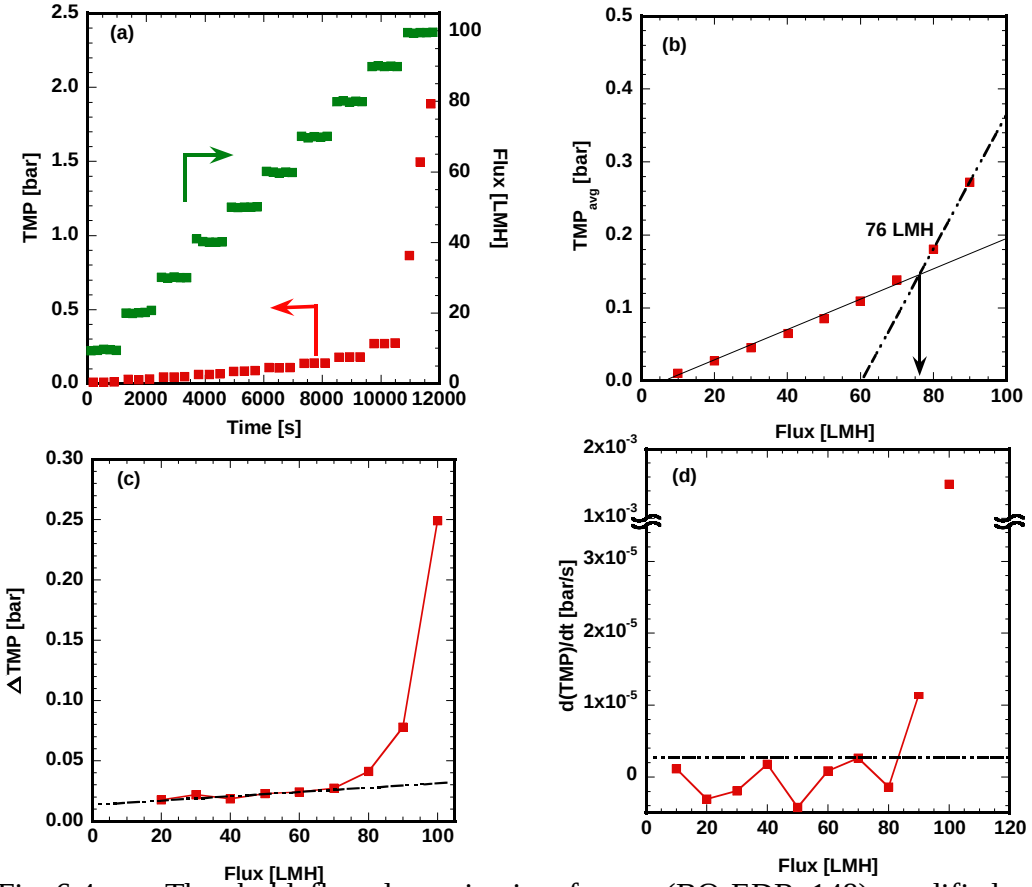

Fig. 6.4: Threshold flux determination for a p(BQ-EDR 148) modified membrane challenged with 1500 ppm soybean oil emulsion. (a) Threshold flux data. Threshold flux determined from (b) the TMPavg method, (c) ΔTMP method, and (d) d(TMP)/dt method. The values shown in (b)-(d) were calculated from the data presented in (a).

Table 6.2: Threshold flux values of unmodified, pDA-modified, and p(BQ-Jeffamine®) modified membranes determined by three different methods.[22]

	Threshold flux (LMH)		
Membrane	**TMP_{avg} method**	**ΔTMP method**	**d(TMP/dt) method**
UM PS-A[22]	65	65	65
UM PS-B	76±0.3	75±5	77±3
pDA	74±1	70±7	80±1
p(BQ-EDR 148)	76±0.2	70±0.5	85±2

In addition to the p(BQ-EDR 148) modified membranes, flux stepping experiments were performed on unmodified and pDA modified membranes. The threshold flux values of all membranes determined by the three methods are recorded in Table 6.2. For UM PS-A, the threshold flux values obtained by the three methods are the same. The threshold flux of UM PS-B is higher than that of UM PS-A, likely due to the larger pore size of UM PS-B, as indicated by its higher pure water permeance (see Table 6.1) and higher MWCO (Fig. 6.3). For the other modified membranes, the three determination methods yield somewhat varying threshold flux values. These results are similar to those reported for pDA modified membranes in a previous publication.[22] As interactions between the membrane surface and hydrophobic foulants become weaker, due to the surface becoming hydrophilic, the changes measured by each of the three parameters may become less pronounced and more difficult to detect.[22] Although the threshold flux values determined by the three parameters for modified membranes do not always give exactly the same values, they are nonetheless useful for revealing the impact of surface modification by providing a range of approximate values. These threshold flux values can be validated using constant flux fouling experiments. All three threshold flux values for p(BQ-EDR 148) modified membranes are

higher than those for UM PS-A and are comparable to those of the pDA-modified membranes. These results indicate that p(BQ-EDR 148) significantly improves fouling resistance compared to unmodified polysulfone membranes (*i.e.*, UM PS-A).

To validate the results of the flux stepping studies, constant flux experiments were performed with unmodified, pDA modified, and p(BQ-EDR 148) modified membranes at three different fluxes. The results are shown in Fig. 6.5. At 55 LMH (Fig. 6.5(a)), which is below the measured threshold flux values of all the membranes, the TMP increased primarily at the start of the test (*i.e.*, at V/A less than 1 cm), then reached a plateau for the remainder of the experiment. This TMP evolution implies that fouling at 55 LMH is minimal for all three membranes. The steady state TMP values for the two modified membranes are higher than those of the unmodified membranes, which is similar to the results of other studies.[21, 31] As mentioned earlier, surface modification leads to pore blockage, which decreases the MWCO of both modified membranes. This pore blocking effect outweighs the improved hydrophilicity at this low permeate flux, resulting in higher TMP for both modified membranes. Both modified membranes have higher rejection values (*i.e.*, R in Fig. 6.5) than that of UM PS-A, and this effect is also due to the decrease in MWCO after modification. Although an increase in hydrophilicity provides little improvement at 55 LMH, improved hydrophilicity does play an essential role at 70 LMH (Fig. 6.5(b)). The two hydrophilic modified membranes show a TMP evolution similar to their 55 LMH cases, which means that 70 LMH is still below the threshold flux of these membranes. In contrast, the TMP of the unmodified membranes dramatically increases after 4 cm, indicating that 70 LMH is above their threshold flux. At 80 LMH (Fig. 6.5(c)), all membranes show sharp increases in TMP, confirming that 80 LMH is above the threshold flux values of all three membranes. The TMP curve of p(BQ-EDR 148) modified membranes exhibits concaves down behavior and reaches a pseudo-steady state TMP

around 1.7 barg. This TMP profile has also been reported elsewhere.[32-33] Z. He *et al*. hypothesized that high TMP may push deformable foulants through membranes and contribute to a pseudo-steady state TMP in the high TMP regime.[33] Based on the results of flux stepping and constant flux experiments at 70 LMH, the new p(BQ-EDR 148) modified membrane has better fouling resistance than the unmodified PS membrane does, and at the conditions considered, it shows fouling resistance comparable to that of pDA modified membranes.

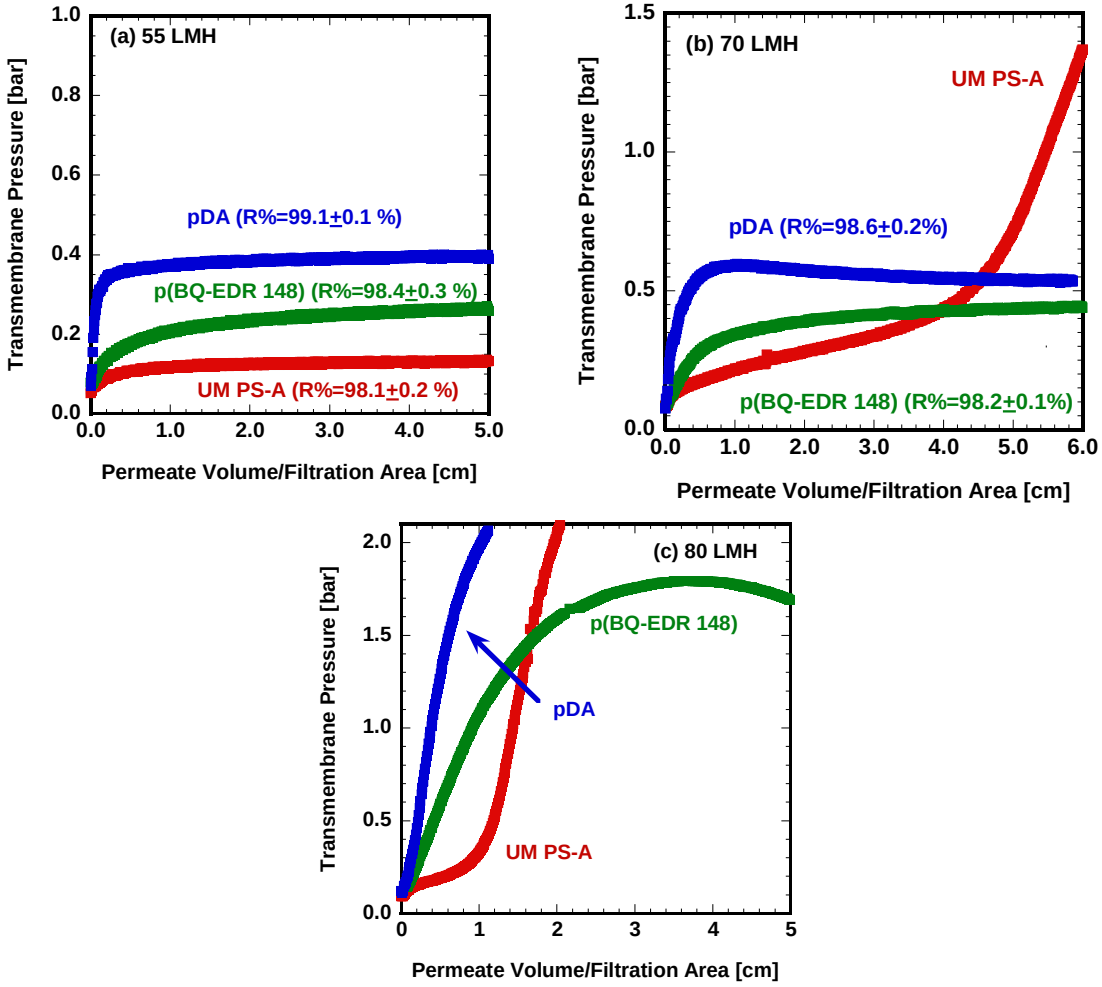

Fig. 6.5: Constant flux fouling experiments of unmodified, pDA modified, and p(BQ-EDR 148) modified membranes at three different fluxes: (a) 55 LMH, (b) 70 LMH and (c) 80 LMH.

6.2.4 Influence of deposition time and molar ratio on pore size properties

Surface modification can change not just hydrophilicity but also pore size properties. Kasemset *et al.* evaluated changes in PS-20 pore size and pore size distribution of an ultrafiltration membrane due to pDA modification.[28] The two experimental parameters used to control pDA modification, deposition time and dopamine concentration, showed similar effects on mean pore size and distribution. For example, the mean pore size increased when membranes were coated with low dopamine concentration (e.g., 1 mg/mL) or when the deposition time was short, but mean pore size and distribution decreased with more aggressive modification conditions (e.g., long deposition times or high dopamine concentrations). Moreover, pure water permeance also decreased as dopamine concentration and deposition time increased. A change in permeance usually accompanies a change in pore size properties, and it is difficult to control pore size properties without changing permeance. In contrast, the new material, p(BQ-EDR 148), possesses an additional parameter that may enable fine-tuning of pore size and distribution: the molar ratio of the coating reagents. To explore this hypothesis, we first investigated the effects of deposition time and molar ratio separately, and then attempted to tune the pore size at fixed permeance while changing both of these parameters.

Fig. 6.6 and Table 6.3 present the impact of increasing deposition time, from 1 hr to 2.5 hr, on pore size distribution and pure water permeance. All modified membranes exhibit larger mean pore sizes and narrower distributions than do unmodified membranes. As deposition time rises from 1 hr to 1.5 hr, the mean pore size initially increases, then, at longer deposition time (*i.e.*, 2 and 2.5 hr), starts to decrease. This trend is similar to the effect of increasing deposition time during pDA modification of UM membranes.[28] When membranes are modified at short deposition times, coating the insides of pores will decreases their radii and may even close small pores, but it may not coat bigger pores

sufficiently to reduce their radii significantly. Consequently, the pore size distribution shifts to higher mean pore size at short deposition times. At longer deposition times (*i.e.*, 2 and 2.5 hr), the coating not only blocks small pores but also begins to decrease the size of larger pores, resulting in a decrease of mean pore size. As shown in Fig. 6.6(c), pure water permeance continuously decreases with increasing deposition time. The qualitative influence of increasing deposition time on pore size distribution and pure water permeance is similar to that observed for pDA modification of UF membranes.[28]

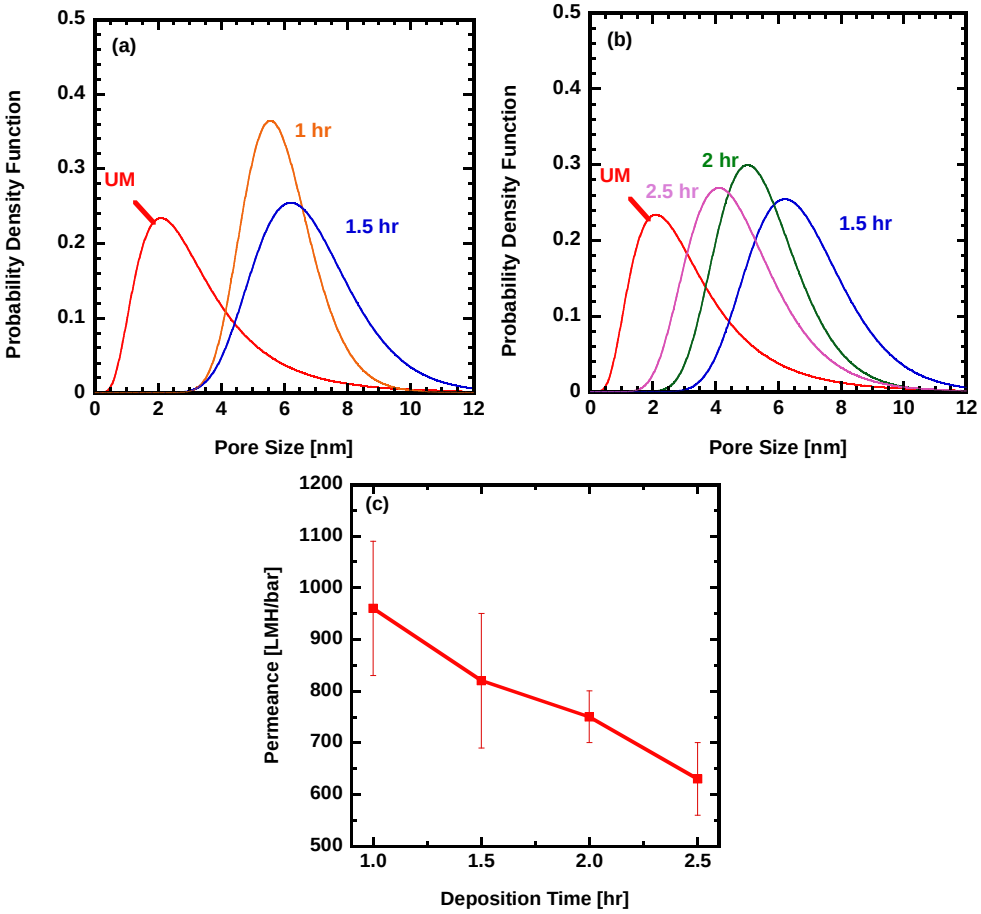

Fig. 6.6: Pore size distribution of unmodified membranes and p(BQ-EDR 148) modified membranes with (a) short, and (b) long deposition times. (c) Effects of modification deposition time on pure water permeance. Other modification conditions: BQ concentration: 0.5 mg/mL, BQ to EDR 148 molar ratio is 1:1. The unmodified membranes are UM PS-A.

Table 6.3: Mean pore sizes and standard deviations of pore size distribution (σ) of p(BQ-EDR 148) modified membranes prepared at various deposition times. Other modification conditions: BQ concentration: 0.5 mg/mL, and the BQ to EDR 148 molar ratio is 1:1.

Deposition time (hr)	**Mean pore size (nm)**	**σ (nm)**
0 (UM)	2.8	2.3
1	5.8	1.1
1.5	6.6	1.6
2	5.4	1.4
2.5	4.6	1.6

To investigate the influence of reactant molar ratio, the concentration of EDR 148 was varied while the concentration of BQ (0.5 mg/mL) and the deposition time (1 hr) remained constant. Fig. 6.7 and Table 6.4 show the influence of the BQ to EDR 148 molar ratio on pore size properties and pure water permeance. Due to small pore blockage, as described earlier, all modified membranes have larger mean pore sizes and narrower distribution than do the unmodified membranes, and they have similar mean pore size values (~5.4-6.0 nm), indicating that all molar ratios have a similar influence on mean pore size. Furthermore, increasing BQ to EDR 148 ratio continuously increases pure water permeance, as shown in Fig. 6.7(c). The molar ratio experimental parameter can potentially

serve as a tool for fine-tuning pure water permeance without a large change in mean pore size.

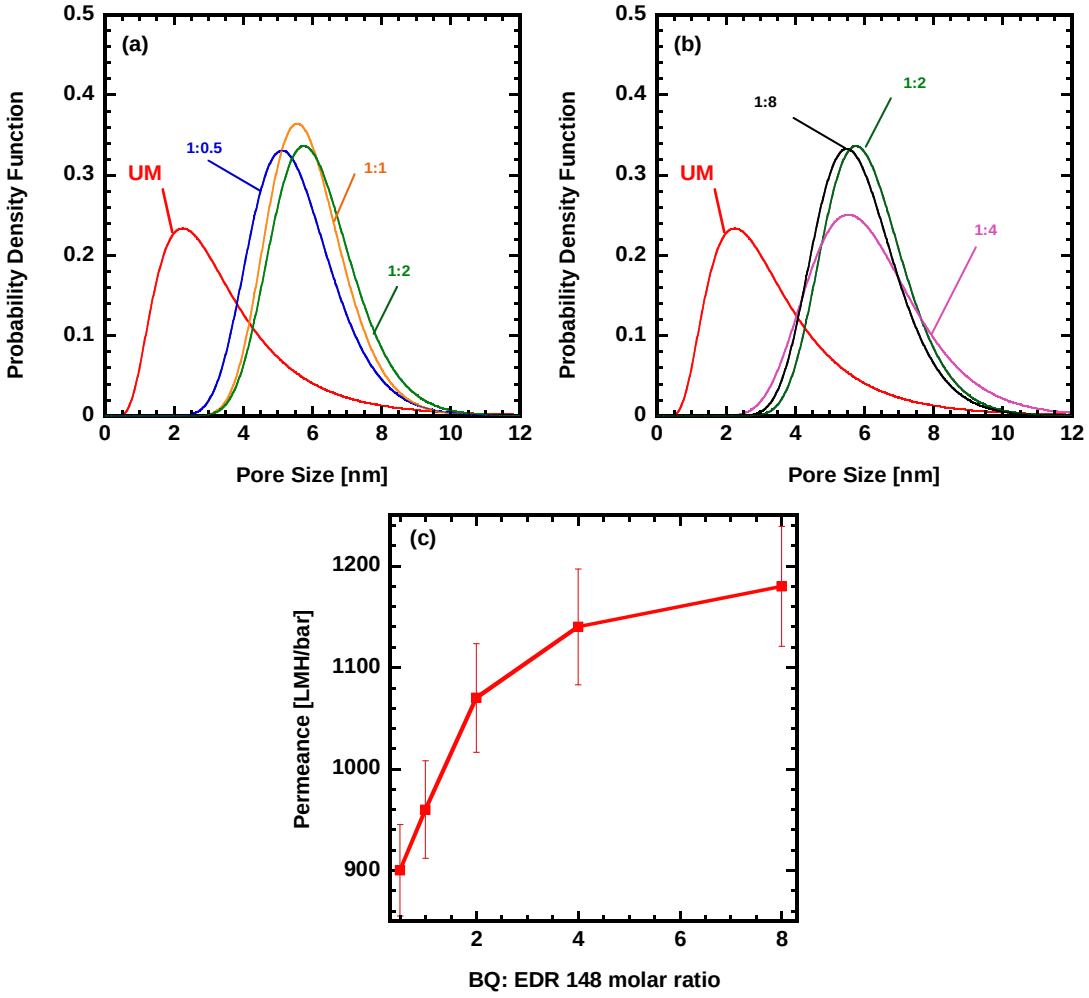

Fig. 6.7: Pore size distribution of unmodified membranes and p(BQ-EDR 148) modified membranes with (a) moderate and (b) excessive BQ: EDR 148 molar ratio. (c) Influence of BQ: EDR 148 molar ratio on pure water permeance. Other modification conditions: BQ concentration: 0.5 mg/mL, deposition time: 1 hr. The numbers in (a) and (b) are the molar ratios of BQ to EDR 148.

Table 6.4: Mean pore sizes and standard deviations of unmodified membranes and p(BQ-EDR 148) modified membranes prepared at various molar ratios of reactants. Other modification conditions: BQ concentration: 0.5 mg/mL, deposition time: 1 hr.

BQ: EDR 148 ratio	**Mean pore size (nm)**	**σ (nm)**
UM	2.8	2.3
1:0.5	5.4	1.3
1:1	5.8	1.1
1:2	6.0	1.2
1:4	6.0	1.7
1:8	5.7	1.2

As mentioned before, manipulating these parameters may control the pore size distribution without changing the pure water permeance. To test this hypothesis, membranes were modified with p(BQ-EDR 148) at various ratios and deposition times. Table 6.5 summarizes the permeance and contact angle values of p(BQ-EDR 148) modified membranes. Because increasing BQ:EDR 148 molar ratio leads to an increase in pure water permeance, while increasing deposition time has the opposite effect, the deposition time and molar ratio were raised simultaneously to maintain a constant pure water permeance. The contact angles for all modified membranes are similar, which suggests that the chemical structure of the surface modification likely remains similar when two parameters are changed simultaneously.

Table 6.5: Permeance and contact angle of p(BQ-EDR 148) modified membrane with various molar ratios and deposition times. The molar ratios shown in the table are the ratios of BQ to EDR 148 in the coating solution. The BQ concentration in the coating solution was 0.5 mg/mL in all cases.

Membrane		**Permeance (LMH/bar)**	**Contact angle (^{0})**
Deposition time (hr)	**BQ:EDR 148 ratio**		
1	1:0.5	900±120	29±5
1	1:1	960±130	32±3
1.5	1:2	980±70	26±3
2	1:4	960±150	30±5
2.5	1:8	1040±100	29±3

Fig. 6.8 and Table 6.6 present the mean pore sizes and pore size distributions of unmodified membranes and p(BQ-EDR 148) modified membranes. At low BQ:EDR 148 molar ratio conditions and short deposition times (*i.e.*, Fig. 6.8(a)), the mean pore size increases with BQ: EDR 148 ratios and deposition times. However, when more EDR 148 and long deposition times are used (*i.e.*, 1:4, 2 hr and 1:8, 2.5 hr in Fig. 6.8(b)), the mean pore size decreases relative to the largest pore size obtained (*i.e.*, with molar ratio of 1:2 and 1.5 hr deposition time). Because the trend in pore size distribution change is similar to that when only the deposition time is increased (cf. Fig. 6.6 and Table 6.3), differences in

pore size distribution can be attributed primarily to the influence of longer deposition times. The increase in molar ratio increases the pure water permeance rise and compensates for the influence of increasing deposition time but has little influence on pore size distribution. Based on the results shown in Fig. 6.8, the pore size distribution of modified membranes can be controlled by altering these two parameters.

Table 6.6: Mean pore sizes of unmodified and p(BQ-EDR 148) modified membranes with various molar ratios and deposition times. The molar ratios shown in the table are the ratios of BQ to EDR 148 in the coating solution. The BQ concentration in the coating solution was 0.5 mg/mL in all cases.

Membrane		**Mean pore size (nm)**	**σ (nm)**
Deposition time (hr)	**BQ:EDR 148 ratio**		
0 (UM)	-	2.84	2.25
1	1:0.5	5.39	1.25
1	1:1	5.77	1.13
1.5	1:2	6.78	1.02
2	1:4	5.85	1.14
2.5	1:8	5.44	1.18

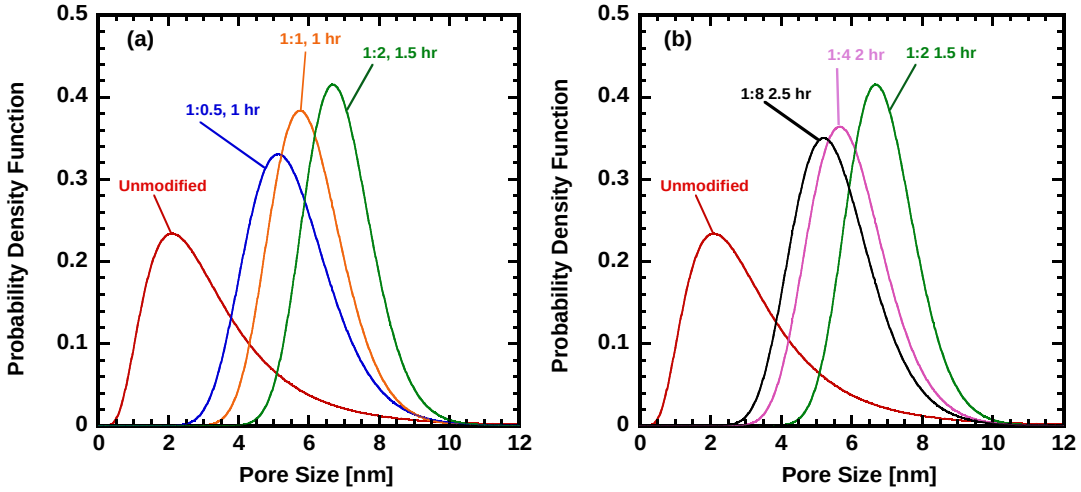

Fig. 6.8: Probability density function of pore size distributions of unmodified membranes and p(BQ-EDR 148) modified membranes with (a) BQ: EDR 148 ratios of 1:0.5, 1:1 and 1:2, deposition times of 1, 1, and 1.5 hr, respectively, and (b) BQ: EDR 148 ratios of 1:2, 1:4 and 1:8, deposition time of 1.5, 2 and 2.5, respectively.

6.3 REFERENCES

1. Mueller, J.; Cen, Y.; Davis, R. H., Crossflow Microfiltration of Oily Water. *Journal of Membrane Science* **1997,** *129* (2), 221-235.

2. Rassenfoss, S., From Flowback to Fracturing: Water Recycling Grows in the Marcellus Shale. *Journal of Petroleum Technology* **2011,** *63* (07), 48-51.

3. Baker, R. W., *Membrane Technology and Applications. 2nd Ed.* Wiley: 2004.

4. Geise, G. M.; Lee, H.-S.; Miller, D. J.; Freeman, B. D.; McGrath, J. E.; Paul, D. R., Water Purification by Membranes: The Role of Polymer Science. *Journal of Polymer Science Part B: Polymer Physics* **2010,** *48* (15), 1685-1718.

5. J.R. Pressdee, S. V., H.L. Shorney-Darby, J.A. Clement, J.P. Van der Hoek, *Integration of Membrane Filtration into Water Treatment Systems*. American Water Works Association Research Foundation and U.S. Department of the Interior, Bureau of Reclamation: 2006.

6. Ju, H.; McCloskey, B. D.; Sagle, A. C.; Kusuma, V. A.; Freeman, B. D., Preparation and Characterization of Crosslinked Poly(Ethylene Glycol) Diacrylate Hydrogels as Fouling-Resistant Membrane Coating Materials. *Journal of Membrane Science* **2009,** *330* (1–2), 180-188.

7. Elimelech, M.; Phillip, W. A., The Future of Seawater Desalination: Energy, Technology, and the Environment. *Science* **2011,** *333* (6043), 712-717.

8. Ju, H.; McCloskey, B. D.; Sagle, A. C.; Wu, Y.-H.; Kusuma, V. A.; Freeman, B. D., Crosslinked Poly(Ethylene Oxide) Fouling Resistant Coating Materials for Oil/Water Separation. *Journal of Membrane Science* **2008,** *307* (2), 260-267.

9. Sagle, A. C.; Van Wagner, E. M.; Ju, H.; McCloskey, B. D.; Freeman, B. D.; Sharma, M. M., PEG-Coated Reverse Osmosis Membranes: Desalination Properties and Fouling Resistance. *Journal of Membrane Science* **2009,** *340* (1–2), 92-108.

10. Roosjen, A.; Kaper, H. J.; van der Mei, H. C.; Norde, W.; Busscher, H. J., Inhibition of Adhesion of Yeasts and Bacteria by Poly(Ethylene Oxide)-Brushes on Glass in a Parallel Plate Flow Chamber. *Microbiology* **2003,** *149* (11), 3239-3246.

11. Ulbricht, M.; Matuschewski, H.; Oechel, A.; Hicke, H.-G., Photo-Induced Graft Polymerization Surface Modifications for the Preparation of Hydrophilic and Low-Proten-Adsorbing Ultrafiltration Membranes. *Journal of Membrane Science* **1996,** *115* (1), 31-47.

12. Cai, T.; Li, X.; Wan, C.; Chung, T.-S., Zwitterionic Polymers Grafted Poly(Ether Sulfone) Hollow Fiber Membranes and Their Antifouling Nehaviors for Osmotic Power Generation. *Journal of Membrane Science* **2016,** *497*, 142-152.

13. Jiang, S.; Cao, Z., Ultralow-Fouling, Functionalizable, and Hydrolyzable Zwitterionic Materials and Their Derivatives for Biological Applications. *Advanced Materials* **2010,** *22* (9), 920-932.

14. Zhao, Y.-H.; Wee, K.-H.; Bai, R., Highly Hydrophilic and Low-Protein-Fouling Polypropylene Membrane Prepared by Surface Modification with Sulfobetaine-Based Zwitterionic Polymer through a Combined Surface Polymerization Method. *Journal of Membrane Science* **2010,** *362* (1–2), 326-333.

15. Miller, D. J.; Dreyer, D. R.; Bielawski, C. W.; Paul, D. R.; Freeman, B. D., Surface Modification of Water Purification Membranes. *Angewandte Chemie International Edition* **2017,** *56* (17), 4662-4711.

16. Lee, H.; Dellatore, S. M.; Miller, W. M.; Messersmith, P. B., Mussel-Inspired Surface Chemistry for Multifunctional Coatings. *Science* **2007,** *318* (5849), 426-430.

17. Lee, H.; Lee, Y.; Statz, A. R.; Rho, J.; Park, T. G.; Messersmith, P. B., Substrate-Independent Layer-by-Layer Assembly by Using Mussel-Adhesive-Inspired Polymers. *Advanced Materials* **2008,** *20* (9), 1619-1623.

18. McCloskey, B. D.; Park, H. B.; Ju, H.; Rowe, B. W.; Miller, D. J.; Freeman, B. D., A Bioinspired Fouling-Resistant Surface Modification for Water Purification Membranes. *Journal of Membrane Science* **2012,** *413–414*, 82-90.

19. McCloskey, B. D.; Park, H. B.; Ju, H.; Rowe, B. W.; Miller, D. J.; Chun, B. J.; Kin, K.; Freeman, B. D., Influence of Polydopamine Deposition Conditions on Pure Water Flux and Foulant Adhesion Resistance of Reverse Osmosis, Ultrafiltration, and Microfiltration Membranes. *Polymer* **2010,** *51* (15), 3472-3485.

20. Kasemset, S.; Lee, A.; Miller, D. J.; Freeman, B. D.; Sharma, M. M., Effect of Polydopamine Deposition Conditions on Fouling Resistance, Physical Properties, and Permeation Properties of Reverse Osmosis Membranes in Oil/Water Separation. *Journal of Membrane Science* **2013,** *425–426*, 208-216.

21. Kasemset, S.; He, Z.; Miller, D. J.; Freeman, B. D.; Sharma, M. M., Effect of Polydopamine Deposition Conditions on Polysulfone Ultrafiltration Membrane Properties and Threshold Flux During Oil/Water Emulsion Filtration. *Polymer* **2016,** *97*, 247-257.

22. Miller, D. J.; Kasemset, S.; Wang, L.; Paul, D. R.; Freeman, B. D., Constant Flux Crossflow Filtration Evaluation of Surface-Modified Fouling-Resistant Membranes. *Journal of Membrane Science* **2014,** *452*, 171-183.

23. Xu, Y. C.; Wang, Z. X.; Cheng, X. Q.; Xiao, Y. C.; Shao, L., Positively Charged Nanofiltration Membranes via Economically Mussel-Substance-Simulated Co-Deposition for Textile Wastewater Treatment. *Chemical Engineering Journal* **2016,** *303*, 555-564.

24. Kaleem, K.; Chertok, F.; Erhan, S., A Novel Coating Based on Poly(Etheramine-Quinone) Polymers. *Progress in Organic Coatings* **1987,** *15* (1), 63-71.

25. Kaleem, K.; Chertok, F.; Erhan, S., Quinone–Amine Polymers. II. 1,3-Bis(3-Aminophenoxy) Benzene-P-Benzoquinone Oligomers. *Journal of Polymer Science Part A: Polymer Chemistry* **1989,** *27* (3), 865-872.

26. Reddy, T. A.; Macaione, D.; Erhan, S., Quinone-Amine Polymers. XV. Syntheses and Characterization of High-Temperature Resistant Poly(Arylamino-Quinone)S. *Journal of Polymer Science Part A: Polymer Chemistry* **1994,** *32* (10), 1977-1982.

27. Fischer, E.; Schrader, H., Verbindungen Von Chinon Mit Aminosäureestern. *Berichte der Deutschen Chemischen Gesellschaft* **1910,** *43* (1), 525-529.

28. Kasemset, S.; Wang, L.; He, Z.; Miller, D. J.; Kirschner, A.; Freeman, B. D.; Sharma, M. M., Influence of Polydopamine Deposition Conditions on Hydraulic Permeability, Sieving Coefficients, Pore Size and Pore Size Distribution for a Polysulfone Ultrafiltration Membrane. *Journal of Membrane Science* **2017,** *522*, 100-115.

29. Zeman, L.; Wales, M., Polymer Solute Rejection by Ultrafiltration Membranes. In *Synthetic Membranes: Volume II*, AMERICAN CHEMICAL SOCIETY: 1981; Vol. 154, pp 411-434.

30. Mochizuki, S.; Zydney, A. L., Theoretical Analysis of Pore Size Distribution Effects on Membrane Transport. *Journal of Membrane Science* **1993,** *82* (3), 211-227.

31. Kirschner, A. Y.; Chang, C.-C.; Kasemset, S.; Emrick, T.; Freeman, B. D., Fouling-Resistant Ultrafiltration Membranes Prepared via Co-Deposition of Dopamine/Zwitterion Composite Coatings. *Journal of Membrane Science* **2017,** *541*, 300-311.

32. Liu, Q.-F.; Kim, S.-H., Evaluation of Membrane Fouling Models Based on Bench-Scale Experiments: A Comparison between Constant Flowrate Blocking Laws and Artificial Neural Network (Anns) Model. *Journal of Membrane Science* **2008,** *310* (1), 393-401.

33. He, Z.; Miller, D. J.; Kasemset, S.; Wang, L.; Paul, D. R.; Freeman, B. D., Fouling Propensity of a Poly(Vinylidene Fluoride) Microfiltration Membrane to Several Model Oil/Water Emulsions. *Journal of Membrane Science* **2016,** *514*, 659-670.

Chapter 7: Conclusions and Recommendations

7.1 Fouling Mechanisms in Constant Flux Crossflow Ultrafiltration

A combined intermediate pore blocking and cake filtration model was developed to describe fouling of a poly(ether sulfone) ultrafiltration membrane by a 0.22 micron 200 ppm latex bead suspension or a 200 ppm soybean oil emulsion. Below the threshold flux, the intermediate pore blocking model correlated well with experimental data. Above the threshold flux, the combined intermediate pore blocking/cake filtration model gave the most accurate fits. Based on this observation, the following definition of the threshold flux is proposed: *the flux below which cake buildup is negligible and above which cake filtration becomes the dominant fouling mechanism*. Based on a mathematical analysis of the combined model, the model and the definition are consistent with empirical threshold flux determination methods. A flux stepping experiment was simulated using fitting parameters from constant flux crossflow fouling experiments. For rigid particles, the simulation matched the experimental flux stepping data closely. Analysis of flux stepping experiments using the proposed models could enable prediction of fouling behavior in constant flux fouling experiments.

[*] This chapter has been adapted with permission from sections of:

Kirschner, A.Y.; Cheng, Y.H; Paul, D.R.; Field, R.W.; Freeman; B.D. Fouling mechanisms in constant flux crossflow ultrafiltration. *Journal of Membrane Science* **2019**, 574, 65-75. Kirschner wrote the manuscript and performed experimental and modeling work; Cheng performed experimental and modeling work and assisted with writing; Field, Paul, and Freeman advised the project and assisted with writing.

7.2 Complete Coverage Model (CCM)

The intermediate pore blocking model proposed in Chapter 4 can qualitatively describe membrane fouling far below the threshold flux, but its prediction deviates from experimental data when foulant concentration/permeate flux is high. To solve this issue, a complete coverage model is proposed in Chapter 5. The complete coverage model assumes that particle deposition leads to hindrance (rather than complete blocking) of permeate flow through the membrane pores, which increases membrane resistance. Based on this model, changes in operating conditions have little impact on the normalized transmembrane pressure (TMP) profile at high concentrations because the foulant deposition rate overwhelms the foulant removal rate, and the membrane surface is mostly covered by foulant particles. At low concentrations, the CCM model predicts that an increase in crossflow rate should decrease the normalized TMP. Increases in concentration or permeate flux lead to an 'increase-then-plateau' influence on normalized, steady TMP. Combining the complete coverage model and cake filtration provides better agreement with experimental data than does a model that combines intermediate pore blocking and cake filtration.

7.3 Surface Modification of Ultrafiltration Membranes with 1, 4-Benzoquinone and Polyetheramines

Fouling resistant polysulfone ultrafiltration membranes were prepared by modifying commercial ultrafiltration membranes with poly(benzoquinone-Jeffamine®) (p(BQ-Jeffamine®)). All modifications were done on a membrane with high permeance, and the modification conditions were adjusted so that all membranes had similar permeance. Contact angle results showed that modified membranes have higher hydrophilicity than unmodified membranes. Only p(BQ-EDR 148) modified membranes, however, possess a low contact angle comparable to that of polydopamine (pDA) modified

membranes. The threshold fluxes of p(BQ-EDR 148) modified membranes are significantly higher than those of unmodified membranes and are comparable to the threshold fluxes of pDA modified membranes. The results of contact angle, flux stepping measurements, and constant flux experiments indicate that p(BQ-EDR 148) coatings have hydrophilicity and fouling resistance similar to those of pDA coatings.

The effects of molar ratio and deposition time on membrane properties were also investigated. The results of permeance tests and molecular weight cut off (MWCO) experimental modeling show that pure water permeance decreases with increasing deposition time, and the mean pore size first increases with increasing deposition time to 1.5 hr, then decreases when the deposition time exceeds 1.5 hr. The effects of increasing deposition time are similar to those reported from a previous study of pDA modification.[1] In contrast, increasing the BQ: EDR 148 ratio leads to an increase in permeance but has a negligible impact on mean pore size. Manipulating the molar ratio parameter allows better control of membrane properties and may ultimately lead to better ultrafiltration membrane design.

7.4 Recommended Future Work

7.4.1 Dopamine alternatives

Further investigation of materials that have similar structure to pDA (hydroquinone, aminophenol, etc.) should be conducted to understand the role of different functional groups and configurations on coating properties:

- Constant flux crossflow fouling experiments comparing different isomers of the same material will isolate the effect of configuration on coating properties and fouling resistance.

- High/low pH tolerance and chlorine tolerance tests should be conducted to observe the effect of different configurations, and the absence or presence of certain functional groups, on coating durability.
- Molecular weight cutoff and thickness measurements are needed to determine differences in coating kinetics for different chemical structures. Changes in pore size distribution can affect rejection, pure water permeance, and fouling resistance of membranes.

7.4.2 Microfiltration fouling model in constant flux crossflow filtration

The fouling models discussed in Chapter 4 and Chapter 5 are applicable only to fouling of ultrafiltration membranes, where internal fouling is minimal. For microfiltration, TMP evolution during filtration is a coupled effect of internal and external fouling. To derive a microfiltration fouling model, future studies should focus on the following:

- Derive an internal fouling model by modifying Hermia's standard pore blocking or Fillipov's sieving mechanisms.[2-3]
- Modify the models discussed in Chapter 4 and 5 to incorporate the influence of pore size distribution on membrane fouling. For microfiltration, foulant size is similar to the membrane pore size, so pore size distribution can significantly affect local permeate flux and fouling progression.
- Combine the internal fouling model with CCM/cake filtration model. Validate the proposed model by constant flux crossflow filtration experiments using isoporous membranes/PVDF membranes and latex bead suspension.

7.4.3 Investigate the influences of membrane properties on the hindrance factor

Currently, the CCM model mainly focuses on the influence of operating condition (*e.g.*, foulant concentration, crossflow rate, and permeate flux) on pressure evolution. However, the influence of membrane/foulant properties on pressure evolution is not clear in CCM. Future studies of CCM should focus on the following:

- Investigate how membrane pure water permeance, pore size distribution, and hydrophilicity affect hindrance factor.
- Relate the hindrance factor to extended DLVO model.

7.4.4 Further investigation of flux stepping and threshold flux

The permeate flux of flux stepping experiments in this research always increases as a function of time. Dr. Sharma suggests that flux stepping experiments should include a "stepping-down" process, which could help decoupling reversible and irreversible fouling. The influence of decreasing permeate flux on pressure evolution and threshold flux should be evaluated in the future.

7.5 REFERENCES

1. Kasemset, S.; Wang, L.; He, Z.; Miller, D. J.; Kirschner, A.; Freeman, B. D.; Sharma, M. M., Influence of Polydopamine Deposition Conditions on Hydraulic Permeability, Sieving Coefficients, Pore Size and Pore Size Distribution for a Polysulfone Ultrafiltration Membrane. *Journal of Membrane Science* **2017,** *522*, 100-115.

2. Hermia, J., Constant Pressure Blocking Filtration Laws: Application to Power-Law Non-Newtonian Fluids. *Transactions of the Institution of Chemical Engineers* **1982,** *60*, 183-187.

3. Filippov, A.; Starov, V. M.; Llyod, D. R.; Chakravarti, S.; Glaser, S., Sieve Mechanism of Microfiltration. *Journal of Membrane Science* **1994,** *89* (3), 199-213.

APPENDICES

Appendix A: Supporting information – Complete Coverage Model

A.1 FITTING METHOD

The model (*i.e.*, Equation 5.16) is fit to experimental data in two stages. First, a three-parameter fit is used, allowing λ, K_{CCM} and K_c to vary. This method was not found to be practical because the three parameters are not bounded, and there is no control over how they vary. However, the fitted λ value is useful for estimating the time when the fouling mechanism transitions from the complete coverage model (CCM) to cake filtration (t^*). Mathematically, t^* is defined as the time when the exponential term of Equation 5.11 equals 0.01, and it can be calculated as follows:

$$t^* = -\frac{\ln(0.01)}{\lambda} \qquad \textbf{A.1}$$

The slope of the experimental ΔP vs. time plot is then calculated for each constant flux fouling experiment from t* until the end of the experiment. The relationship between this slope, K_{CCM} and K_c is given by Equation 5.17. A one parameter fit was then used (varying only λ), as set forth in the dissertation.

A.2 PARAMETER MEASUREMENTS

The one-parameter fit requires the values of f, k_a, and σ to calculate K_{CCM} (Equation 5.12). The methods for determining these parameters are described in the following section.

A.2.1 Permeate flow hindrance factor (f)

The value of f was estimated using fouling data at high concentration and low permeate flux. The membrane is fouled with a 300 ppm latex bead suspension to ensure that particles fully cover the membrane surface, and the permeate flux is kept low to prevent cake formation. Fig. A.1 presents an SEM image of a membrane fouled under these conditions. The membrane surface is mostly covered by particles, and some defects in the membrane surface are visible as well. The ΔP is steady over time except for the initial rise, similar to the CCM model prediction with negligible cake filtration. This pressure profile is fit to Equation 5.16 using the three-parameter fitting method described above, and t^* is calculated using Equation A.1. Cake formation is negligible and the membrane surface is mostly covered, indicating that K_{CCM} of Equation 5.12 should reach its theoretical maximum. Thus, the average ΔP from t^* to the end of the experiment, ΔP_{avg} can be calculated as follows:

$$P_{avg} = \frac{P_0}{1 - 1/f} \qquad \textbf{A.2}$$

The calculated value of f, based on the transmembrane pressure profile in Fig. A.1 and Equation A.2, is $f = 0.114 \pm 0.008$.

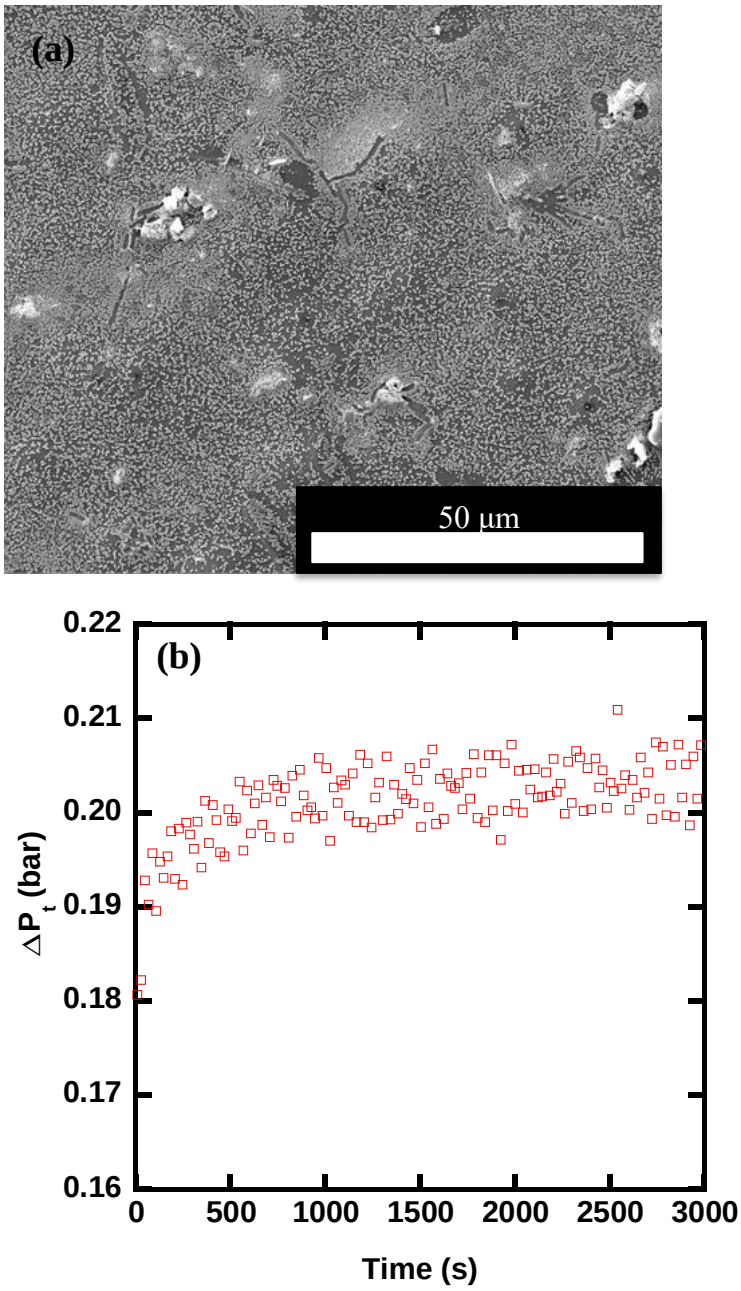

Fig. A.1: (a) SEM image and (b) ΔP profile of a fouled membrane at high concentration and low permeate flux. Fouling condition: 300 ppm latex beads concentration, 40 LMH permeate flux, and 0.8 L/min crossflow rate.

A.2.2 Adsorption and desorption rate constants

The adsorption and desorption rate constants were measured by adsorption/desorption tests. First, pure water permeance values of pristine PES membranes were measured. The membranes were then immersed in 200 ppm latex bead foulant solutions for a set amount of time. Then, their pure water permeance values were remeasured and compared to those of pristine membranes. After the second set of permeance measurements, the membranes with latex beads adsorbed onto their surfaces (*i.e.*, fouled membranes) were soaked in ultrapure water for 24 hr, and their permeances were measured for a third time to calculate the desorption rate constant. The pristine/fouled/desorbed membrane permeances are presented in Table A1.

Pure water permeance decreased following adsorption, and the fouled/pristine membrane permeance ratios decrease with increasing adsorption time. Thus, foulant particle adsorption onto membrane surface increases with soaking time. However, even after 24 hours of soaking in ultrapure water, the pure water permeance does not show a significant increase. Thus, the desorption rate is extremely slow compared to the adsorption rate. Thus, we assume k_d, the desorption constant, is approximately zero in subsequent data fitting.

The permeance ratio of fouled and pristine membranes can be used for adsorption constant calculations. The permeate flux and shear force terms of Equation 5.6 are zero in steady adsorption tests:

$$\frac{da_p}{dt} = k_a c(a_0 - a_p) - k_d a_p \qquad \textbf{A.3}$$

Integration of Equation A.3 yields:

$$a_p(t) = \frac{k_a c a_0}{k_a c + k_d}\left(1 - e^{-(k_a c + k_d)t}\right) \qquad \textbf{A.4}$$

As mentioned above, the desorption term is negligible, so Equation A.4 can be simplified:

$$a_p(t) = a_0\left(1 - e^{-k_a ct}\right) \qquad \textbf{A.5}$$

According to Equations 3.1 and 3.2, the permeance ratio equals the volumetric flow rate ratio between fouled and clean membrane, given that the membrane surface area and ΔP are the same for all pure water measurements. The volumetric flow rate of fouled and pristine membranes can be described by Darcy's Law:

$$Q' = \frac{\Delta P(a_0 - a_p)}{\mu R} + \frac{\Delta P a_p}{\mu f R} \qquad \textbf{A.6}$$

$$Q_0 = \frac{\Delta P a_0}{\mu R} \qquad \textbf{A.7}$$

where Q' and Q_0 are the volumetric flow rates of fouled and pristine membranes, respectively. Dividing Equation A.6 with A.7, then inserting Equation A.5 yields:

$$permeance\ ratio = \frac{Q'}{Q_0} = 1 - \left(1 - 1/f\right)\left(1 - e^{-k_a ct}\right) \qquad \textbf{A.8}$$

The fitting permeance ratio data in Table A1, along with Equation A.8, can give the adsorption constant, which is 4.6×10^{-7} $ppm^{-1}s^{-1}$.

Table A1: Permeances of pristine, fouled and desorbed PES membranes

Adsorption time (hr)	Pristine membrane permeance (LMH/bar)	Fouled membrane permeance (LMH/bar)	Desorbed membrane permeance (LMH/bar)	Fouled/clean membrane permeance ratio
1	383±6	364±3	362±8	0.950
2	349±5	325±5	326±4	0.935
4	359±4	333±6	333±5	0.925
6	324±21	293±24	290±20	0.902
8	332±8	295±9	293±7	0.889

A.2.3 Projected surface area per unit filtrate volume (σ)

σ is defined as the blocked area per unit filtrate volume, and can be calculated using the following equation from Hermia:[1]

$$\sigma = 1.5\frac{\gamma s}{\gamma_0 d\psi} \qquad \textbf{A.9}$$

where γ and γ_0 are the densities of the suspension and latex beads, respectively [kg/m^3]. d is the diameter of the latex beads [m] and ψ is the shape factor [-]. Except for ψ, the other parameters are known properties of the latex bead suspension. ψ is roughly estimated using the raw data from section 5.4.2.1, where the influence of concentration on K_{CCM} is discussed. Three-parameter fits to Equation 5.16 were conducted for the raw data in Fig.

5.7. Then, the resulting K_{CCM} values were fit to Equations 5.8 and 5.12 using ψ as the fitting parameter. However, a value for the resuspension rate (B) in Equation 5.8 is also needed for this fitting. The resuspension rates at 40, 50 and 60 LMH were measured using cleaning tests. A representative ΔP profile during a cleaning test is shown in Fig. A.2(a). Membranes were first fouled for 5 cm filtration length ("filtration length" is total filtrated volume divided by the total membrane area and in constant flux experiments, is directly proportional to filtration time), then the feed was switched to DI water. The crossflow shear force of the DI water feed can remove some foulants from the membrane surface, so ΔP decreases over time during water cleaning. As particle deposition and desorption are negligible, Equation 5.6 can be simplified as follows, assuming negligible cake filtration:

$$\frac{da_p}{dt} = -Ba_p \qquad \textbf{A.10}$$

Integration of Equation A.10 yields:

$$a_p = a_{p0}e^{-Bt} \qquad \textbf{A.11}$$

where a_{p0} is the projected surface area when water cleaning starts, and t is the water cleaning time. The TMP during water cleaning, ΔP_C, can be related to a_p using Darcy's Law:

$$\frac{\Delta P_C(a_0 - a_p)}{\mu R_0} + \frac{\Delta P_C a_p}{f\,\mu R_0} = \frac{\Delta P_0 a_0}{\mu R_0} \qquad \textbf{A.12}$$

The TMP when water cleaning starts, ΔP_{C0}, can also be related to a_{p0}:

$$\frac{\Delta P_{C0}(a_0 - a_{p0})}{\mu R_0} + \frac{\Delta P_{C0} a_{p0}}{f\,\mu R_0} = \frac{\Delta P_0 a_0}{\mu R_0} \qquad \textbf{A.13}$$

Combining Equations A.11-A.13 yields:

$$\Delta P_C = \frac{\Delta P_0}{1-\left[1-\Delta P_0 / \Delta P_f \left(e^{-Bt}\right)\right]} \qquad \textbf{A.14}$$

Equation A.14 is fit to cleaning test data by using B as the fitting parameter. The results are presented in Fig. A.2. The fitted B values decrease with increasing permeate flux because the drag force, which is proportional to permeate flux, increases while the shear force, which depends on crossflow rate, remains constant. The model curve at 60 LMH deviates slightly from the experimental data due to cake formation. As mentioned in section 5.2.1, 60 LMH is close enough to the TF that cake begins to grow on the membrane surface, which is not included in Equation A.14. As a result, the fit in Fig. A.2(b) is poorer for 60 LMH than for the lower fluxes.

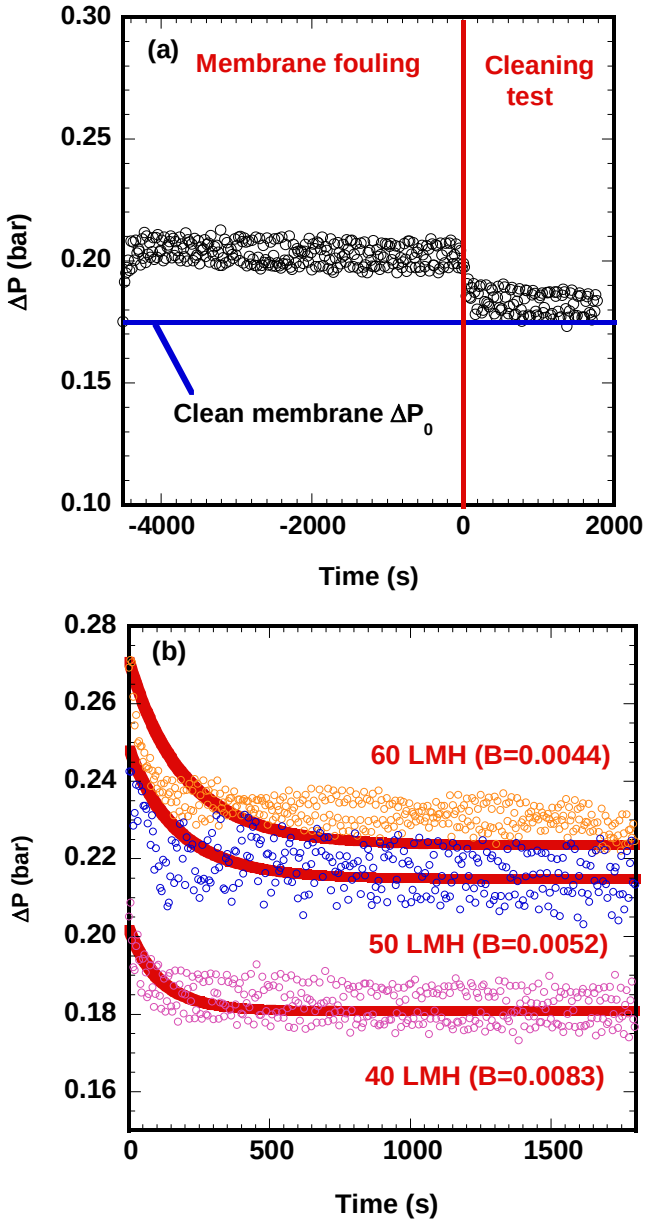

Fig. A.2: (a) A representative ΔP profile for a cleaning test to determine the foulant resuspension rate, B. The membrane was fouled first, and then the feed was switched to DI water at time 0. (b) ΔP profiles of cleaning tests (open circles) and model fits (solid curves). Fouling conditions: 200 ppm foulant concentration and 0.8 L/min crossflow rate.

The fitted B values in Fig. A.2(b) are used to calculate ψ, and the results are presented in Fig. A.3. The ψ values range from 0.018 to 0.168. If one were to hold ψ constant (i.e., independent of permeate flux) and calculate the best ψ value (i.e., the value which minimized the sum of squares of the deviations between the model and experimental data) for all the data in this study, the resulting volume of ψ was 0.12. This value of ψ gave the minimum sum of error squares for most of the fittings. Therefore, this value of ψ (0.12) was used for all one-parameter model fits presented in this study.

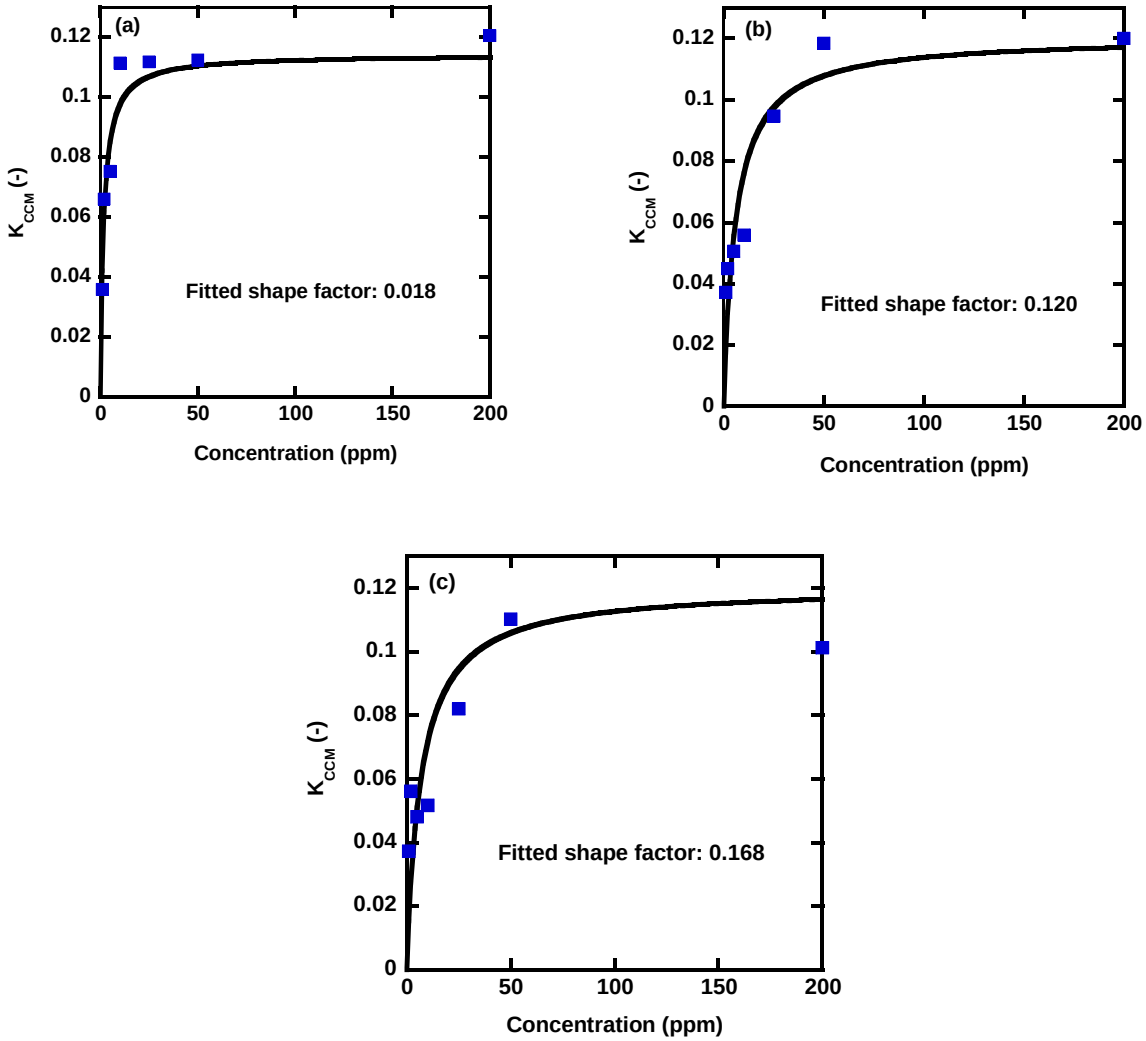

Fig. A.3: Fitted K_{CCM} values (blue points) using the three parameter fit vs. concentration at (a) 40 LMH (b) 50 LMH and (c) 60 LMH. The K_{CCM} values were fitted with Equation 5.12 using ψ as the fitting parameter. The fitting curves are shown as black solid curves for each permeate flux. The crossflow rate is 0.8 L/min.

In principle, the theoretical shape factor, ψ, should be close to 1 because the latex beads used in this study are spherical.[1] However, all three ψ values are much smaller than

1, ranging from 0.018 to 0.168. The small fitted ψ values are ascribed to the membrane pore size distribution and uneven particle deposition. Ultrafiltration membranes typically have a broad pore size distribution.[2] The Hagen-Poiseuille Equation, which is typically used to model water flow through such pore, is:[1]

$$\Delta P = \frac{8\mu L}{\pi r^4} Q \qquad \textbf{A.15}$$

where L is the effective membrane thickness [m], r is pore size radius [m], and Q is the volumetric flow rate through the pore [m^3/s]. Based on Equation A.15, local flow rate varies with pore size, given that ΔP across all pores is the same. Variations in flowrate through individual pores will lead to uneven particle deposition on the membrane surface. Drag forces around large pores are strong, so particles tend to deposit around such pores and hinder the permeate flow through them first. SEM images of membranes fouled for various times are shown in Fig. A.4. Particle deposition forms islands in the first 30 s of fouling (Fig. A.4(a)). These islands grow larger over time and merge with each other as fouling progresses (Fig. A.4(b) and (c)), and they eventually cover the entire surface if foulant concentration is high enough (Fig. A.4d). These images are consistent with uneven particle deposition, instead of uniform deposition as assumed by the CCM model. The hindrance of big pores also has a stronger influence on ΔP than does that of small pores. However, the CCM and IPB models do not consider the influence of pore size distribution on overall TMP, so the hindrance of a big pore is equivalent to the hindrance of several uniform-sized pores in the model. Since the permeate flux and concentration are constant throughout an experiment, the only way for models to capture the hindrance effect of big pores is by using a small ψ value. Based on the Hermia's model, a small shape factor represents a large projected surface area per particle.[1] A simulated particle with a small ψ

value (*i.e.*, large surface area) can hinder several uniform-size pores in the simulation, which can mimic the hindrance effect of a large pore. A comparison between two different shape factor is shown in Fig. A.5. The experimental data are the same as for Fig. 5.14(a). A shape factor equal to one is unable to fit the data and gives a much slower initial rise in ΔP than observed in the actual data. On the other hand, $\psi=0.12$ gives a better fit because the simulated particles are allowed to hinder several pores during the initial stage of fouling, which has a similar influence on ΔP as when large pores are hindered by latex beads. In conclusion, a low shape factor is required because the uniform pore size assumption in the CCM deviates from the wide pore size distribution of real membranes. Incorporation of pore size distribution into the CCM should be the focus of a future study.

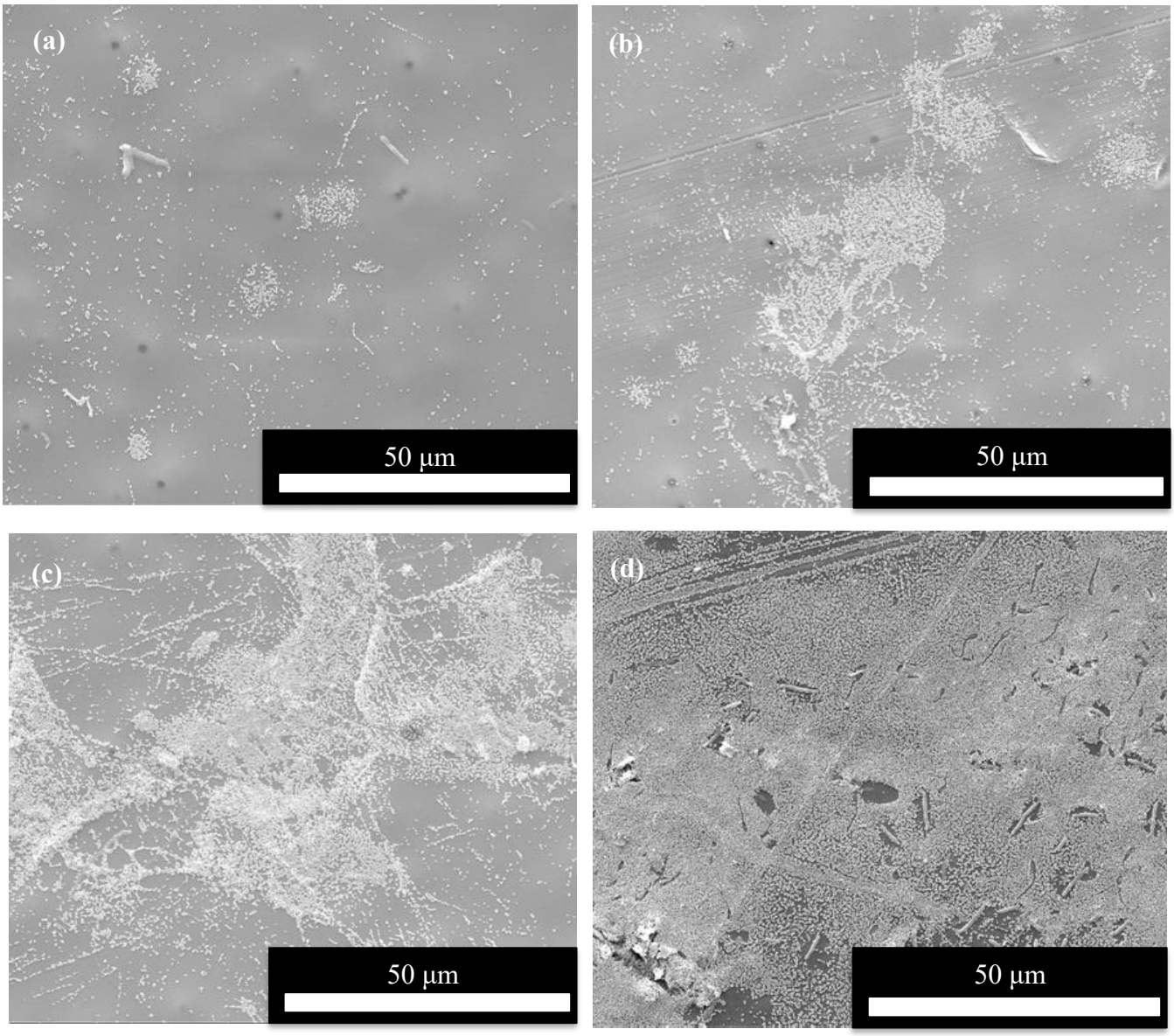

Fig. A.4: SEM images of membranes after (a) 30 s, (b) 60 s, (c) 180 s, and (d) 4500 s of fouling. Fouling condition: 200 ppm latex bead concentration, 40 LMH permeate flux and 0.8 L/min crossflow rate.

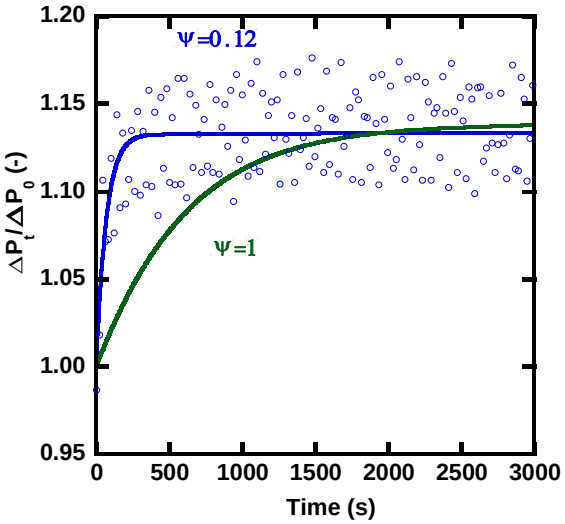

Fig. A.5: Fitting comparison between ψ=0.12 and ψ=1. The experimental data are the same as in Fig. 5.14. Fouling conditions: 25 ppm foulant concentration, 0.6 L/min crossflow rate and 40 LMH permeate flux.

A.3 REFERENCES

1. J. Hermia, Constant Pressure Blocking Filtration Laws: Application to Power-Law Non-Newtonian Fluids, (1982).

2. S. Kasemset, L. Wang, Z. He, D.J. Miller, A. Kirschner, B.D. Freeman, M.M. Sharma, Influence of Polydopamine Deposition Conditions on Hydraulic Permeability, Sieving Coefficients, Pore Size and Pore Size Distribution for a Polysulfone Ultrafiltration Membrane, Journal of Membrane Science, 522 (2017) 100-115.

Bibliography

Bacchin, P.; Aimar, P.; Field, R. W., Critical and Sustainable Fluxes: Theory, Experiments and Applications. *Journal of Membrane Science* **2006,** *281*, 42–69.

Bailey, R. S., Ground Water Contamination – Fracking Controversy Continues. *The Los Angles Post* 2011.

Baker, R. W., *Membrane Technology and Applications*. Third ed.; John Wiley & Sons Ltd.: West Sussex, UK, 2012.

Baker, R. W., *Membrane Technology and Applications. 2nd Ed.* Wiley: 2004.

Beier, S. P.; Jonsson, G., Critical Flux Determination by Flux-Stepping. *AIChE Journal* **2010,** *56* (7), 1739-1747.

Bevington, P. R.; Robinson, D. K., *Data Reduction and Error Analysis for the Physical Sciences*. 3rd ed.; The McGraw-Hill Companies, Inc.: New York, NY, 2003.

Bowen, W. R.; Calvo, J. I.; Hernández, A., Steps of Membrane Blocking in Flux Decline During Protein Microfiltration. *Journal of Membrane Science* **1995,** *101* (1), 153-165.

Cai, T.; Li, X.; Wan, C.; Chung, T.-S., Zwitterionic Polymers Grafted Poly(Ether Sulfone) Hollow Fiber Membranes and Their Antifouling Nehaviors for Osmotic Power Generation. *Journal of Membrane Science* **2016,** *497*, 142-152.

Chang, I.-S.; Clech, P. L.; Jefferson, B.; Judd, S., Membrane Fouling in Membrane Bioreactors for Wastewater Treatment. *Journal of Environmental Engineering* **2002,** *128* (11), 1018-1029.

Council, W. E., World Energy Resources-Unconventional Gas, a Global Phenomenon. **2016**.

Elimelech, M.; Phillip, W. A., The Future of Seawater Desalination: Energy, Technology, and the Environment. *Science* **2011,** *333* (6043), 712-717.

Field, R. W.; Pearce, G. K., Critical, Sustainable and Threshold Fluxes for Membrane Filtration with Water Industry Applications. *Advances in Colloid and Interface Science* **2011,** *164* (1), 38-44.

Field, R. W.; Wu, D.; Howell, J. A.; Gupta, B. B., Critical Flux Concept for Microfiltration Fouling. *Journal of Membrane Science* **1995,** *100* (3), 259-272.

Field, R. W.; Wu, J. J., Modelling of Permeability Loss in Membrane Filtration: Re-Examination of Fundamental Fouling Equations and Their Link to Critical Flux. *Desalination* **2011,** *283*, 68-74.

Filippov, A.; Starov, V. M.; Llyod, D. R.; Chakravarti, S.; Glaser, S., Sieve Mechanism of Microfiltration. *Journal of Membrane Science* **1994,** *89* (3), 199-213.

Finkel, M.; Hays, J.; Law, A., The Shale Gas Boom and the Need for Rational Policy. *Am J Public Health* **2013,** *103* (7), 1161-1163.

Fischer, E.; Schrader, H., Verbindungen Von Chinon Mit Aminosäureestern. *Berichte der Deutschen Chemischen Gesellschaft* **1910,** *43* (1), 525-529.

Fux, G.; Ramon, G. Z., Microscale Dynamics of Oil Droplets at a Membrane Surface: Deformation, Reversibility, and Implications for Fouling. *Environmental science & technology* **2017,** *51* (23), 13842-13849.

Geise, G. M.; Lee, H.-S.; Miller, D. J.; Freeman, B. D.; McGrath, J. E.; Paul, D. R., Water Purification by Membranes: The Role of Polymer Science. *Journal of Polymer Science Part B: Polymer Physics* **2010,** *48* (15), 1685-1718.

Guo, W.; Ngo, H.-H.; Li, J., A Mini-Review on Membrane Fouling. *Bioresource Technology* **2012,** *122*, 27-34.

Hamiche, A. M.; Stambouli, A. B.; Flazi, S., A Review of the Water-Energy Nexus. *Renewable and Sustainable Energy Reviews* **2016,** *65*, 319-331.

Hand, E., Injection Wells Blamed in Oklahoma Earthquakes. *Science* **2014,** *345* (6192), 13-14.

He, Z.; Miller, D. J.; Kasemset, S.; Wang, L.; Paul, D. R.; Freeman, B. D., Fouling Propensity of a Poly(Vinylidene Fluoride) Microfiltration Membrane to Several Model Oil/Water Emulsions. *Journal of Membrane Science* **2016,** *514*, 659-670.

Hermia, J., Constant Pressure Blocking Filtration Laws – Application to Power-Law Non-Newtonian Fluids. *Transactions of the American Institute of Chemical Engineers* **1982,** *60*, 183–187.

Ho, C. C.; Zydney, A. L., A Combined Pore Blockage and Cake Filtration Model for Protein Fouling During Microfiltration. *Journal of Colloid and Interface Science* **2000,** *232* (2), 389-399.

Ho, C. C.; Zydney, A. L., Transmembrane Pressure Profiles During Constant Flux Microfiltration of Bovine Serum Albumin. *Journal of Membrane Science* **2002,** *209* (2), 363-377.

Howe, K. J.; Clark, M. M., Fouling of Microfiltration and Ultrafiltration Membranes by Natural Waters. *Environmental science & technology* **2002,** *36* (16), 3571-3576.

J.R. Pressdee, S. V., H.L. Shorney-Darby, J.A. Clement, J.P. Van der Hoek, *Integration of Membrane Filtration into Water Treatment Systems*. American Water Works Association Research Foundation and U.S. Department of the Interior, Bureau of Reclamation: 2006.

Jiang, S.; Cao, Z., Ultralow-Fouling, Functionalizable, and Hydrolyzable Zwitterionic Materials and Their Derivatives for Biological Applications. *Advanced Materials* **2010,** *22* (9), 920-932.

Ju, H.; McCloskey, B. D.; Sagle, A. C.; Kusuma, V. A.; Freeman, B. D., Preparation and Characterization of Crosslinked Poly(Ethylene Glycol) Diacrylate Hydrogels as Fouling-Resistant Membrane Coating Materials. *Journal of Membrane Science* **2009,** *330* (1–2), 180-188.

Ju, H.; McCloskey, B. D.; Sagle, A. C.; Wu, Y.-H.; Kusuma, V. A.; Freeman, B. D., Crosslinked Poly(Ethylene Oxide) Fouling Resistant Coating Materials for Oil/Water Separation. *Journal of Membrane Science* **2008,** *307* (2), 260-267.

Kaleem, K.; Chertok, F.; Erhan, S., A Novel Coating Based on Poly(Etheramine-Quinone) Polymers. *Progress in Organic Coatings* **1987,** *15* (1), 63-71.

Kaleem, K.; Chertok, F.; Erhan, S., Quinone–Amine Polymers. II. 1,3-Bis(3-Aminophenoxy) Benzene-P-Benzoquinone Oligomers. *Journal of Polymer Science Part A: Polymer Chemistry* **1989,** *27* (3), 865-872.

Kasemset, S.; He, Z.; Miller, D. J.; Freeman, B. D.; Sharma, M. M., Effect of Polydopamine Deposition Conditions on Polysulfone Ultrafiltration Membrane Properties and Threshold Flux During Oil/Water Emulsion Filtration. *Polymer* **2016,** *97*, 247-257.

Kasemset, S.; Lee, A.; Miller, D. J.; Freeman, B. D.; Sharma, M. M., Effect of Polydopamine Deposition Conditions on Fouling Resistance, Physical Properties, and Permeation Properties of Reverse Osmosis Membranes in Oil/Water Separation. *Journal of Membrane Science* **2013,** *425–426*, 208-216.

Kasemset, S.; Wang, L.; He, Z.; Miller, D. J.; Kirschner, A.; Freeman, B. D.; Sharma, M. M., Influence of Polydopamine Deposition Conditions on Hydraulic Permeability, Sieving Coefficients, Pore Size and Pore Size Distribution for a Polysulfone Ultrafiltration Membrane. *Journal of Membrane Science* **2017,** *522*, 100-115.

Kirschner, A. Y.; Chang, C.-C.; Kasemset, S.; Emrick, T.; Freeman, B. D., Fouling-Resistant Ultrafiltration Membranes Prepared via Co-Deposition of Dopamine/Zwitterion Composite Coatings. *Journal of Membrane Science* **2017,** *541*, 300-311.

Kirschner, A. Y.; Cheng, Y. H.; Paul, D. R.; Field, R. W.; Freeman, B. D., Fouling Mechanisms in Constant Flux Crossflow Ultrafiltration. *Journal of Membrane Science* **2019,** *574*, 65-75.

Kochkodan, V.; Hilal, N., A Comprehensive Review on Surface Modified Polymer Membranes for Biofouling Mitigation. *Desalination* **2015,** *356*, 187-207.

Le Clech, P.; Jefferson, B.; Chang, I. S.; Judd, S. J., Critical Flux Determination by the Flux-Step Method in a Submerged Membrane Bioreactor. *Journal of Membrane Science* **2003,** *227* (1–2), 81-93.

Le-Clech, P.; Chen, V.; Fane, T. A. G., Fouling in Membrane Bioreactors Used in Wastewater Treatment. *Journal of Membrane Science* **2006,** *284* (1), 17-53.

Lee, H.; Amy, G.; Cho, J.; Yoon, Y.; Moon, S.-H.; Kim, I. S., Cleaning Strategies for Flux Recovery of an Ultrafiltration Membrane Fouled by Natural Organic Matter. *Water Research* **2001,** *35* (14), 3301-3308.

Lee, H.; Dellatore, S. M.; Miller, W. M.; Messersmith, P. B., Mussel-Inspired Surface Chemistry for Multifunctional Coatings. *Science* **2007,** *318* (5849), 426-430.

Lee, H.; Lee, Y.; Statz, A. R.; Rho, J.; Park, T. G.; Messersmith, P. B., Substrate-Independent Layer-by-Layer Assembly by Using Mussel-Adhesive-Inspired Polymers. *Advanced Materials* **2008,** *20* (9), 1619-1623.

Liu, Q.-F.; Kim, S.-H., Evaluation of Membrane Fouling Models Based on Bench-Scale Experiments: A Comparison between Constant Flowrate Blocking Laws and Artificial Neural Network (ANNs) Model. *Journal of Membrane Science* **2008,** *310* (1), 393-401.

Luo, J.; Morthensen, S. T.; Meyer, A. S.; Pinelo, M., Filtration Behavior of Casein Glycomacropeptide (Cgmp) in an Enzymatic Membrane Reactor: Fouling Control

by Membrane Selection and Threshold Flux Operation. *Journal of Membrane Science* **2014,** *469*, 127–139.

McCloskey, B. D.; Park, H. B.; Ju, H.; Rowe, B. W.; Miller, D. J.; Chun, B. J.; Kin, K.; Freeman, B. D., Influence of Polydopamine Deposition Conditions on Pure Water Flux and Foulant Adhesion Resistance of Reverse Osmosis, Ultrafiltration, and Microfiltration Membranes. *Polymer* **2010,** *51* (15), 3472-3485.

McCloskey, B. D.; Park, H. B.; Ju, H.; Rowe, B. W.; Miller, D. J.; Freeman, B. D., A Bioinspired Fouling-Resistant Surface Modification for Water Purification Membranes. *Journal of Membrane Science* **2012,** *413–414*, 82-90.

McKinnon, J. T. *Advanced Filtration of Pulp Mill Wastes*; Environmental Protection Agency: Washington, D.C., 1979.

Mehta, A.; Zydney, A. L., Permeability and Selectivity Analysis for Ultrafiltration Membranes. *Journal of Membrane Science* **2005,** *249* (1–2), 245-249.

Miller, D. J.; Dreyer, D. R.; Bielawski, C. W.; Paul, D. R.; Freeman, B. D., Surface Modification of Water Purification Membranes. *Angewandte Chemie International Edition* **2017,** *56* (17), 4662-4711.

Miller, D. J.; Huang, X.; Li, H.; Kasemset, S.; Lee, A.; Agnihotri, D.; Hayes, T.; Paul, D. R.; Freeman, B. D., Fouling-Resistant Membranes for the Treatment of Flowback Water from Hydraulic Shale Fracturing: A Pilot Study. *Journal of Membrane Science* **2013,** *437* (Supplement C), 265-275.

Miller, D. J.; Kasemset, S.; Paul, D. R.; Freeman, B. D., Comparison of Membrane Fouling at Constant Flux and Constant Transmembrane Pressure Conditions. *Journal of Membrane Science* **2014,** *454*, 505–515.

Miller, D. J.; Kasemset, S.; Wang, L.; Paul, D. R.; Freeman, B. D., Constant Flux Crossflow Filtration Evaluation of Surface-Modified Fouling-Resistant Membranes. *Journal of Membrane Science* **2014,** *452*, 171-183.

Miller, D. J.; Paul, D. R.; Freeman, B. D., A Crossflow Filtration System for Constant Permeate Flux Membrane Fouling Characterization. *Review of Scientific Instruments* **2013,** *84* (3), 035003.

Miller, D. J.; Paul, D. R.; Freeman, B. D., An Improved Method for Surface Modification of Porous Water Purification Membranes. *Polymer* **2014,** *55*, 1375–1383.

Mochizuki, S.; Zydney, A. L., Theoretical Analysis of Pore Size Distribution Effects on Membrane Transport. *Journal of Membrane Science* **1993,** *82* (3), 211-227.

Mueller, J.; Cen, Y.; Davis, R. H., Crossflow Microfiltration of Oily Water. *Journal of Membrane Science* **1997,** *129* (2), 221-235.

Nicot, J. P.; Scanlon, B. R., Water Use for Shale-Gas Production in Texas, U.S. *Environmental science & technology* **2012,** *46* (6), 3580-6.

Nicot, J.-P.; Scanlon, B. R.; Reedy, R. C.; Costley, R. A., Source and Fate of Hydraulic Fracturing Water in the Barnett Shale: A Historical Perspective. *Environmental science & technology* **2014,** *48* (4), 2464-2471.

Ognier, S.; Wisniewski, C.; Grasmick, A., Membrane Bioreactor Fouling in Sub-Critical Filtration Conditions: A Local Critical Flux Concept. *Journal of Membrane Science* **2004,** *229* (1), 171-177.

Opong, W. S.; Zydney, A. L., Diffusive and Convective Protein Transport through Asymmetric Membranes. *AIChE Journal* **1991,** *37* (10), 1497–1510.

Pearce, G. K., UF/MF Pre-Treatment to RO in Seawater and Wastewater Reuse Applications: A Comparison of Energy Costs. *Desalination* **2008,** *222* (1), 66-73.

Rassenfoss, S., From Flowback to Fracturing: Water Recycling Grows in the Marcellus Shale. *SPE-0711-0048-JPT* **2011,** *63* (07), 48-51.

Reddy, T. A.; Macaione, D.; Erhan, S., Quinone-Amine Polymers. XV. Syntheses and Characterization of High-Temperature Resistant Poly(Arylamino-Quinone)S. *Journal of Polymer Science Part A: Polymer Chemistry* **1994,** *32* (10), 1977-1982.

Roosjen, A.; Kaper, H. J.; van der Mei, H. C.; Norde, W.; Busscher, H. J., Inhibition of Adhesion of Yeasts and Bacteria by Poly(Ethylene Oxide)-Brushes on Glass in a Parallel Plate Flow Chamber. *Microbiology* **2003,** *149* (11), 3239-3246.

Ruth, B. F., Studies in Filtration III: Derivation of General Filtration Equations. *Industrial & Engineering Chemistry* **1935,** *27* (6), 708-723.

Sagle, A. C.; Ju, H.; Freeman, B. D.; Sharma, M. M., PEG-Based Hydrogel Membrane Coatings. *Polymer* **2009,** *50* (3), 756-766.

Sagle, A. C.; Van Wagner, E. M.; Ju, H.; McCloskey, B. D.; Freeman, B. D.; Sharma, M. M., PEG-Coated Reverse Osmosis Membranes: Desalination Properties and Fouling Resistance. *Journal of Membrane Science* **2009,** *340* (1–2), 92-108.

Scott, C. A.; Pierce, S. A.; Pasqualetti, M. J.; Jones, A. L.; Montz, B. E.; Hoover, J. H., Policy and Institutional Dimensions of the Water–Energy Nexus. *Energy Policy* **2011,** *39* (10), 6622-6630.

Siddiqi, A.; Anadon, L. D., The Water–Energy Nexus in Middle East and North Africa. *Energy Policy* **2011,** *39* (8), 4529-4540.

Singh, S.; Khulbe, K. C.; Matsuura, T.; Ramamurthy, P., Membrane Characterization by Solute Transport and Atomic Force Microscopy. *Journal of Membrane Science* **1998,** *142*, 111–127.

The AWWA Subcommittee On Periodical Publications of The Membrane Process, Microfiltration and Ultrafiltration Membranes for Drinking Water. *Journal (American Water Works Association)* **2008,** *100* (12), 84-97.

Tummons, E. N.; Tarabara, V. V.; Chew, Jia W.; Fane, A. G., Behavior of Oil Droplets at the Membrane Surface During Crossflow Microfiltration of Oil–Water Emulsions. *Journal of Membrane Science* **2016,** *500*, 211-224.

Ulbricht, M.; Matuschewski, H.; Oechel, A.; Hicke, H.-G., Photo-Induced Graft Polymerization Surface Modifications for the Preparation of Hydrophilic and Low-Proten-Adsorbing Ultrafiltration Membranes. *Journal of Membrane Science* **1996,** *115* (1), 31-47.

Van der Bruggen, B.; Vandecasteele, C.; Tim, V. G.; Doyen, W.; Leysen, R., A Review of Pressure-Driven Membrane Processes in Wastewater Treatment and Drinking Water Production. *Environmental Progress* **2003,** *22* (1), 46.

Wang, H.; Wu, J.; Cai, C.; Guo, J.; Fan, H.; Zhu, C.; Dong, H.; Zhao, N.; Xu, J., Mussel Inspired Modification of Polypropylene Separators by Catechol/Polyamine for Li-Ion Batteries. *ACS Applied Materials & Interfaces* **2014,** *6* (8), 5602-5608.

Wijmans, J. G.; Baker, R. W., The Solution-Diffusion Model: A Review. *Journal of Membrane Science* **1995,** *107* (1), 1-21.

Xie, W.; Geise, G. M.; Freeman, B. D.; Lee, H.-S.; Byun, G.; McGrath, J. E., Polyamide Interfacial Composite Membranes Prepared from M-Phenylene Diamine, Trimesoyl Chloride and a New Disulfonated Diamine. *Journal of Membrane Science* **2012,** *403-404*, 152-161.

Xu, Y. C.; Wang, Z. X.; Cheng, X. Q.; Xiao, Y. C.; Shao, L., Positively Charged Nanofiltration Membranes via Economically Mussel-Substance-Simulated Co-Deposition for Textile Wastewater Treatment. *Chemical Engineering Journal* **2016,** *303*, 555-564.

Yang, X.; Sun, P.; Zhang, H.; Xia, Z.; Waldman, R. Z.; Mane, A. U.; Elam, J. W.; Shao, L.; Darling, S. B., Polyphenol-Sensitized Atomic Layer Deposition for Membrane

Interface Hydrophilization. *Advanced Functional Materials* **2020,** *30* (15), 1910062.

Zeman, L.; Wales, M., Polymer Solute Rejection by Ultrafiltration Membranes. In *Synthetic Membranes: Volume II*, AMERICAN CHEMICAL SOCIETY: 1981; Vol. 154, pp 411-434.

Zeman, L. J.; Zydney, A. L., *Microfiltration and Ultrafiltration: Principles and Applications*. Marcel Dekker, Inc.: New York, NY, 1996.

Zhang, W.; Wahlgren, M.; Sivik, B., Membrane Characterization by the Contact Angle Technique: II. Characterization of UF-Membranes and Comparison between the Captive Bubble and Sessile Drop as Methods to Obtain Water Contact Angles. *Desalination* **1989,** *72* (3), 263-273.

Zhao, Y.-H.; Wee, K.-H.; Bai, R., Highly Hydrophilic and Low-Protein-Fouling Polypropylene Membrane Prepared by Surface Modification with Sulfobetaine-Based Zwitterionic Polymer through a Combined Surface Polymerization Method. *Journal of Membrane Science* **2010,** *362* (1–2), 326-333.

Zydney, A. L.; Aimar, P.; Meireles, M.; Pimbley, J. M.; Belfort, G., Use of the Log-Normal Probability Density Function to Analyze Membrane Pore Size Distributions: Functional Forms and Discrepancies. *Journal of Membrane Science* **1994,** *91* (3), 293-298.

Standard Test Method for Molecular Weight Cutoff Evaluation of Flat Sheet Ultrafiltration Membranes. ASTM International: West Conshohocken, PA, 2001.

Oklahoma Orders Wastewater Disposal Wells Shut Down after Earthquake. https://www.theguardian.com/us-news/2016/sep/04/oklahoma-wastewater-wells-earthquake#:~:text=Oklahoma%20orders%20wastewater%20disposal%20wells%20shut%20down%20after%20earthquake,-This%20article%20is&text=Five%20months%20ago%2C%20US%20officials,suffer%20tremors%20as%20northern%20California.

Reverse Osmosis Vs. Nanofiltration and Other Filtration Technologies. https://aquaclearllc.com/technical-info/reverse-osmosis-vs-nanofiltration-and-other-filtration-technologies/.

AMTA. Industrial Applications for Membranes 2014.